New multi-speed BGK thermal model in finite difference lattice Boltzmann method

Watari, Minoru

(Degree)
博士（工学）

(Date of Degree)
2003-03-31

(Date of Publication)
2017-04-28

(Resource Type)
doctoral thesis

(Report Number)
甲2799

(URL)
https://hdl.handle.net/20.500.14094/D1002799

Doctoral Dissertation

New multi-speed BGK thermal model in finite difference lattice Boltzmann method

March 2003

Graduate School of Science and Technology
Kobe University

WATARI Minoru

博士論文

New multi-speed BGK thermal model in finite difference lattice Boltzmann method

（差分格子ボルツマン法における
新しい多速ＢＧＫ型熱流体モデル）

2003年3月

神戸大学大学院自然科学研究科

渡利　實

Contents page

1. Introduction

Lattice gas automata (LGA), lattice Boltzmann method (LBM), and finite difference lattice Boltzmann method (FDLBM), which have historically evolved in this order, are currently used in simulating wide variety of fluid flows.[1] These methods have common features; microscopic models and mesoscopic kinetic equations are used to represent macroscopic continuum flow. The basic premise for these ideas is that the macroscopic dynamics of fluid is the result of the collective behavior of many microscopic particles, and that although microscopic details, like an interaction law between particles, affect parameters such as viscosity, the form of macroscopic dynamics is less sensitive to microscopic details.[2]

The LGA [3] is constructed as a simplified, fictitious molecular dynamic in which space, time, and particle velocities are discretized. To describe the state of particle's condition at each node x and each time t, a set of Boolean variables $n_i(x,t)$ is assumed, where the suffix i is the direction of the particle velocity. If the particle of ith direction is present, the variable $n_i(x,t)$ is set unity, whereas if absent, the $n_i(x,t)$ is set zero. The evolution of the variable $n_i(x,t)$ is governed by following equation.

$$n_i(x+c_i,t+1) = n_i(x,t) + \Omega_i[n(x,t)] \tag{1.1}$$

The particle velocity c_i is selected as to link adjacent nodes. Collision operator Ω_i is designed to conserve mass and momentum. Because of the variable $n_i(x,t)$'s Boolean nature, it is necessary to take ensemble averages to obtain macroscopic quantities.

The main feature of the LBM [4] is to replace the Boolean variable $n_i(x,t)$ by distribution function $f_i(x,t)$ ($\equiv < n_i > : < >$ denotes an ensemble average). Same as the LGA, particle velocity c_i is selected as to link adjacent nodes. Therefore, the evolution equation for the distribution function is similar to that of the LGA.

$$f_i(x+c_i,t+1) = f_i(x,t) + \Omega_i[f(x,t)] \tag{1.2}$$

However, as the distribution functions themselves are variables of the problem, the LBM is free from statistical noise. Macroscopic quantities, the density ρ and momentum density ρu, are defined by taking velocity moment summations.

$$\rho = \sum_i f_i \tag{1.3}$$

$$\rho u = \sum_i f_i c_i \tag{1.4}$$

Collision operator Ω_i is required to satisfy conservations of mass and momentum.

$$\sum_i \Omega_i = 0 \tag{1.5}$$

$$\sum_i \Omega_i c_i = 0 \tag{1.6}$$

Single relaxation time scheme proposed by Bhatnagar, Gross, and Krook (BGK scheme) is assumed in my study. Although the BGK scheme fixes the Prandtl number constant (=unity), it makes the collision operator quite simple and still has capability of wide applications.

$$\Omega_i \equiv -\frac{1}{\phi}(f_i - f_i^{(0)}) \tag{1.7}$$

where $f_i^{(0)}$ is the local equilibrium distribution function.

The FDLBM [5] was proposed as an extended version of LBM in order to secure numerical stability and to apply non-uniform grids. In place of the evolution equation of the LBM (1.2), following differential equation is used in the FDLBM.

$$\frac{\partial f_i}{\partial t} + c_{i\alpha}\frac{\partial f_i}{\partial r_\alpha} = \Omega_i(f) \tag{1.8}$$

In the LBM, particle velocity c_i, time increment Δt, and the lattice configuration must have a close relationship; the particle velocity has to link the lattice nodes in unit time. However, in the FDLBM, this requirement is no more necessary. Therefore, time increment Δt can be adjusted to satisfy CFL (Courant Friedrichs Lewy) requirement for numerical stability, and non-uniform grids, like polar grid or variable pitch grid, are available in the FDLBM.

My doctoral study is on models of LBM and FDLBM, especially focusing on FDLBM.

Chapter 2 [6] discusses the possibility to construct a LBM BGK thermal model. There are two ways to handle thermal fluid. One is the so-called "multi-component thermal model," where heat is handled as different component from fluid. This model characterizes the flow as Boussinesq fluid. Another is the so-called "multi-speed thermal model," where particle velocities that have different speeds are used. LBM BGK thermal models have been proposed by several authors. While these models are intended to correctly represent heat characteristics and compressibility, none of these existing models provides satisfactory accuracy. This chapter discusses the possibility of a correct model and how to construct it. To recover correct fluid equations, up-to fourth orders of local flow velocity should be retained in the local equilibrium distribution function and the particle velocities should have up-to seventh rank tensor isotropy. It is concluded that it is possible to construct a thermally correct two-dimensional LBM BGK multi-speed model. However, a correct three-dimensional LBM BGK multi-speed thermal model is theoretically impossible. A correct two-dimensional LBM multi-speed thermal model that has global weighting coefficients in the local equilibrium distribution function was proposed. Being applied to a Couette flow, this model showed exact agreement with the analytical solution.

Chapter 3 [7,8] proposes a new two-dimensional multi-speed thermal model for the FDLBM. In the FDLBM, particle velocities can be selected independently from the lattice configuration. Therefore, particle velocities of octagonal directions, which have up-to seventh rank isotropic tensors, are adopted. Furthermore, as the local equilibrium distribution function is determined such that it retains as much Maxwellian characteristic as possible, the proposed model has excellent numerical stability in addition to strict accuracy. The model was verified, being applied to three flow simulations. All results showed good agreement with the analytical solutions.

Chapter 4 [9] proposes a new three-dimensional multi-speed thermal model for the FDLBM. It has been shown in Chapter 2 that a three-dimensional LBM BGK multi-speed thermal model is theoretically impossible. Contrary to the LBM, as the FDLBM can select particle velocities independently from the lattice configuration, in the proposed model, a group of thirty-two particle velocities is selected as a basic group of moving particles, which are derived from vectors that point to the vertexes of dodecahedron and icosahedron from the center. As the group of thirty-two particle velocities has a quasi-isotropic sixth rank tensor, the model made up of a rest particle and four speeds of the basic groups showed good agreement with the analytical solutions when applied to two flow simulations.

Chapter 5 [10] discusses methods of boundary conditions. In the past, a lot of studies have been done to make clear boundary conditions for the LBM. Most of them are about boundary conditions for non-thermal models that have a limited number of particle velocities. Few studies are found that describe a clear receipt of boundary conditions for the FDLBM, especially for thermal models that have a large number of particle velocities. In this chapter, two methods of boundary conditions for thermal FDLBM are presented. Their performances were compared, being applied to benchmark tests. First method, called "control node method," can handle wide variety of boundary conditions and showed excellent performance on the tests. Control node method should be applied if accurate simulation is intended. Second method, called "extrapolation method," is simple and easy to make computing software. Although the performance of extrapolation method is not so high as the first method, it is a viable method if it is not required strict accuracy.

Chapter 6 [11] presents an example of applications simulated by proposed model and method of boundary conditions. In the past, numerical simulations have been extensively performed on natural convection in a square cavity with differently heated walls (thermal cavity flow). Most of these studies are for Boussinesq fluid. Although some studies treat the flows as compressible fluid, they do not clearly state how much compressibility affects the flows and

how far Boussinesq approximation is considered valid. Using the two-dimensional model in Chapter 3 and the control node method in Chapter 5, thermal cavity flow for compressible fluid was studied in a systematic manner and whole features were thoroughly revealed.

References

[1] M. Tsutahara, N. Takada, and T. Kataoka, "Lattice Gas and Lattice Boltzmann Methods", Corona (1999) (in Japanese).

[2] S. Chen and G. Doolen, "Lattice Boltzmann method for fluid flows", Annu. Rev. Fluid Mech. 30: 329-64 (1998).

[3] S. Wolfram, "Cellular automaton fluids 1: Basic Theory", J. Stat. Phys. 45: 471-526 (1986).

[4] GR. McNamara and G. Zanetti, "Use of the Boltzmann equation to simulate lattice gas automata", Phys. Rev. Lett. 61: 2332-35 (1988).

[5] N. Cao, S. Chen, S. Jin and D. Martinez, "Physical symmetry and lattice symmetry in the lattice Boltzmann method", Phys. Rev. E 55,1: R21-24 (1997).

[6] M. Watari and M. Tsutahara, "Is it possible to construct a multi-speed thermal model of the lattice Boltzmann method?", J. Stat. Phys. (submitted).

[7] M. Watari and M. Tsutahara, "Finite Difference Lattice Boltzmann Method Having a High Spatial Isotropy", Memory of Graduate School of Science and Technology Kobe University No.21-A, (2003).

[8] M. Watari and M. Tsutahara, "Two-Dimensional Thermal Model of Finite Difference Lattice Boltzmann Method with High Spatial Isotropy", Phys. Rev. E (submitted).

[9] M. Watari and M. Tsutahara, "Three-Dimensional Thermal Model of Finite Difference Lattice Boltzmann Method with High Spatial Isotropy", J. Stat. Phys. (submitted).

[10] M. Watari and M. Tsutahara, "Boundary Conditions for Finite Difference Lattice Boltzmann Method", JSME B (accepted, in Japanese).

[11] M. Watari and M. Tsutahara, "Thermal Cavity Flow of Compressible Fluids. Numerical Simulation by a Newly proposed Model of Finite Difference Lattice Boltzmann Method", The Fifth JSME-KSME Fluids Engineering Conference. Nov.17-21, CD-ROM No.02-207: 1699-1704 (2002).

2. Possibility to construct a multi-speed thermal model of the lattice Boltzmann method

2.1. Introduction

Multi-speed thermal models of the lattice Boltzmann method (LBM) that have a single relaxation (BGK) scheme have been proposed by several authors.[1-3] While the multi-speed thermal model is intended to correctly represent heat characteristics and compressibility, existing models do not give satisfactory accuracy when applied to the Couette flow simulation. These models were carefully investigated to discover whether a correct model is possible and how to construct it.

2.2. The conditions leading to correct fluid equations

Below are the conditions for the local equilibrium distribution function $f_{ki}^{(0)}$ for the particle velocity c_{ki} to lead to correct fluid equations. The symbol ρ is the density, u_α the velocity, and e the internal energy. The subscript symbol k indicates a group of the particle velocities whose speed c_k, and i indicates the particle velocity's direction. The subscript symbols α, β, and γ indicate the x, y, or z component. D is a space dimension.

$$\sum_{ki} f_{ki}^{(0)} = \rho \tag{2.1}$$

$$\sum_{ki} f_{ki}^{(0)} c_{ki\alpha} = \rho u_\alpha \tag{2.2}$$

$$\sum_{ki} f_{ki}^{(0)} c_{ki\alpha} c_{ki\beta} = \rho\left(\frac{2}{D} e\delta_{\alpha\beta} + u_\alpha u_\beta\right) \tag{2.3}$$

$$\sum_{ki} f_{ki}^{(0)} c_{ki\alpha} c_{ki\beta} c_{ki\gamma} = \rho\left[\frac{2}{D} e(u_\alpha \delta_{\beta\gamma} + u_\beta \delta_{\gamma\alpha} + u_\gamma \delta_{\alpha\beta}) + u_\alpha u_\beta u_\gamma\right] \tag{2.4}$$

$$\sum_{ki} f_{ki}^{(0)} \frac{c_k^2}{2} = \rho\left(e + \frac{u^2}{2}\right) \tag{2.5}$$

$$\sum_{ki} f_{ki}^{(0)} \frac{c_k^2}{2} c_{ki\alpha} = \rho u_\alpha \left(\frac{D+2}{D} e + \frac{u^2}{2}\right) \tag{2.6}$$

$$\sum_{ki} f_{ki}^{(0)} \frac{c_k^2}{2} c_{ki\alpha} c_{ki\beta} = \rho\left[\frac{2}{D} e\left(\frac{D+2}{D} e + \frac{u^2}{2}\right)\delta_{\alpha\beta} + u_\alpha u_\beta \left(\frac{D+4}{D} e + \frac{u^2}{2}\right)\right] \tag{2.7}$$

As energy diffusion equation (2.7) contains up-to fourth order of flow velocity u, local equilibrium distribution function $f_{ki}^{(0)}$ should retain up-to fourth order terms of flow velocity. Consequently, the local equilibrium distribution function is to contain the fourth rank tensor.

Considering that momentum diffusion equation (2.4) contains the third rank tensor, up-to seventh rank tensor is used. As a result, the tensors up-to seventh rank should be isotropic to recover correct fluid equations.

In the LBM, the particle velocities are restricted to those that exactly link the lattice nodes in unit time. Generally, cubic lattice is used in three dimensions, and the square or hexagonal lattice is used in two dimensions. However, the hexagonal lattice ensures only up-to fourth rank isotropy, which is insufficient to derive correct fluid equations. The model that uses a hexagonal lattice is not discussed further.

The basic particle velocities used in the square lattice and in the cubic lattice are shown in Figure 2.1 and Figure 2.2, respectively. The odd rank tensors for these particle velocities vanish. The even rank tensors generally have the following form: [4]

$$\sum_{i=1}^{b_k} 1 = b_k \tag{2.8}$$

$$\sum_i c_{ki\alpha} c_{ki\beta} = \chi_k \delta_{\alpha\beta} \tag{2.9}$$

$$\sum_i c_{ki\alpha} c_{ki\beta} c_{ki\gamma} c_{ki\chi} = \varphi_k \Delta^{(4)}_{\alpha\beta\gamma\chi} + \psi_k \delta_{\alpha\beta\gamma\chi} \tag{2.10}$$

$$\sum_i c_{ki\alpha} c_{ki\beta} c_{ki\gamma} c_{ki\chi} c_{ki\lambda} c_{ki\tau} = \Theta_k \Delta^{(6)}_{\alpha\beta\gamma\chi\lambda\tau} + \Omega_k \Delta^{(4,2)}_{\alpha\beta\gamma\chi\lambda\tau} + \Lambda_k \delta_{\alpha\beta\gamma\chi\lambda\tau} \tag{2.11}$$

$$\sum_i \frac{c_k^2}{2} = \frac{D}{2} \chi_k \tag{2.12}$$

$$\sum_i \frac{c_k^2}{2} c_{ki\alpha} c_{ki\beta} = \Gamma_k \delta_{\alpha\beta} \tag{2.13}$$

$$\sum_i \frac{c_k^2}{2} c_{ki\alpha} c_{ki\beta} c_{ki\gamma} c_{ki\chi} = \Pi_k \Delta^{(4)}_{\alpha\beta\gamma\chi} + \Xi_k \delta_{\alpha\beta\gamma\chi} \tag{2.14}$$

$$\sum_i \frac{c_k^2}{2} c_{ki\alpha} c_{ki\beta} c_{ki\gamma} c_{ki\chi} c_{ki\lambda} c_{ki\tau} = \mathrm{B}_k \Delta^{(6)}_{\alpha\beta\gamma\chi\lambda\tau} + \mathrm{N}_k \Delta^{(4,2)}_{\alpha\beta\gamma\chi\lambda\tau} + \mathrm{Z}_k \delta_{\alpha\beta\gamma\chi\lambda\tau} \tag{2.15}$$

The tensors that appear in the above equations are defined as follows:

$\delta_{\alpha\beta}$=1 (if α=β), =0 (otherwise)
$\delta_{\alpha\beta\gamma\chi}$=1 (if α=β=γ=χ), =0 (otherwise)
$\delta_{\alpha\beta\gamma\chi\lambda\tau}$=1 (if α=β=γ=χ=λ=τ), =0 (otherwise) (2.16 abcdef)

$$\Delta^{(4)}_{\alpha\beta\gamma\chi}=\delta_{\alpha\beta}\delta_{\gamma\chi}+\delta_{\alpha\gamma}\delta_{\beta\chi}+\delta_{\alpha\chi}\delta_{\beta\gamma}$$

$$\Delta^{(6)}_{\alpha\beta\gamma\chi\lambda\tau}=\delta_{\alpha\beta}\Delta^{(4)}_{\gamma\chi\lambda\tau}+\delta_{\alpha\gamma}\Delta^{(4)}_{\beta\chi\lambda\tau}+\delta_{\alpha\chi}\Delta^{(4)}_{\beta\gamma\lambda\tau}+\delta_{\alpha\lambda}\Delta^{(4)}_{\beta\gamma\chi\tau}+\delta_{\alpha\tau}\Delta^{(4)}_{\beta\gamma\chi\lambda}$$

$$\Delta^{(4,2)}_{\alpha\beta\gamma\chi\lambda\tau}=\delta_{\alpha\beta}\delta_{\gamma\chi\lambda\tau}+\delta_{\alpha\gamma}\delta_{\beta\chi\lambda\tau}+\delta_{\alpha\chi}\delta_{\beta\gamma\lambda\tau}+\delta_{\alpha\lambda}\delta_{\beta\gamma\chi\tau}+\delta_{\alpha\tau}\delta_{\beta\gamma\chi\lambda}+\delta_{\beta\gamma}\delta_{\alpha\chi\lambda\tau}+\delta_{\beta\chi}\delta_{\alpha\gamma\lambda\tau}+\cdots$$

The tensors $\Delta^{(6)}_{\alpha\beta\gamma\chi\lambda\tau}$, $\Delta^{(4)}_{\alpha\beta\gamma\chi}$, $\delta_{\alpha\beta}$ are isotropic, whereas $\Delta^{(4,2)}_{\alpha\beta\gamma\chi\lambda\tau}$, $\delta_{\alpha\beta\gamma\chi\lambda\tau}$, $\delta_{\alpha\beta\gamma\chi}$ are anisotropic. The specific values of $b_k, \chi_k, \varphi_k \cdots, Z_k$ for the basic particle velocities in Figure 2.1 and Figure 2.2 are listed in Table 2.1 and Table 2.2, respectively. They are grouped into five groups depending on the influence of particle speed c_k. If particle velocities that have double or triple the speed of the basic particles are adopted, the values of $b_k, \chi_k, \varphi_k \cdots, Z_k$ increase to 2^n times or 3^n times of the basic values, depending on group c_k^n.

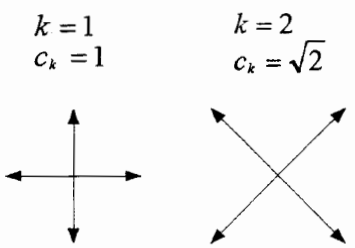

Figure 2.1. Basic particle velocities used in the square lattice.

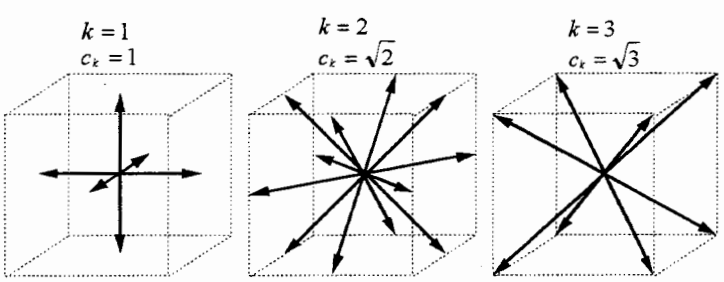

Figure 2.2. Basic particle velocities used in the cubic lattice. They consist of vectors in six, twelve, and eight directions.

Table 2.1. Specific values of $b_k, \chi_k, \varphi_k \cdots, \mathrm{B}_k$ for the basic particle velocities in the square lattice of Figure 2.1. They are grouped into five groups depending on the influence of particle speed c_k. For example, if particle velocities that have triple the speed of k=1 particles are adopted, the value of ψ_k becomes 2×3^4.

	k	1	2
	c_k	1	$\sqrt{2}$
c_k^0	b_k	4	4
c_k^2	χ_k	2	4
c_k^4	ψ_k	2	−8
	φ_k	0	4
	Γ_k	1	4
c_k^6	Λ_k	2	−16
	Ω_k	0	0
	Θ_k	0	$4/3$
	Ξ_k	1	−8
	Π_k	0	4
c_k^8	Z_k	1	−16
	N_k	0	0
	B_k	0	$4/3$

Table 2.2. Specific values of $b_k, \chi_k, \varphi_k \cdots, \mathrm{B}_k$ for the basic particle velocities in the cubic lattice of Figure 2.2.

	k	1	2	3
	c_k	1	$\sqrt{2}$	$\sqrt{3}$
c_k^0	b_k	6	12	8
c_k^2	χ_k	2	8	8
c_k^4	ψ_k	2	−4	−16
	φ_k	0	4	8
	Γ_k	1	8	12
c_k^6	Λ_k	2	−52	128
	Ω_k	0	4	−16
	Θ_k	0	8	0
	Ξ_k	1	−4	−24
	Π_k	0	4	12
c_k^8	Z_k	1	−52	192
	N_k	0	4	−24
	B_k	0	8	0

2.3. Model derivation

There seem to be two ways to define the local equilibrium distribution function. One is to distribute weighting coefficients to each power of u^2 and $c_{ki\alpha}u_\alpha$. The other is to distribute weighting coefficients to the whole expansion equation. Both types are discussed in this section.

2.3.1. Deriving a model that has global coefficients

This type of local equilibrium distribution function was adopted by Takada et al.[3], although their model retains up-to third order of local flow velocity. The local equilibrium distribution function that retains up-to fourth order is defined as follows. This form is derived by expanding Maxwellian distribution regarding local flow velocity u. Weighting coefficients F_k are placed before the polynomial.

$$f_{ki}^{(0)} = \rho F_k[(1-\frac{D}{4e}u^2+\frac{D^2}{32e^2}u^4)+\frac{D}{2e}(1-\frac{D}{4e}u^2)c_{ki\xi}u_\xi+\frac{D^2}{8e^2}(1-\frac{D}{4e}u^2)c_{ki\xi}c_{ki\eta}u_\xi u_\eta$$
$$+\frac{D^3}{48e^3}c_{ki\xi}c_{ki\eta}c_{ki\zeta}u_\xi u_\eta u_\zeta+\frac{D^4}{384e^4}c_{ki\xi}c_{ki\eta}c_{ki\zeta}c_{ki\chi}u_\xi u_\eta u_\zeta u_\chi] \tag{2.17}$$

This local equilibrium distribution function is applied to conditions (2.1) through (2.7). When the property in which the odd tensors vanish is applied, the following equations to determine weighting coefficients F_k are obtained:

$$\sum_{ki}F_k = 1 \tag{2.18}$$

$$\sum_{ki}F_k c_{ki\alpha}c_{ki\beta} = \frac{2}{D}e\delta_{\alpha\beta} \tag{2.19}$$

$$\sum_{ki}F_k c_{ki\alpha}c_{ki\beta}c_{ki\gamma}c_{ki\chi} = \frac{4}{D^2}e^2\Delta^{(4)}_{\alpha\beta\gamma\chi} \tag{2.20}$$

$$\sum_{ki}F_k c_{ki\alpha}c_{ki\beta}c_{ki\gamma}c_{ki\chi}c_{ki\lambda}c_{ki\tau} = \frac{8}{D^3}e^3\Delta^{(6)}_{\alpha\beta\gamma\chi\lambda\tau} \tag{2.21}$$

$$\sum_{ki}F_k\frac{c_k^2}{2} = e \tag{2.22}$$

$$\sum_{ki}F_k\frac{c_k^2}{2}c_{ki\alpha}c_{ki\beta} = \frac{2(D+2)}{D^2}e^2\delta_{\alpha\beta} \tag{2.23}$$

$$\sum_{ki}F_k\frac{c_k^2}{2}c_{ki\alpha}c_{ki\beta}c_{ki\gamma}c_{ki\chi} = \frac{4(D+4)}{D^3}e^3\Delta^{(4)}_{\alpha\beta\gamma\chi} \tag{2.24}$$

$$\sum_{ki} F_k \frac{c_k^2}{2} c_{ki\alpha} c_{ki\beta} c_{ki\gamma} c_{ki\chi} c_{ki\lambda} c_{ki\tau} = \frac{8(D+6)}{D^4} e^4 \Delta^{(6)}_{\alpha\beta\gamma\chi\lambda\tau} \tag{2.25}$$

Considering tensor expressions (2.8) through (2.15), constraints (2.18) through (2.25) can be rewritten as the following:

From (2.18),

$$\sum_k b_k F_k = 1 \tag{2.26}$$

From (2.19) and (2.22),

$$\sum_k \chi_k F_k = \frac{2}{D} e \tag{2.27}$$

From (2.20),

$$\sum_k \varphi_k F_k = \frac{4}{D^2} e^2 \tag{2.28}$$

$$\sum_k \psi_k F_k = 0 \tag{2.29}$$

From (2.21),

$$\sum_k \Theta_k F_k = \frac{8}{D^3} e^3 \tag{2.30}$$

$$\sum_k \Omega_k F_k = 0 \tag{2.31}$$

$$\sum_k \Lambda_k F_k = 0 \tag{2.32}$$

From (2.23),

$$\sum_k \Gamma_k F_k = \frac{2(D+2)}{D^2} e^2 \tag{2.33}$$

From (2.24),

$$\sum_k \Pi_k F_k = \frac{4(D+4)}{D^3} e^3 \tag{2.34}$$

$$\sum_k \Xi_k F_k = 0 \tag{2.35}$$

From (2.25),

$$\sum_k \mathrm{B}_k F_k = \frac{8(D+6)}{D^4} e^4 \tag{2.36}$$

$$\sum_k \mathrm{N}_k F_k = 0 \tag{2.37}$$

$$\sum_k Z_k F_k = 0 \tag{2.38}$$

First, let us discuss the model in three dimensions. The constraints are summarized in Table 2.3. In the table, the constraints are arranged into five groups according to manner of dependence on c_k^n. Let us consider the constraint equations of group c_k^6:

$$\begin{bmatrix} 2 & -52 & 128 \\ 0 & 4 & -16 \\ 0 & 8 & 0 \\ 1 & -4 & -24 \\ 0 & 4 & 12 \end{bmatrix} \begin{bmatrix} F_1 \\ F_2 \\ F_3 \end{bmatrix} = \begin{bmatrix} 0 \\ 0 \\ 8/27 e^3 \\ 0 \\ 28/27 e^3 \end{bmatrix} \tag{2.39}$$

If we evaluate the ranks of the equations:

$$rankA \equiv rank \begin{bmatrix} 2 & -52 & 128 \\ 0 & 4 & -16 \\ 0 & 8 & 0 \\ 1 & -4 & -24 \\ 0 & 4 & 12 \end{bmatrix} = 3 \tag{2.40}$$

$$rankB \equiv rank \begin{bmatrix} 2 & -52 & 128 & 0 \\ 0 & 4 & -16 & 0 \\ 0 & 8 & 0 & 8/27 e^3 \\ 1 & -4 & -24 & 0 \\ 0 & 4 & 12 & 28/27 e^3 \end{bmatrix} = 4 \tag{2.41}$$

There is no solution for F_k because $rankA < rankB$. *RankA* does not increase even if double, triple or more speed particle velocities are added to the basic ones. *RankA* remains unchanged because only linearly dependent row vectors are added to the matrix. Therefore, although the other groups: c_k^0, c_k^2, c_k^4, and c_k^8, meet the requirement, $rankA = rankB$, failure to meet the requirement in group c_k^6 makes the equation as a whole unsolvable. It can be concluded that it is impossible to construct a three-dimensional model.

Is a model in two dimensions possible? The constraints are summarized in Table 2.4. It is easy to confirm that each group meets the requirement, $rankA = rankB$.

$$\begin{aligned} &rankA = rankB = 1 \quad \text{for group } c_k^0 \\ &rankA = rankB = 1 \quad \text{for group } c_k^2 \\ &rankA = rankB = 2 \quad \text{for group } c_k^4 \\ &rankA = rankB = 2 \quad \text{for group } c_k^6 \\ &rankA = rankB = 2 \quad \text{for group } c_k^8 \end{aligned} \tag{2.42 abcde}$$

Whole equations, as a set of equations, are solvable when we add necessary number of multiple speeds of basic particle velocities, because the rank can increase beyond the groups. It can be concluded that it is possible to construct a two-dimensional model.

The following is an example that demonstrates the constructibility of a two-dimensional model. As there are eight linearly independent constraints, a model using a rest particle and seven groups of moving particles, as shown in Figure 2.3, was constructed. The results for coefficients F_k are as follows:

$$F_{11} = \frac{1}{60}(-24e^4 + 85e^3 - 106e^2 + 48e) \tag{2.43}$$

$$F_{12} = \frac{1}{240}(24e^4 - 80e^3 + 89e^2 - 24e) \tag{2.44}$$

$$F_{13} = \frac{1}{11340}(-264e^4 + 735e^3 - 574e^2 + 144e) \tag{2.45}$$

$$F_{14} = \frac{1}{13440}(36e^4 - 70e^3 + 49e^2 - 12e) \tag{2.46}$$

$$F_{21} = \frac{1}{32}(4e^4 - 13e^3 + 12e^2) \tag{2.47}$$

$$F_{22} = \frac{1}{320}(-4e^4 + 10e^3 - 3e^2) \tag{2.48}$$

$$F_{23} = \frac{1}{12960}(12e^4 - 15e^3 + 4e^2) \tag{2.49}$$

$$F_0 = 1 - 4(F_{11} + F_{12} + F_{13} + F_{14} + F_{21} + F_{22} + F_{23}) \tag{2.50}$$

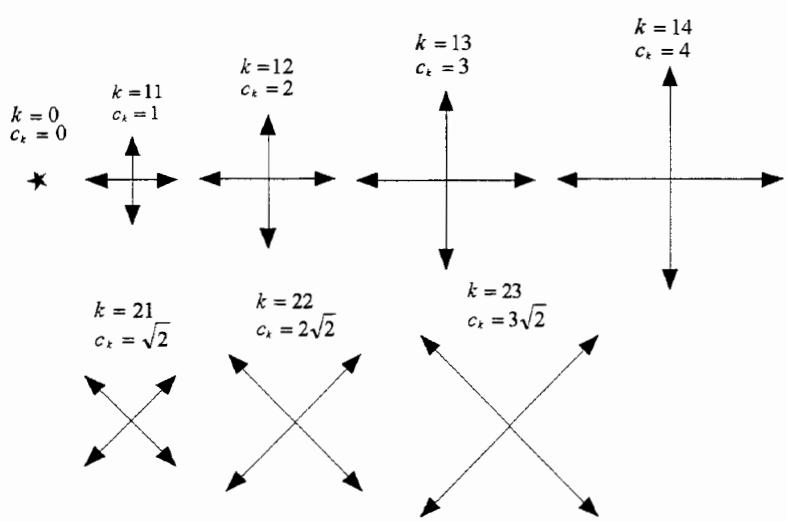

Figure 2.3. Particle velocities used in the two-dimensional model proposed in this paper. They consist of a rest particle and seven groups of moving particles.

Table 2.3. Constraints for the coefficients F_k in the three-dimensional model that has global coefficients. X_k represents $b_k, \chi_k, \varphi_k \cdots, \mathrm{B}_k$. For example, the constraint equation for group c_k^2 is written as $2F_1 + 8F_2 + 8F_3 = \frac{2}{3}e$

	Constraint	X_k			value
c_k^0	$\sum_k b_k F_k$	6	12	8	1
c_k^2	$\sum_k \chi_k F_k$	2	8	8	$\frac{2}{3}e$
c_k^4	$\sum_k \psi_k F_k$	2	−4	−16	0
	$\sum_k \varphi_k F_k$	0	4	8	$\frac{4}{9}e^2$
	$\sum_k \Gamma_k F_k$	1	8	12	$\frac{10}{9}e^2$
c_k^6	$\sum_k \Lambda_k F_k$	2	−52	128	0
	$\sum_k \Omega_k F_k$	0	4	−16	0
	$\sum_k \Theta_k F_k$	0	8	0	$\frac{8}{27}e^3$
	$\sum_k \Xi_k F_k$	1	−4	−24	0
	$\sum_k \Pi_k F_k$	0	4	12	$\frac{28}{27}e^3$
c_k^8	$\sum_k \mathrm{Z}_k F_k$	1	−52	192	0
	$\sum_k \mathrm{N}_k F_k$	0	4	−24	0
	$\sum_k \mathrm{B}_k F_k$	0	8	0	$\frac{8}{9}e^4$

Table 2.4. Constraints for the coefficients F_k in the two-dimensional model that has global coefficients.

	Constraint	X_k		value
C_k^0	$\sum_k b_k F_k$	4	4	1
C_k^2	$\sum_k \chi_k F_k$	2	4	e
C_k^4	$\sum_k \psi_k F_k$	2	−8	0
	$\sum_k \varphi_k F_k$	0	4	e^2
	$\sum_k \Gamma_k F_k$	1	4	$2e^2$
C_k^6	$\sum_k \Lambda_k F_k$	2	−16	0
	$\sum_k \Omega_k F_k$	0	0	0
	$\sum_k \Theta_k F_k$	0	$4/3$	e^3
	$\sum_k \Xi_k F_k$	1	−8	0
	$\sum_k \Pi_k F_k$	0	4	$3e^3$
C_k^8	$\sum_k \mathrm{Z}_k F_k$	1	−16	0
	$\sum_k \mathrm{N}_k F_k$	0	0	0
	$\sum_k \mathrm{B}_k F_k$	0	$4/3$	$4e^4$

2.3.2. Deriving a model that has distributed coefficients

Chen et al.[2] define the local equilibrium distribution function as follows. The distribution function has weighting coefficients on each of the terms.

$$f_{ki}^{(0)} = \rho[A_k + M_k c_{ki\xi} u_\xi + G_k u^2 + J_k c_{ki\xi} c_{ki\eta} u_\xi u_\eta + Q_k c_{ki\xi} u_\xi u^2 + H_k c_{ki\xi} c_{ki\eta} c_{ki\zeta} u_\xi u_\eta u_\zeta + R_k c_{ki\xi} c_{ki\eta} u_\xi u_\eta u^2 + S_k u^4] \tag{2.51}$$

Weighting coefficients $A_k, M_k, \cdots$ are written as polynomial forms of internal energy e.

$$X_k = \sum_{l=0}^{2} x_{kl} e^l \tag{2.52}$$

Local equilibrium distribution function (2.51) is applied to conditions (2.1) through (2.7). Considering tensor expressions (2.8) through (2.15), Table 2.5 for the constraints on the weighting coefficients is obtained.

In two dimensions, looking at Table 2.1, the following linearly dependent relations can be recognized. Even if double, triple or more speed particle velocities are added to the basic ones, the same linear dependency still holds because $\Gamma_k, \psi_k, \varphi_k$ belong to the same group c_k^4, and $\Xi_k, \Lambda_k, \Pi_k, \Theta_k$ to the same group c_k^6.

$$2\Gamma_k = \psi_k + 4\varphi_k \tag{2.53}$$

$$2\Xi_k = \Lambda_k \tag{2.54}$$

$$\Pi_k = 3\Theta_k \tag{2.55}$$

Therefore, the following equations hold:

$$2\sum_k \Gamma_k x_{kl} = \sum_k \psi_k x_{kl} + 4\sum_k \varphi_k x_{kl} \tag{2.56}$$

$$2\sum_k \Xi_k x_{kl} = \sum_k \Lambda_k x_{kl} \tag{2.57}$$

$$\sum_k \Pi_k x_{kl} = 3\sum_k \Theta_k x_{kl} \tag{2.58}$$

Requiring anisotropic terms $\sum_k \psi_k x_{kl}$ vanish and $Y_4 = 1/2$, the constraints of Table 2.5 are transformed into those of Table 2.6, which is exactly equivalent to TABLE II in Chen et al.'s paper.[2] The constraints of Table 2.6 are solvable because the ranks of all groups meet the requirement, $rankA = rankB$.

$$
\begin{aligned}
&rankA = rankB = 1 \quad \text{for group } c_k^{\,0} \\
&rankA = rankB = 1 \quad \text{for group } c_k^{\,2} \\
&rankA = rankB = 2 \quad \text{for group } c_k^{\,4} \\
&rankA = rankB = 2 \quad \text{for group } c_k^{\,6}
\end{aligned}
\tag{2.59 abcd}
$$

It can be concluded that it is possible to construct a two-dimensional model.

However, the situations in three dimensions are different. Linear dependencies (2.53) through (2.55) do not hold in three dimensions. Therefore, it is necessary to return to the original constraints in Table 2.5. When D=3 is substituted, Table 2.7 is obtained. The constraints for groups $c_k^{\,0}$ and $c_k^{\,2}$ clearly meet the requirement, $rankA = rankB$. For group $c_k^{\,4}$, the constraints, except for Q_k, meet the requirement as follows.

$$
rank\begin{bmatrix} 2 & -4 & -16 \\ 0 & 4 & 8 \\ 1 & 8 & 12 \end{bmatrix} = 2 \tag{2.60}
$$

$$
rank\begin{bmatrix} 2 & -4 & -16 & 0 \\ 0 & 4 & 8 & 0 \\ 1 & 8 & 12 & 0 \end{bmatrix} = rank\begin{bmatrix} 2 & -4 & -16 & 0 \\ 0 & 4 & 8 & \frac{2}{3} \\ 1 & 8 & 12 & \frac{5}{3} \end{bmatrix} = rank\begin{bmatrix} 2 & -4 & -16 & 0 \\ 0 & 4 & 8 & \frac{1}{2} \\ 1 & 8 & 12 & \frac{5}{4} \end{bmatrix} = 2 \tag{2.61}
$$

However, $rankB$ for Q_k depends on the value of Y_4. To be solvable, the rank must have a value of two.

$$
rank\begin{bmatrix} 2 & -4 & -16 & 0 \\ 0 & 4 & 8 & -\frac{1}{2} \\ 1 & 8 & 12 & \frac{1}{2} - 3Y_4 \end{bmatrix} = 2 \tag{2.62}
$$

Above requirement is satisfied if Y_4 has the following value:

$$
Y_4 = \frac{7}{12} \tag{2.63}
$$

For group $c_k^{\,6}$, $rankA$ obviously has a value of three.

$$
rank\begin{bmatrix} 2 & -52 & 128 \\ 0 & 4 & -16 \\ 0 & 8 & 0 \\ 1 & -4 & -24 \\ 0 & 4 & 12 \end{bmatrix} = 3 \tag{2.64}
$$

RankB for H_k has the following value if the value (2.63) is substituted:

$$rank\begin{bmatrix} 2 & -52 & 128 & 0 \\ 0 & 4 & -16 & 0 \\ 0 & 8 & 0 & \frac{1}{6} \\ 1 & -4 & -24 & 0 \\ 0 & 4 & 12 & \frac{7}{12} \end{bmatrix} = 4 \tag{2.65}$$

Therefore, the constraint equations for group c_k^6 are unsolvable. It can be concluded that it is impossible to construct a three-dimensional model.

TABLE Ⅱ in Chen et al.'s paper[2] is no more valid in three dimensions. Consequently, the coefficients for 3D40V in TABLE Ⅲ in their paper do not give correct fluid equations.

Table 2.5. Constraints for the model that has distributed coefficients. x_{kl} represents $a_{k0}, a_{k1}, \cdots, s_{k0}$. For example, the second equation for a_{kl} is written as $\sum_k \chi_k a_{k1} = \frac{2}{D}$. Constraints for j_{k0} and g_{k0} are related through Y_0. For example, if Y_0 is calculated by known j_{k0}, Y_0 becomes the constraint for g_{k0} as $\sum_k b_k g_{k0} = -Y_0$.

	Constraint	A_k			M_k		J_k		G_k		H_k	Q_k	R_k	S_k
		a_{k0}	a_{k1}	a_{k2}	m_{k0}	m_{k1}	j_{k0}	j_{k1}	g_{k0}	g_{k1}	h_{k0}	q_{k0}	r_{k0}	s_{k0}
c_k^0	$\sum_k b_k x_{kl}$	1	0	0					$-Y_0$	$-Y_1$				$-Y_3$
c_k^2	$\sum_k \chi_k x_{kl}$	0	$\frac{2}{D}$	0	1	0	Y_0	Y_1	$-\frac{1}{2}$	0		$-3Y_2$	Y_3	0
c_k^4	$\sum_k \psi_k x_{kl}$				0	0	0	0			0	0	0	
	$\sum_k \varphi_k x_{kl}$				0	$\frac{2}{D}$	$\frac{1}{2}$	0			Y_2	$-\frac{1}{2}$	0	
	$\sum_k \Gamma_k x_{kl}$	0	0	$\frac{2(D+2)}{D^2}$	0	$\frac{D+2}{D}$	$\frac{D+2}{4}$	0	0	$-\frac{D+2}{2D}$		$\frac{1}{2}-3Y_4$	0	$-\frac{1}{4}$
c_k^6	$\sum_k \Lambda_k x_{kl}$										0			
	$\sum_k \Omega_k x_{kl}$										0			
	$\sum_k \Theta_k x_{kl}$										$\frac{1}{6}$			
	$\sum_k \Xi_k x_{kl}$						0	0			0		0	
	$\sum_k \Pi_k x_{kl}$						0	$\frac{D+4}{2D}$			Y_4		$\frac{1}{4}$	

Table 2.6. Constraints for the two-dimensional model that has distributed coefficients.

	Constraint	X_k		A_k			M_k		J_k		G_k		H_k	Q_k	R_k	S_k
				a_{k0}	a_{k1}	a_{k2}	m_{k0}	m_{k1}	j_{k0}	j_{k1}	g_{k0}	g_{k1}	h_{k0}	q_{k0}	r_{k0}	s_{k0}
c_k^0	$\sum_k b_k x_{kl}$	4	4	1	0	0					$-Y_0$	$-Y_1$				$-Y_3$
c_k^2	$\sum_k \chi_k x_{kl}$	2	4	0	1	0	1	0	Y_0	Y_1	$-\frac{1}{2}$	0		$-3Y_2$	Y_3	0
c_k^4	$\sum_k \psi_k x_{kl}$	2	−8	0	0	0	0	0	0	0	0	0	0	0	0	0
	$\sum_k \varphi_k x_{kl}$	0	4	0	0	1	0	1	$\frac{1}{2}$	0	0	$-\frac{1}{2}$	Y_2	$-\frac{1}{2}$	0	$-\frac{1}{8}$
c_k^6	$\sum_k \Lambda_k x_{kl}$	2	−16						0	0			0		0	
	$\sum_k \Omega_k x_{kl}$	0	0													
	$\sum_k \Theta_k x_{kl}$	0	$\frac{4}{3}$						0	$\frac{1}{2}$			$\frac{1}{6}$		$\frac{1}{12}$	

Table 2.7. Constraints for the three-dimensional model that has distributed coefficients.

	Constraint	X_k			A_k			M_k		J_k		G_k		H_k	Q_k	R_k	S_k
					a_{k0}	a_{k1}	a_{k2}	m_{k0}	m_{k1}	j_{k0}	j_{k1}	g_{k0}	g_{k1}	h_{k0}	q_{k0}	r_{k0}	s_{k0}
c_k^0	$\sum_k b_k x_{kl}$	6	12	8	1	0	0					$-Y_0$	$-Y_1$				$-Y_3$
c_k^2	$\sum_k \chi_k x_{kl}$	2	8	8	0	$\frac{2}{3}$	0	1	0	Y_0	Y_1	$-\frac{1}{2}$	0		$-3Y_2$	Y_3	0
c_k^4	$\sum_k \psi_k x_{kl}$	2	−4	−16				0	0	0	0			0	0	0	
	$\sum_k \varphi_k x_{kl}$	0	4	8				0	$\frac{2}{3}$	$\frac{1}{2}$	0			Y_2	$-\frac{1}{2}$	0	
	$\sum_k \Gamma_k x_{kl}$	1	8	12	0	0	$\frac{10}{9}$	0	$\frac{5}{3}$	$\frac{5}{4}$	0	0	$-\frac{5}{6}$		$\frac{1}{2}-3Y_4$	0	$-\frac{1}{4}$
c_k^6	$\sum_k \Lambda_k x_{kl}$	2	−52	128										0			
	$\sum_k \Omega_k x_{kl}$	0	4	−16										0			
	$\sum_k \Theta_k x_{kl}$	0	8	0										$\frac{1}{6}$			
	$\sum_k \Xi_k x_{kl}$	1	−4	−24						0	0			0		0	
	$\sum_k \Pi_k x_{kl}$	0	4	12						0	$\frac{7}{6}$			Y_4		$\frac{1}{4}$	

2.4. Verification of the new two-dimensional model

The two-dimensional thermal model constructed in section 2.3.1 was evaluated by Couette flow simulation. The simulation was conducted using following finite difference scheme:

$$\frac{\partial f_{ki}}{\partial t} + c_{ki\alpha}\frac{\partial f_{ki}}{\partial r_\alpha} = -\frac{1}{\phi}(f_{ki} - f_{ki}^{(0)}) \tag{2.66}$$

where f_{ki} is the distribution function for the particle velocity c_{ki}, t the time, r_α the spatial coordinate, and ϕ the relaxation parameter.

The upper wall, which is H apart from the lower wall and has internal energy e_2, starts to move at speed U. The lower wall has e_1 and is at rest (Figure 2.4). Internal energy distribution e along vertical axis y in a steady state is given as:

$$e = e_1 + (e_2 - e_1)\frac{y}{H} + \frac{\mu}{2\kappa'}U^2\frac{y}{H}(1 - \frac{y}{H}) \tag{2.67}$$

Since viscous coefficients μ and thermal conductivity κ' are given as the following equations:

$$\mu = \rho e \phi \tag{2.68}$$

$$\kappa' = 2\rho e \phi \tag{2.69}$$

value $\mu/2\kappa'$ is constant ($= 1/4$). Therefore, the distribution does not depend on relaxation parameter ϕ or on internal energy e.

Figure 2.5 shows the results for internal energy distribution in a steady state for various relaxation parameters. In the figure, the internal energy subtracted by linear distribution, which corresponds to the last term of equation (2.67), is shown. Figure 2.6 show the results for the internal energy distribution in a steady state for various wall temperatures. Both results agree completely with the analysis.

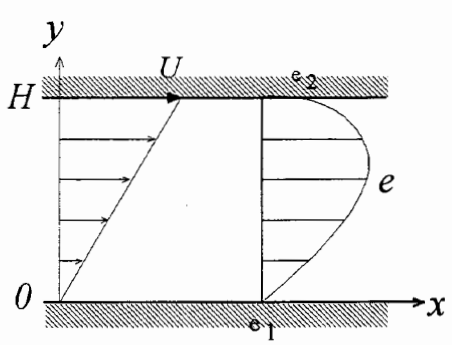

Figure 2.4. Couette flow simulation. The upper wall, which is H apart from the lower wall and has internal energy e_2, starts to move at speed U. The lower wall has e_1 and is at rest.

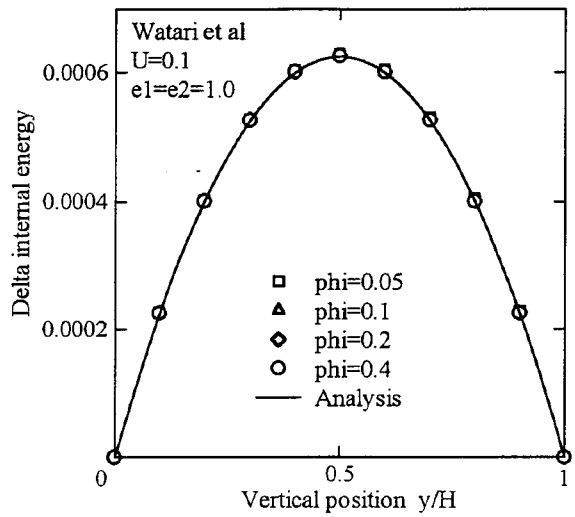

Figure 2.5. Internal energy distribution at steady state for various relaxation parameters: ϕ=0.05, 0.1, 0.2, 0.4. U=0.1, e_1=e_2=1.0. The internal energy subtracted by linear distribution is shown. The results for all ϕ overlap each other.

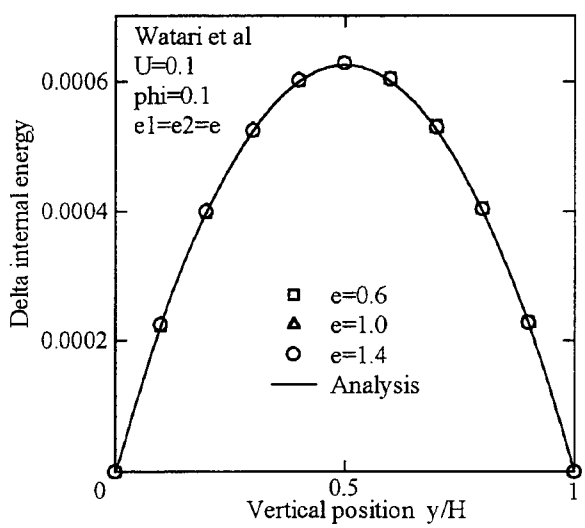

Figure 2.6. Internal energy distribution at steady state for various wall temperatures: e_1=e_2=0.6, 1.0, 1.4. U=0.1, ϕ=0.1. The internal energy subtracted by linear distribution is shown. The results for all cases overlap each other.

2.5. Conclusions

It is possible to construct a thermally correct two-dimensional LBM multi-speed model that has a single relaxation (BGK model). However, a correct three-dimensional LBM multi-speed thermal model is theoretically impossible. In addition, these results do not change for the types of local equilibrium distribution function.

A correct two-dimensional LBM multi-speed thermal model that has global coefficients in the local equilibrium distribution function was derived. The model was evaluated by Couette flow simulation. The result showed exact agreement with the analysis.

References

[1] F. J. Alexander, S. Chen and J. D. Sterling, "Lattice Boltzmann thermo-hydrodynamics", Phys. Rev. E **47**: R2249-52 (1993).

[2] Y. Chen, H. Ohashi and M. Akiyama, "Thermal lattice BGK model without nonlinear deviations in macrodynamic equations", Phys. Rev. E **50**: 2776-83 (1994).

[3] N. Takada, Y. Yamakoshi and M. Tsutahara, "Numerical Analysis of fluid motions by three-dimensional thermal lattice Boltzmann model", JSME B **64**, 628: 4-11 (1998) (in Japanese).

[4] S. Wolfram, "Cellular automaton fluids 1: Basic Theory", J. Stat. Phys. **45**: 471-526 (1986).

3. Two-dimensional thermal model of finite difference lattice Boltzmann method with high spatial isotropy

3.1. Introduction

The lattice Boltzmann method (LBM) has become a powerful numerical tool for simulating fluid flows.[1] In the LBM, there are two ways of handling thermal fluids. One is the so-called "multi-component thermal model,"[2] where heat is handled as different component from fluid. This model characterizes the flow as Boussinesq fluid. Another is the so-called "multi-speed thermal model,"[3,4] where particle velocities that have different speeds are used. While the multi-speed thermal model is intended to correctly represent heat characteristics and compressibility, existing models seem to have hidden error terms and show a limited accuracy.

The finite difference lattice Boltzmann method (FDLBM)[5] was proposed in order to secure numerical stability and to apply non-uniform grids. In the LBM, particle velocities are restricted to those that exactly link the lattice nodes in unit time. On the other hand, in the FDLBM as we do not need to consider that constraint, we can select particle velocities independently from the lattice configuration. Therefore, a correct and numerically stable multi-speed thermal model can be constructed by adopting more isotropic particle velocities. This paper proposes a two-dimensional FDLBM BGK (single relaxation) model based on the above concept.

3.2. Finite difference lattice Boltzmann method

Below is a general description of the two-dimensional thermal FDLBM model. The evolution of the distribution function f_{ki} for particle velocity c_{ki} is governed by the following equation, which is solved using Euler and second upwind difference scheme.

$$\frac{\partial f_{ki}}{\partial t} + c_{ki\alpha}\frac{\partial f_{ki}}{\partial r_\alpha} = -\frac{1}{\phi}(f_{ki} - f_{ki}^{(0)}) \tag{3.1}$$

where the subscript k indicates a group of particle velocities whose speed c_k and i indicates the particle velocity's direction. The subscript α indicates x or y component. The variable t is time, r_α the spatial coordinate, $f_{ki}^{(0)}$ the local equilibrium distribution function, and ϕ the relaxation parameter.

Macroscopic quantities, the density ρ, the velocity u_α, and the internal energy e, are defined as follows.

$$\rho = \sum_{ki} f_{ki} \tag{3.2}$$

$$\rho u_\alpha = \sum_{ki} f_{ki} c_{ki\alpha} \tag{3.3}$$

$$\rho(e+\frac{u^2}{2})=\sum_{ki} f_{ki}\frac{c_k^2}{2} \tag{3.4}$$

The local equilibrium distribution function is determined to satisfy the following moment summation equations.

$$\sum_{ki} f_{ki}^{(0)} = \rho \tag{3.5}$$

$$\sum_{ki} f_{ki}^{(0)} c_{ki\alpha} = \rho u_\alpha \tag{3.6}$$

$$\sum_{ki} f_{ki}^{(0)} c_{ki\alpha} c_{ki\beta} = \rho(e\delta_{\alpha\beta} + u_\alpha u_\beta) \tag{3.7}$$

$$\sum_{ki} f_{ki}^{(0)} c_{ki\alpha} c_{ki\beta} c_{ki\gamma} = \rho[e(u_\alpha\delta_{\beta\gamma} + u_\beta\delta_{\gamma\alpha} + u_\gamma\delta_{\alpha\beta}) + u_\alpha u_\beta u_\gamma] \tag{3.8}$$

$$\sum_{ki} f_{ki}^{(0)} \frac{c_k^2}{2} = \rho(e+\frac{u^2}{2}) \tag{3.9}$$

$$\sum_{ki} f_{ki}^{(0)} \frac{c_k^2}{2} c_{ki\alpha} = \rho u_\alpha (2e+\frac{u^2}{2}) \tag{3.10}$$

$$\sum_{ki} f_{ki}^{(0)} \frac{c_k^2}{2} c_{ki\alpha} c_{ki\beta} = \rho[e(2e+\frac{u^2}{2})\delta_{\alpha\beta} + u_\alpha u_\beta (3e+\frac{u^2}{2})] \tag{3.11}$$

By applying the Chapman-Enskog expansion, the above formulation is shown to be equivalent to the following fluid equations (Navier-Stokes equations).

$$\frac{\partial\rho}{\partial t}+\frac{\partial}{\partial r_\alpha}(\rho u_\alpha)=0 \tag{3.12}$$

$$\frac{\partial}{\partial t}(\rho u_\alpha)+\frac{\partial}{\partial r_\beta}(\rho u_\alpha u_\beta + P\delta_{\alpha\beta})-\frac{\partial}{\partial r_\beta}[\mu(\frac{\partial u_\beta}{\partial r_\alpha}+\frac{\partial u_\alpha}{\partial r_\beta}-\frac{\partial u_\gamma}{\partial r_\gamma}\delta_{\alpha\beta})]=0 \tag{3.13}$$

$$\frac{\partial}{\partial t}[\rho(e+\frac{u^2}{2})]+\frac{\partial}{\partial r_\alpha}[\rho u_\alpha(e+\frac{u^2}{2}+\frac{P}{\rho})]-\frac{\partial}{\partial r_\alpha}[\kappa'\frac{\partial e}{\partial r_\alpha}+\mu u_\beta(\frac{\partial u_\beta}{\partial r_\alpha}+\frac{\partial u_\alpha}{\partial r_\beta}-\frac{\partial u_\gamma}{\partial r_\gamma}\delta_{\alpha\beta})]=0 \tag{3.14}$$

where the pressure P, the viscosity coefficient μ, and the heat conductivity κ' have the following relations.

$$P = \rho e \tag{3.15}$$

$$\mu = \rho e \phi \tag{3.16}$$

$$\kappa' = 2\rho e\phi \tag{3.17}$$

Temperature T is related with the internal energy by the following equation (R: gas constant).

$$T = e/R \tag{3.18}$$

3.3. New FDLBM model derivation

The nth rank tensor for the group of m particle velocities is defined as

$$E^{(n)}_{\alpha_1\alpha_2\alpha_3\cdots\alpha_n} = \sum_{i=1}^{m} c_{i\alpha_1} c_{i\alpha_2} c_{i\alpha_3} \cdots c_{i\alpha_n} \tag{3.19}$$

where $\alpha_1,..,\alpha_n$ indicate either x or y component. The tensor is isotropic if it is invariant for the coordinate rotation and the reflection. As for being isotropic, the odd rank tensors should vanish and the even rank tensors should be sums of all possible products of Kronecker delta.[6]

The tensors for four groups shown in Figure 3.1 are summarized in Table 3.1. Kronecker delta $\delta_{\alpha\beta}$, the sum of its products, $\Delta^{(4)}_{\alpha\beta\gamma\chi}$ and $\Delta^{(6)}_{\alpha\beta\gamma\chi\lambda\tau}$, are isotropic, whereas extended Kronecker deltas, $\delta_{\alpha\beta\gamma\chi}$ and $\delta_{\alpha\beta\gamma\chi\lambda\tau}$, are anisotropic.

The odd tensors for uniformly distributed particle velocities are shown to vanish. For even tensors, Groups I and II yield anisotropic tensors for the fourth rank and higher. Group III ensures isotropy up-to the fourth rank but not for higher ranks. However, Group IV ensures isotropy up-to the seventh rank.

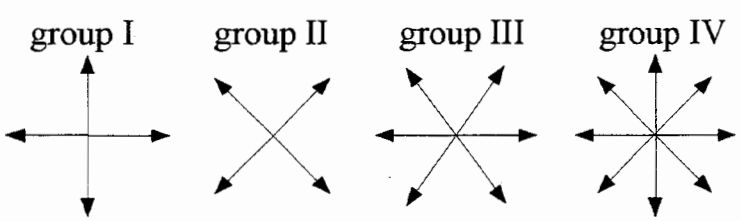

Figure 3.1. Four groups of particle velocities.

Table 3.1. Tensors for four groups of particle velocities shown in Figure 3.1.

$\delta_{\alpha\beta}$=1 (if $\alpha=\beta$), =0 (otherwise)

$\delta_{\alpha\beta\gamma\chi}$=1 (if $\alpha=\beta=\gamma=\chi$), =0 (otherwise)

$\delta_{\alpha\beta\gamma\chi\lambda\tau}$=1 (if $\alpha=\beta=\gamma=\chi=\lambda=\tau$), =0 (otherwise)

$\Delta^{(4)}_{\alpha\beta\gamma\chi}=\delta_{\alpha\beta}\delta_{\gamma\chi}+\delta_{\alpha\gamma}\delta_{\beta\chi}+\delta_{\alpha\chi}\delta_{\beta\gamma}$

$\Delta^{(6)}_{\alpha\beta\gamma\chi\lambda\tau}=\delta_{\alpha\beta}\Delta^{(4)}_{\gamma\chi\lambda\tau}+\delta_{\alpha\gamma}\Delta^{(4)}_{\beta\chi\lambda\tau}+\delta_{\alpha\chi}\Delta^{(4)}_{\beta\gamma\lambda\tau}+\delta_{\alpha\lambda}\Delta^{(4)}_{\beta\gamma\chi\tau}+\delta_{\alpha\tau}\Delta^{(4)}_{\beta\gamma\chi\lambda}$

	$\sum_i c_{ki\alpha}$	$\sum_i c_{ki\alpha}c_{ki\beta}$	$\sum_i c_{ki\alpha}c_{ki\beta}c_{ki\gamma}$	$\sum_i c_{ki\alpha}c_{ki\beta}c_{ki\gamma}c_{ki\chi}$	$\sum_i c_{ki\alpha}c_{ki\beta}c_{ki\gamma}c_{ki\chi}c_{ki\lambda}$	$\sum_i c_{ki\alpha}c_{ki\beta}c_{ki\gamma}c_{ki\chi}c_{ki\lambda}c_{ki\tau}$
GROUP I	0	$2c_k^2\delta_{\alpha\beta}$	0	$2c_k^4\delta_{\alpha\beta\gamma\chi}$	0	$2c_k^6\delta_{\alpha\beta\gamma\chi\lambda\tau}$
GROUP II	0	$2c_k^2\delta_{\alpha\beta}$	0	$c_k^4(\Delta_{\alpha\beta\gamma\chi}-2\delta_{\alpha\beta\gamma\chi})$	0	$c_k^6(\frac{1}{6}\Delta^{(6)}_{\alpha\beta\gamma\chi\lambda\tau}-2\delta_{\alpha\beta\gamma\chi\lambda\tau})$
GROUP III	0	$3c_k^2\delta_{\alpha\beta}$	0	$\frac{3}{4}c_k^4\Delta^{(4)}_{\alpha\beta\gamma\chi}$	0	*anisotropic*
GROUP IV	0	$4c_k^2\delta_{\alpha\beta}$	0	$c_k^4\Delta^{(4)}_{\alpha\beta\gamma\chi}$	0	$\frac{1}{6}c_k^6\Delta^{(6)}_{\alpha\beta\gamma\chi\lambda\tau}$

Energy diffusion equation (3.11) contains up-to fourth order of flow velocity u. Consequently, the local equilibrium distribution function $f_{ki}^{(0)}$ is derived from Maxwellian distribution, retaining up-to fourth order terms of flow velocity.

$$\begin{aligned} f_{ki}^{(0)} &= \frac{\rho}{2\pi e}\exp\left(-\frac{1}{2e}(c_{ki\alpha}-u_\alpha)^2\right) \\ &= \rho\frac{1}{2\pi e}\exp\left(-\frac{1}{2e}c_k^2\right)\exp\left(\frac{1}{e}(c_{ki\alpha}u_\alpha-\frac{u^2}{2})\right) \\ &= \rho F_k[(1-\frac{u^2}{2e}+\frac{u^4}{8e^2})+\frac{1}{e}(1-\frac{u^2}{2e})c_{ki\xi}u_\xi+\frac{1}{2e^2}(1-\frac{u^2}{2e})c_{ki\xi}c_{ki\eta}u_\xi u_\eta \\ &\quad +\frac{1}{6e^3}c_{ki\xi}c_{ki\eta}c_{ki\zeta}u_\xi u_\eta u_\zeta+\frac{1}{24e^4}c_{ki\xi}c_{ki\eta}c_{ki\zeta}c_{ki\chi}u_\xi u_\eta u_\zeta u_\chi]+o(u^5) \end{aligned} \tag{3.20}$$

where the parameter F_k represents the term $\frac{1}{2\pi e}\exp\left(-\frac{1}{2e}c_k^2\right)$ and is the function of e and c_k.

The local equilibrium distribution function $f_{ki}^{(0)}$ contains the fourth rank tensor and momentum diffusion equation (3.8) contains the third rank tensor. Therefore, up-to seventh rank tensor should be isotropic to recover correct fluid equations.

When we apply the property that the odd tensors vanish, we obtain the following equations to determine the parameters F_k.

From equation (3.5),

$$\sum_{ki}F_k=1 \tag{3.21}$$

$$\sum_{ki}F_k c_{ki\xi}c_{ki\zeta}u_\xi u_\zeta=eu^2 \tag{3.22}$$

$$\sum_{ki} F_k c_{ki\xi} c_{ki\zeta} c_{ki\eta} c_{ki\chi} u_\xi u_\zeta u_\eta u_\chi = 3e^2 u^4 \tag{3.23}$$

From equation (3.6),

$$\sum_{ki} F_k c_{ki\alpha} c_{ki\xi} u_\xi = e u_\alpha \tag{3.24}$$

$$\sum_{ki} F_k c_{ki\alpha} c_{ki\xi} c_{ki\zeta} c_{ki\eta} u_\xi u_\zeta u_\eta = 3e^2 u^2 u_\alpha \tag{3.25}$$

From equation (3.7),

$$\sum_{ki} F_k c_{ki\alpha} c_{ki\beta} = e\delta_{\alpha\beta} \tag{3.26}$$

$$\sum_{ki} F_k c_{ki\alpha} c_{ki\beta} c_{ki\xi} c_{ki\zeta} u_\xi u_\zeta = e^2 (u^2 \delta_{\alpha\beta} + 2u_\alpha u_\beta) \tag{3.27}$$

$$\sum_{ki} F_k c_{ki\alpha} c_{ki\beta} c_{ki\xi} c_{ki\zeta} c_{ki\eta} c_{ki\chi} u_\xi u_\zeta u_\eta u_\chi = 3e^3 u^2 (u^2 \delta_{\alpha\beta} + 4u_\alpha u_\beta) \tag{3.28}$$

From equation (3.8),

$$\sum_{ki} F_k c_{ki\alpha} c_{ki\beta} c_{ki\gamma} c_{ki\xi} u_\xi = e^2 (u_\alpha \delta_{\beta\gamma} + u_\beta \delta_{\gamma\alpha} + u_\gamma \delta_{\alpha\beta}) \tag{3.29}$$

$$\sum_{ki} F_k c_{ki\alpha} c_{ki\beta} c_{ki\gamma} c_{ki\xi} c_{ki\zeta} c_{ki\eta} u_\xi u_\zeta u_\eta = 3e^3 u^2 (u_\alpha \delta_{\beta\gamma} + u_\beta \delta_{\gamma\alpha} + u_\gamma \delta_{\alpha\beta}) + 6e^3 u_\alpha u_\beta u_\gamma \tag{3.30}$$

From equation (3.9),

$$\sum_{ki} F_k \frac{c_k^2}{2} = e \tag{3.31}$$

$$\sum_{ki} F_k \frac{c_k^2}{2} c_{ki\xi} c_{ki\zeta} u_\xi u_\zeta = 2e^2 u^2 \tag{3.32}$$

$$\sum_{ki} F_k \frac{c_k^2}{2} c_{ki\xi} c_{ki\zeta} c_{ki\eta} c_{ki\chi} u_\xi u_\zeta u_\eta u_\chi = 9e^3 u^4 \tag{3.33}$$

From equation (3.10),

$$\sum_{ki} F_k \frac{c_k^2}{2} c_{ki\alpha} c_{ki\xi} u_\xi = 2e^2 u_\alpha \tag{3.34}$$

$$\sum_{ki} F_k \frac{c_k^2}{2} c_{ki\alpha} c_{ki\xi} c_{ki\zeta} c_{ki\eta} u_\xi u_\zeta u_\eta = 9e^3 u^2 u_\alpha \tag{3.35}$$

From equation (3.11),

$$\sum_{ki} F_k \frac{c_k^2}{2} c_{ki\alpha} c_{ki\beta} = 2e^2 \delta_{\alpha\beta} \tag{3.36}$$

$$\sum_{ki} F_k \frac{c_k^2}{2} c_{ki\alpha} c_{ki\beta} c_{ki\xi} c_{ki\zeta} u_\xi u_\zeta = 3e^3 (u^2 \delta_{\alpha\beta} + 2u_\alpha u_\beta) \tag{3.37}$$

$$\sum_{ki} F_k \frac{c_k^2}{2} c_{ki\alpha} c_{ki\beta} c_{ki\xi} c_{ki\zeta} c_{ki\eta} c_{ki\chi} u_\xi u_\zeta u_\eta u_\chi = 12e^4 (u^4 \delta_{\alpha\beta} + 4u^2 u_\alpha u_\beta) \tag{3.38}$$

If we further assume application of Group IV particle velocities that have isotropic tensors up-to the seventh rank, the above eighteen equations reduce to the following five equations.

From equation (3.21),

$$\sum_{ki} F_k = 1 \tag{3.39}$$

From equations (3.22), (3.24), (3.26), (3.31),

$$\sum_{ki} F_k c_k^2 = e/4 \tag{3.40}$$

From equations (3.23), (3.25), (3.27), (3.29), (3.32), (3.34), (3.36),

$$\sum_{ki} F_k c_k^4 = e^2 \tag{3.41}$$

From equations (3.28), (3.30), (3.33), (3.35), (3.37),

$$\sum_{ki} F_k c_k^6 = 6e^3 \tag{3.42}$$

From equation (3.38),

$$\sum_{ki} F_k c_k^8 = 48e^4 \tag{3.43}$$

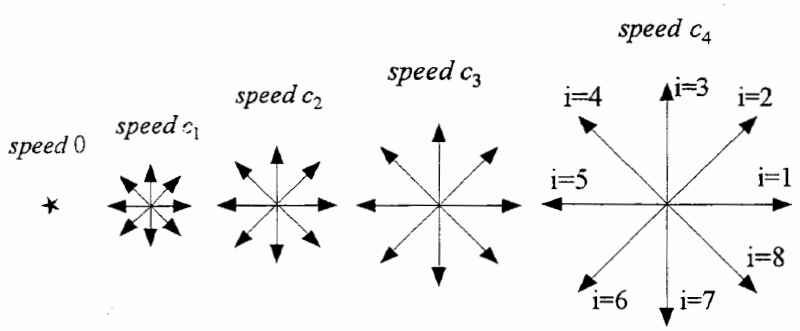

Figure 3.2. Particle velocities of the proposed FDLBM model.

Five speeds are necessary to satisfy the above equations. A rest particle (c_0=0.0) and four group IV particles, whose speed are c_1, c_2, c_3, and c_4, are assumed (Figure 3.2). The equations of (3.39) through (3.43) are easily solved to give the following. The parameters F_k are functions of c_1, c_2, c_3, c_4, and internal energy e.

$$F_1 = \frac{1}{c_1^2(c_1^2-c_2^2)(c_1^2-c_3^2)(c_1^2-c_4^2)}\left[48e^4 - 6(c_2^2+c_3^2+c_4^2)e^3 + (c_2^2c_3^2+c_3^2c_4^2+c_4^2c_2^2)e^2 - \frac{c_2^2c_3^2c_4^2}{4}e\right] \quad (3.44)$$

$$F_2 = \frac{1}{c_2^2(c_2^2-c_3^2)(c_2^2-c_4^2)(c_2^2-c_1^2)}\left[48e^4 - 6(c_3^2+c_4^2+c_1^2)e^3 + (c_3^2c_4^2+c_4^2c_1^2+c_1^2c_3^2)e^2 - \frac{c_3^2c_4^2c_1^2}{4}e\right] \quad (3.45)$$

$$F_3 = \frac{1}{c_3^2(c_3^2-c_4^2)(c_3^2-c_1^2)(c_3^2-c_2^2)}\left[48e^4 - 6(c_4^2+c_1^2+c_2^2)e^3 + (c_4^2c_1^2+c_1^2c_2^2+c_2^2c_4^2)e^2 - \frac{c_4^2c_1^2c_2^2}{4}e\right] \quad (3.46)$$

$$F_4 = \frac{1}{c_4^2(c_4^2-c_1^2)(c_4^2-c_2^2)(c_4^2-c_3^2)}\left[48e^4 - 6(c_1^2+c_2^2+c_3^2)e^3 + (c_1^2c_2^2+c_2^2c_3^2+c_3^2c_1^2)e^2 - \frac{c_1^2c_2^2c_3^2}{4}e\right] \quad (3.47)$$

$$F_0 = 1 - 8(F_1+F_2+F_3+F_4) \quad (3.48)$$

As far as a simulation being stably conducted, the combination of the values, c_1, c_2, c_3, and c_4, does not affect the accuracy itself. We can utilize this freedom to obtain the stably simulated range of temperature as wide as possible. Several criteria were tried and it was finally concluded that following hypothesis has the closest relationship with simulation stability: "Simulation is stable as far as $F_0>F_1>F_2>F_3>F_4>0$." Therefore, the following optimum problem was solved:

Under the condition	$0 < c_1 < c_2 < c_3 < c_4$	
determine	c_1, c_2, c_3, and c_4	
which maximizes	$(e_H-e_L)/e_M$	(3.49)
for $e_L < e < e_H$	$F_0/F_1>1.1$ and $F_1/F_2>1.1$ and	
	$F_2/F_3>1.1$ and $F_3/F_4>1.1$ and $F_4>0$. holds	
keeping	$e_M=(e_H+e_L)/2=1.0$	

The result is the following. The model is expected to stably simulate the flow for the temperature range: e = 0.4~1.6.

$$(c_0, c_1, c_2, c_3, c_4) = (0.0, 1.0, 1.92, 2.99, 4.49) \quad (3.50)$$

$$e_L=0.4\ ,\ e_H=1.6\ ,\quad (e_H-e_L)/e_M = 1.2 \quad (3.51)$$

3.4. Verification of the new model

The model was confirmed valid by conducting two simulations. First, the speed of sound was measured. Second, the shear flow between parallel walls (Couette flow) was investigated.

3.4.1. Speed of sound

In a box, a plate divides fluids that have a small difference in density (Figure 3.3). When the plate is removed, sound waves (expansion and compression) propagate. The position of the pressure jump (Figure 3.4) was measured to calculate the speed of sound. The results at various internal energy levels are shown in Figure 3.5. The simulation was stably conducted for the range: e=0.4~1.6. The speed of sound exactly agrees with the following theoretical value.

$$c_s = \sqrt{2e} \tag{3.52}$$

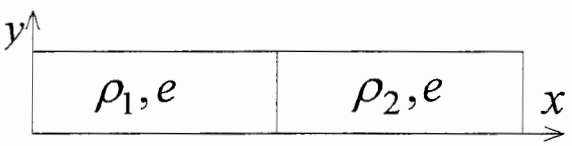

Figure 3.3. Sound wave simulation.
A plate divides fluids that have small difference in density. As the plate is removed, sound waves (expansion or compression) propagate.

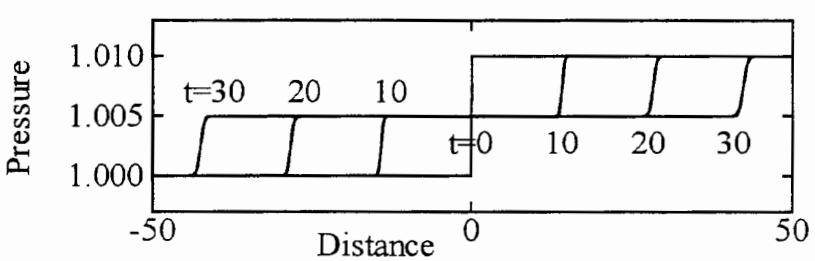

Figure 3.4. Propagation of sound waves.
The pressure jumps advance as time proceeds.

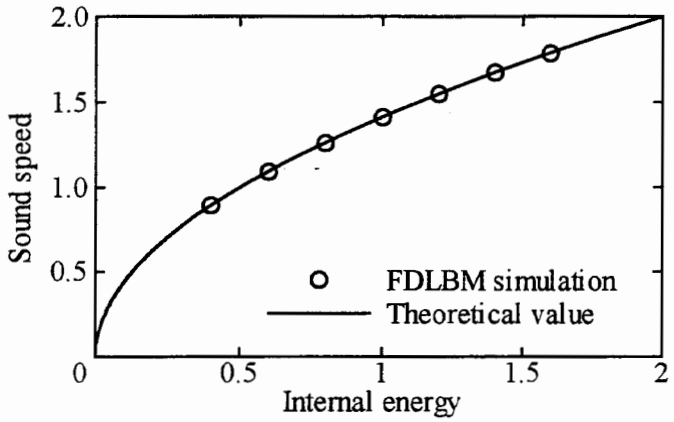

Figure 3.5. Sound speed versus internal energy.

3.4.2. Couette flow

The upper wall, which is H apart from the lower wall and has internal energy e_2, starts to move with speed U. The lower wall has e_1 and is at rest (Figure 3.6). The viscous shear stress transmits momentum into the fluid and changes the horizontal speed profile. The horizontal speed distribution at various instants for $e_1=e_2$ is shown in Figure 3.7. The simulation result exactly agrees with the analytical value of equation (3.53).

$$\frac{u}{U}=\frac{y}{H}-\frac{2}{\pi}\sum_{n=1}^{\infty}\exp\left[-n^2\pi^2\frac{\mu t}{\rho H^2}\right]\sin\left[n\pi(1-\frac{y}{H})\right] \tag{3.53}$$

The analytical distribution of internal energy in a steady state is shown in equation (3.54).

$$e=e_1+(e_2-e_1)\frac{y}{H}+\frac{\mu}{2\kappa'}U^2\frac{y}{H}(1-\frac{y}{H}) \tag{3.54}$$

Since the coefficients μ and κ' are given as (3.16) and (3.17), respectively, value $\mu/2\kappa'$ is constant (=0.25). Therefore, the distribution does not depend on the relaxation parameter ϕ or on the internal energy e. The internal energy subtracted by linear distribution, which corresponds to the last term in equation (3.54), will be shown.

Figure 3.8 shows the result for various relaxation parameters. The result, which is shown to be independent of ϕ, coincides exactly with the analysis. Figure 3.9, the result for various walls' temperatures, also shows complete agreement with the analysis. The relevance of the model for the variation of speed U is shown in Figure 3.10.

Finally, simulation for $e_1\neq e_2$ was conducted. The result for $e_1=0.5$ and $e_2=1.5$ is shown in Figure 3.11. The result exactly agrees with the analytical solution.

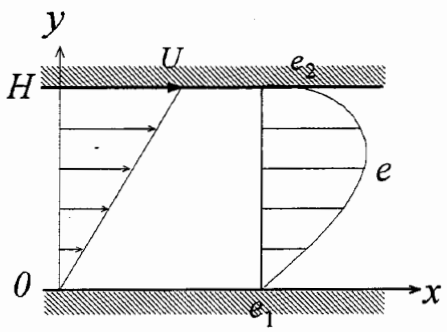

Figure 3.6. Couette flow simulation.

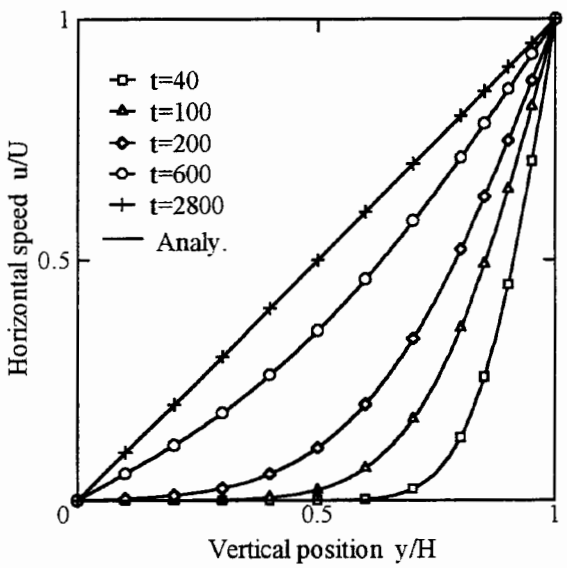

Figure 3.7. Evolution of horizontal speed distribution. e_1=e_2=1.0.

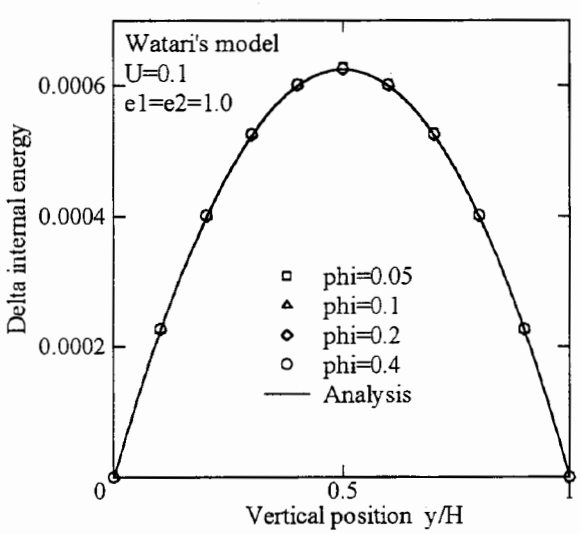

Figure 3.8. Internal energy distribution at steady state for various relaxation parameters: ϕ =0.05, 0.1, 0.2, 0.4. U=0.1, e_1=e_2=1.0. The internal energy subtracted by linear distribution is shown. The results for all ϕ overlap each other.

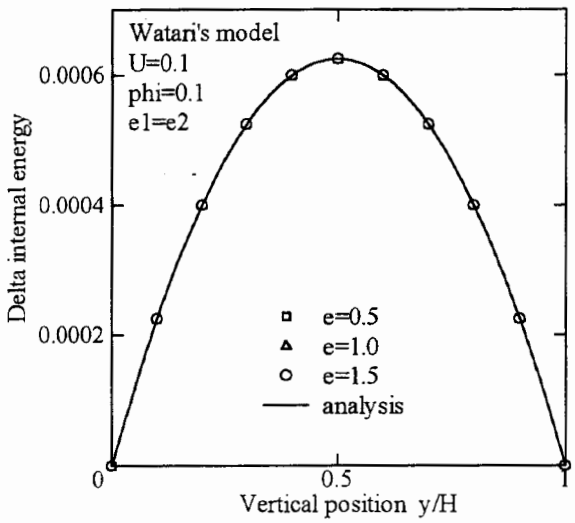

Figure 3.9. Internal energy distribution at steady state for various wall temperatures: e_1=e_2=0.5, 1.0, 1.5. U=0.1, ϕ=0.1. The internal energy subtracted by linear distribution is shown. The results for all cases overlap each other.

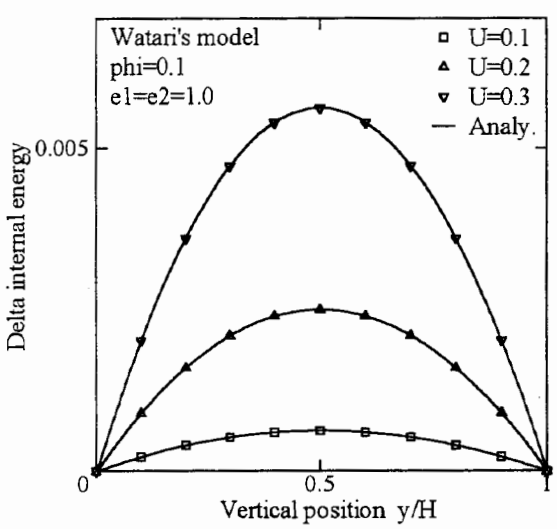

Figure 3.10. Internal energy distribution at steady state for various boundary speeds: U=0.1, 0.2, 0.3. ϕ=0.1, e_1=e_2=1.0. The internal energy subtracted by linear distribution is shown.

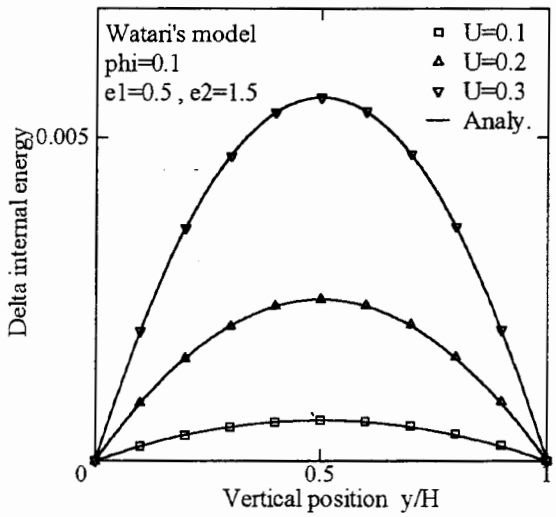

Figure 3.11. Internal energy distribution at steady state for various boundary speeds: U=0.1, 0.2, 0.3. The wall temperatures are different: e_1=0.5, e_2=1.5. ϕ=0.1. The internal energy subtracted by linear distribution is shown.

3.5. Comparison with existing thermal models

Couette simulations using existing multi-speed thermal BGK LBM models were conducted in a FDLBM scheme to compare them with the proposed model.

The model by Alexander et al [3] 2D13V (rest particle and 2 speeds of Group Ⅲ):

They retain up-to third orders of local flow speed in the local equilibrium distribution function. They use GroupⅢ velocities (hexagonal) that ensure only fourth rank tensor isotropy. As shown in the new model derivation, up-to fourth order expansion and up-to seventh rank tensor isotropy are necessary to recover correct fluid equations. Therefore, in their model, error terms are hidden in the momentum and energy diffusions. Figure 3.12 shows the result for the variation of the relaxation parameter. The result indicates the dependency on the relaxation parameter, which contradicts the analysis. The result for the variation of walls' temperature is shown in Figure 3.13. The figure shows the dependency on the internal energy, which also contradicts the analysis. Those discrepancies are the reflection of the error terms described above.

The model by Chen et al[4,7] 2D16V (2 speeds of Group I and 2 speeds of Group Ⅱ):

They say that as they retain up-to fourth orders of local flow speed and realize equivalent up-to seventh rank tensor isotropy by mixing weighted Group I and Ⅱ velocities, their model recovers correct fluid equations. However, the simulation results are different from what they say. The result for the various values of the relaxation parameter ϕ is shown in Figure 3.14. Although the model has been quite improved from Alexander's model, the model still yields an erroneous solution for the ϕ<0.2. For ϕ=0.1, the result for the variation of walls' temperature

is shown in Figure 3.15. This figure indicates that the simulation for ϕ<0.2 (low viscosity flow) yields an erroneous solution if the internal energy e diverts from 0.5. Consequently, although the result for e=0.5 in the variation of speed U (Figure 3.16) shows good agreement with analytical solution, the model gives distorted solutions if the difference in temperature between walls exceeds a certain range (Figure 3.17). Further study is necessary where these discrepancies come from.

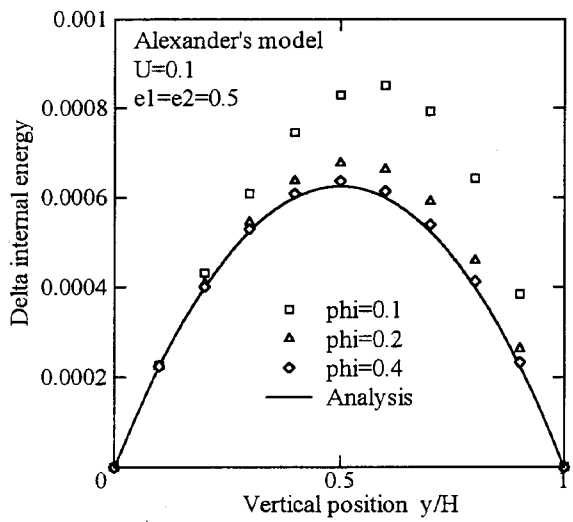

Figure 3.12. Alexander's model. Internal energy distribution at steady state for various relaxation parameters: ϕ=0.1, 0.2, 0.4. U=0.1, e_1=e_2=0.5. The internal energy subtracted by linear distribution is shown. The result shows dependence on ϕ, which contradicts the analytical prediction.

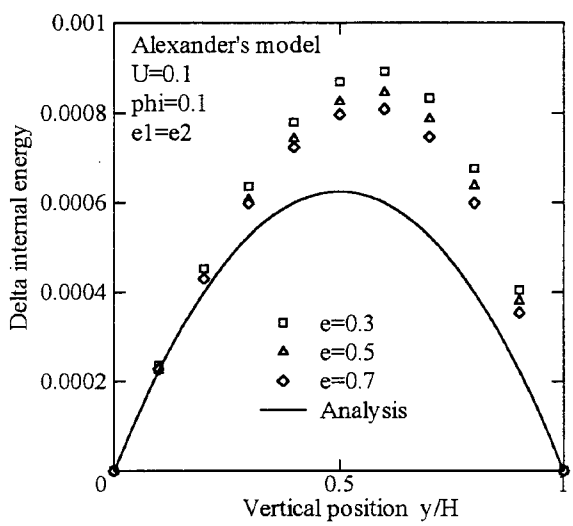

Figure 3.13. Alexander's model. Internal energy distribution at steady state for various wall temperatures: e_1=e_2=0.3, 0.5, 0.7. U=0.1, ϕ=0.1. The internal energy subtracted by linear distribution is shown. The result shows dependence on e, which contradicts the analytical prediction.

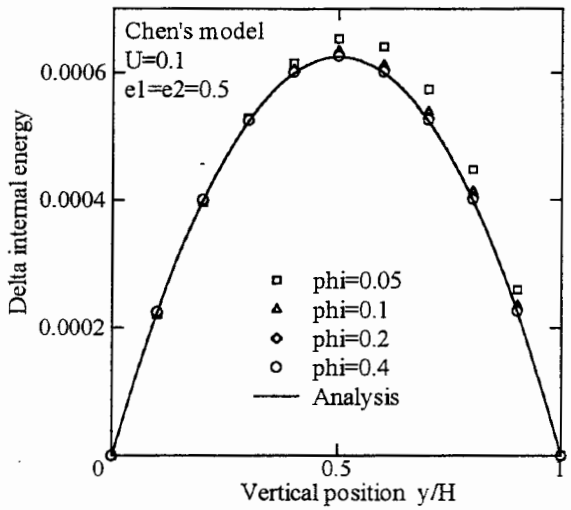

Figure 3.14. Chen's model. Internal energy distribution at steady state for various relaxation parameters: ϕ=0.05, 0.1, 0.2, 0.4. U=0.1, e_1=e_2=0.5. The internal energy subtracted by linear distribution is shown. Although the model has been improved from Alexander's model, the result still shows dependence on ϕ, which contradicts the analytical prediction.

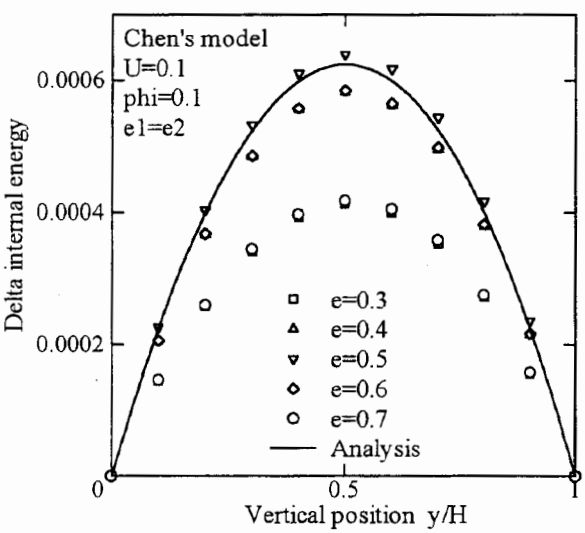

Figure 3.15. Chen's model. Internal energy distribution at steady state for various walls' temperatures: e_1=e_2=0.3, 0.4, 0.5, 0.6, 0.7. U=0.1, ϕ=0.1. The internal energy subtracted by linear distribution is shown. The results for e=0.4 and 0.6 overlap. The results for e=0.3 and 0.7 overlap. The result shows dependence on e, which contradicts the analytical prediction.

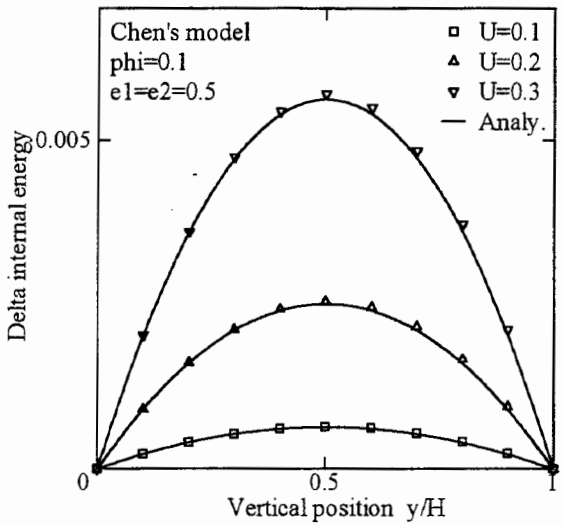

Figure 3.16. Chen's model. Internal energy distribution at steady state for various boundary speeds: U=0.1, 0.2, 0.3. ϕ=0.1, e_1=e_2=0.5. The internal energy subtracted by linear distribution is shown.

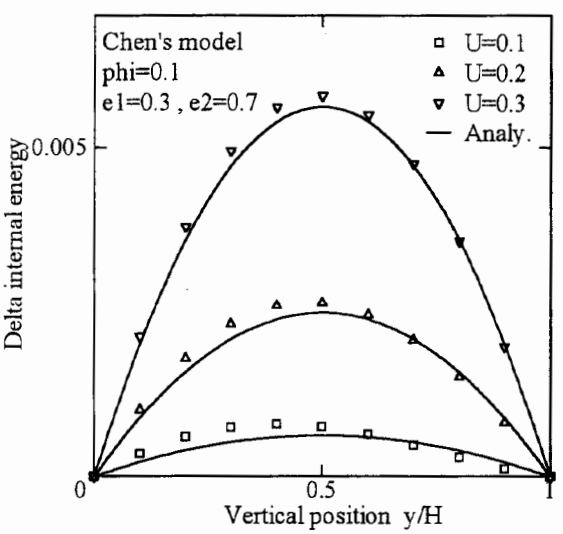

Figure 3.17. Chen's model. Internal energy distribution at steady state for various boundary speeds: U=0.1, 0.2, 0.3, when the wall temperatures are different; e_1=0.3, e_2=0.7. ϕ=0.1. The internal energy subtracted by linear distribution is shown. The model gives distorted solutions.

3.6. Conclusions

A new multi-speed thermal model for the FDLBM was proposed. To recover correct fluid equations, up-to fourth orders of local flow velocity should be retained in the local equilibrium distribution function and the particle velocities should have up-to seventh rank tensor isotropy.

In the FDLBM, we can select particle velocities independently from the lattice configuration. Therefore, particle velocities of octagonal directions, which have up-to seventh rank isotropic tensors, are adopted. Furthermore, as the local equilibrium distribution function is determined such that it retains as much Maxwellian characteristic as possible, the proposed model has excellent numerical stability in addition to strict accuracy.

The model was verified by flow simulations and was compared with the results of existing models. While existing multi-speed thermal models give correct answers in quite limited ranges of viscosity and temperature, the proposed model gives correct answers in wide ranges.

I would like to note that the proposed model has capability to high Reynolds number problems. In an application study,[8] thermal cavity flow simulations of ϕ=0.0009 was successfully conducted.

References

[1] S. Chen and G. Doolen, "Lattice Boltzmann method for fluid flows", Annu. Rev. Fluid Mech. 30: 329-64 (1998).

[2] X. Shan and H. Chen, "Lattice Boltzmann model for simulating flows with multiple phases and components", Phys. Rev. E 47: 1815-19 (1993).

[3] F. J. Alexander, S. Chen and J. Sterling, "Lattice Boltzmann thermohydrodynamics", Phys. Rev. E 47: R2249-52 (1993).

[4] Y. Chen, H. Ohashi and M. Akiyama, "Thermal lattice BGK model without nonlinear deviations in macrodynamic equations", Phys. Rev. E 50,4: 2776-83 (1994).

[5] N. Cao, S. Chen, S. Jin and D. Martinez, "Physical symmetry and lattice symmetry in the lattice Boltzmann method", Phys. Rev. E 55,1: R21-24 (1997).

[6] S. Wolfram, "Cellular automaton fluids 1: Basic Theory", J. Stat. Phys. 45: 471-526 (1986).

[7] Y. Chen, H. Ohashi and M. Akiyama, "Heat transfer in lattice BGK modeled fluid", J. Stat. Phys. 81: 71-85 (1995).

[8] M. Watari and M. Tsutahara, "Thermal Cavity Flow of Compressible Fluids. Numerical Simulation by a Newly proposed Model of Finite Difference Lattice Boltzmann Method", The Fifth JSME-KSME Fluids Engineering Conference. Nov.17-21, (2002).

4. Three-dimensional thermal model of finite difference lattice Boltzmann method with high spatial isotropy

4.1. Introduction

In the lattice Boltzmann method (LBM), there are two ways of handling thermal fluids. One is the so-called "multi-component thermal model."[1] The other is the so-called "multi-speed thermal model," [2,3] where particle velocities that have different speeds are used. While the multi-speed thermal model is intended to correctly represent heat characteristics and compressibility, it has been shown that a three-dimensional LBM BGK multi-speed thermal model is theoretically impossible. [4]

The finite difference lattice Boltzmann method (FDLBM) [5] was proposed in order to secure numerical stability and to apply non-uniform grids. In the LBM, the particle velocities are restricted to those that exactly link the lattice nodes in unit time. On the other hand, in the FDLBM, as that constraint does not need to be considered, particle velocities can be selected independently from the lattice configuration. Therefore, a correct and numerically stable multi-speed thermal model can be constructed by adopting more isotropic particle velocities. This paper proposes a three-dimensional FDLBM BGK (single relaxation) thermal model based on the above concept.

4.2. Finite difference lattice Boltzmann method

Below is a general description of the three-dimensional thermal FDLBM model. The evolution of the distribution function f_{ki} for particle velocity c_{ki} is governed by the following equation, which is solved using Euler and the second upwind difference scheme:

$$\frac{\partial f_{ki}}{\partial t} + c_{ki\alpha}\frac{\partial f_{ki}}{\partial r_\alpha} = -\frac{1}{\phi}(f_{ki} - f_{ki}^{(0)}) \tag{4.1}$$

where the subscript k indicates a group of particle velocities whose speed c_k and i indicates the particle's direction. The subscript α indicates x, y, or z component. The variable t is time, r_α the spatial coordinate, $f_{ki}^{(0)}$ the local equilibrium distribution function and ϕ the relaxation parameter. Macroscopic quantities: the density ρ, the velocity u_α, and the internal energy e, are defined as follows:

$$\rho = \sum_{ki} f_{ki} \tag{4.2}$$

$$\rho u_\alpha = \sum_{ki} f_{ki} c_{ki\alpha} \tag{4.3}$$

$$\rho(e + \frac{u^2}{2}) = \sum_{ki} f_{ki}\frac{c_k^2}{2} \tag{4.4}$$

The local equilibrium distribution function is determined to satisfy the following moment summation equations:

$$\sum_{ki} f_{ki}^{(0)} = \rho \tag{4.5}$$

$$\sum_{ki} f_{ki}^{(0)} c_{ki\alpha} = \rho u_\alpha \tag{4.6}$$

$$\sum_{ki} f_{ki}^{(0)} c_{ki\alpha} c_{ki\beta} = \rho(\frac{2}{3} e\delta_{\alpha\beta} + u_\alpha u_\beta) \tag{4.7}$$

$$\sum_{ki} f_{ki}^{(0)} c_{ki\alpha} c_{ki\beta} c_{ki\gamma} = \rho[\frac{2}{3} e(u_\alpha \delta_{\beta\gamma} + u_\beta \delta_{\gamma\alpha} + u_\gamma \delta_{\alpha\beta}) + u_\alpha u_\beta u_\gamma] \tag{4.8}$$

$$\sum_{ki} f_{ki}^{(0)} \frac{c_k^2}{2} = \rho(e + \frac{u^2}{2}) \tag{4.9}$$

$$\sum_{ki} f_{ki}^{(0)} \frac{c_k^2}{2} c_{ki\alpha} = \rho u_\alpha (\frac{5}{3} e + \frac{u^2}{2}) \tag{4.10}$$

$$\sum_{ki} f_{ki}^{(0)} \frac{c_k^2}{2} c_{ki\alpha} c_{ki\beta} = \rho[e(\frac{10}{9} e + \frac{u^2}{3})\delta_{\alpha\beta} + u_\alpha u_\beta (\frac{7}{3} e + \frac{u^2}{2})] \tag{4.11}$$

Applying the Chapman-Enskog expansion, the above formulation is shown equivalent to the following fluid equations (Navier-Stokes equations):

$$\frac{\partial \rho}{\partial t} + \frac{\partial}{\partial r_\alpha}(\rho u_\alpha) = 0 \tag{4.12}$$

$$\frac{\partial}{\partial t}(\rho u_\alpha) + \frac{\partial}{\partial r_\beta}(\rho u_\alpha u_\beta + P\delta_{\alpha\beta}) - \frac{\partial}{\partial r_\beta}[\mu(\frac{\partial u_\beta}{\partial r_\alpha} + \frac{\partial u_\alpha}{\partial r_\beta} - \frac{2}{3}\frac{\partial u_\gamma}{\partial r_\gamma}\delta_{\alpha\beta})] = 0 \tag{4.13}$$

$$\frac{\partial}{\partial t}[\rho(e + \frac{u^2}{2})] + \frac{\partial}{\partial r_\alpha}[\rho u_\alpha (e + \frac{u^2}{2} + \frac{P}{\rho})] - \frac{\partial}{\partial r_\alpha}[\kappa' \frac{\partial e}{\partial r_\alpha} + \mu u_\beta (\frac{\partial u_\beta}{\partial r_\alpha} + \frac{\partial u_\alpha}{\partial r_\beta} - \frac{2}{3}\frac{\partial u_\gamma}{\partial r_\gamma}\delta_{\alpha\beta})] = 0 \tag{4.14}$$

where the pressure P, the viscosity coefficient μ, and the heat conductivity κ' have the following relations:

$$P = \frac{2}{3}\rho e \tag{4.15}$$

$$\mu = \frac{2}{3}\rho e \phi \tag{4.16}$$

$$\kappa' = \frac{10}{9}\rho e \phi \tag{4.17}$$

Temperature T is related to the internal energy by the following equation (R: gas constant):

$$T = \frac{2e}{3R} \tag{4.18}$$

4.3. New FDLBM model derivation

The energy diffusion equation (4.11) contains up-to fourth order of flow velocity u. Therefore, up-to fourth order terms of flow velocity are retained in the local equilibrium distribution function $f_{ki}^{(0)}$. Assuming the velocity u is small, the Maxwellian distribution is expanded:

$$\begin{aligned} f_{ki}^{(0)} &= \frac{\rho}{(4/3\,\pi e)^{3/2}}\exp\left(-\frac{3}{4e}(c_{ki\alpha}-u_\alpha)^2\right) \\ &= \rho\frac{1}{(4/3\,\pi e)^{3/2}}\exp\left(-\frac{3}{4e}c_k^2\right)\exp\left(-\frac{3}{2e}(c_{ki\alpha}u_\alpha-u^2)\right) \end{aligned} \tag{4.19}$$

The local equilibrium distribution function for the FDLBM is obtained:

$$\begin{aligned} f_{ki}^{(0)} = \rho F_k[&(1-\frac{3u^2}{4e}+\frac{9u^4}{32e^2})+\frac{3}{2e}(1-\frac{3u^2}{4e})c_{ki\xi}u_\xi+\frac{9}{8e^2}(1-\frac{3u^2}{4e})c_{ki\xi}c_{ki\eta}u_\xi u_\eta \\ &+\frac{9}{16e^3}c_{ki\xi}c_{ki\eta}c_{ki\zeta}u_\xi u_\eta u_\zeta+\frac{27}{128e^4}c_{ki\xi}c_{ki\eta}c_{ki\zeta}c_{ki\chi}u_\xi u_\eta u_\zeta u_\chi] \end{aligned} \tag{4.20}$$

where the parameter F_k represents the term $\frac{1}{(4/3\,\pi e)^{3/2}}\exp\left(-\frac{3}{4e}c_k^2\right)$ and is the function of e and c_k. The local equilibrium distribution function $f_{ki}^{(0)}$ contains the fourth rank tensor and the momentum diffusion equation (4.8) contains the third rank tensor. As a result, up-to seventh rank tensor must be isotropic to recover correct fluid equations.

The nth rank tensor for the group of m particle velocities is defined as:

$$E_{\alpha_1\alpha_2\alpha_3\cdots\alpha_n}^{(n)} = \sum_{i=1}^{m} c_{i\alpha_1}c_{i\alpha_2}c_{i\alpha_3}\cdots c_{i\alpha_n} \tag{4.21}$$

where $\alpha_1,..,\alpha_n$ indicate any of x, y, and z components. The tensor is isotropic if it is invariant for the coordinate rotation and reflection. As for being isotropic, the odd rank tensors should vanish.

$$E_{\alpha_1\alpha_2\alpha_3\cdots\alpha_{2n+1}}^{(2n+1)} = 0 \tag{4.22}$$

The isotropic even rank tensors should be sums of all possible product of Kronecker delta.[6]

$$\begin{aligned} &E_{\alpha_1\alpha_2\alpha_3\cdots\alpha_{2n}}^{(2n)} = \frac{m}{3\cdot5\cdots(3+2n-2)}c^{2n}\Delta_{\alpha_1\alpha_2\alpha_3\cdots\alpha_{2n}}^{(2n)} \\ &\Delta_{\alpha\beta}^{(2)} = \delta_{\alpha\beta} \\ &\Delta_{\alpha\beta\gamma\chi}^{(4)} = \delta_{\alpha\beta}\delta_{\gamma\chi}+\delta_{\alpha\gamma}\delta_{\beta\chi}+\delta_{\alpha\chi}\delta_{\beta\gamma} \\ &\Delta_{\alpha\beta\gamma\chi\lambda\tau}^{(6)} = \delta_{\alpha\beta}\Delta_{\gamma\chi\lambda\tau}^{(4)}+\delta_{\alpha\gamma}\Delta_{\beta\chi\lambda\tau}^{(4)}+\delta_{\alpha\chi}\Delta_{\beta\gamma\lambda\tau}^{(4)}+\delta_{\alpha\lambda}\Delta_{\beta\gamma\chi\tau}^{(4)}+\delta_{\alpha\tau}\Delta_{\beta\gamma\chi\lambda}^{(4)} \end{aligned} \tag{4.23}$$

This paper's strategy for constructing the model is, first, to create a basic group of particle velocities that has isotropic tensors up-to seventh rank. Then, the model is constructed using several speeds of these groups in addition to a rest particle.

Vectors that point to the vertexes of dodecahedron and icosahedron (Figure 4.1) from the center have high isotropy. The components and tensors for these vectors are summarized in Table 4.1.

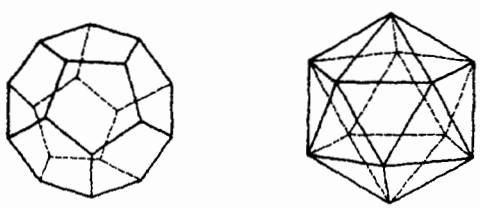

(a) Dodecahedron (b) Icosahedron

Figure 4.1. Dodecahedron and icosahedron.

Table 4.1. Tensors for vectors pointing from the center to the vertexes of dodecahedron and icosahedron. The m is the number of vectors. $E^{(n)}$ is the nth rank tensor. The *cyc* indicates cyclic permutations. The symbol ○ indicates isotropic, and the symbol X anisotropic.

group	components of vectors	m	$E^{(1)}$	$E^{(2)}$	$E^{(3)}$	$E^{(4)}$	$E^{(5)}$	$E^{(6)}$	$E^{(7)}$
Dodecahedron	$\lambda(\pm1,\pm1,\pm1), cyc:\lambda(0,\pm\phi^{-1},\pm\phi)$	20	○	○	○	○	○	X	○
Icosahedron	$cyc:\tau(0,\pm\phi,\pm1)$	12	○	○	○	○	○	X	○

$\phi=(1+\sqrt{5})/2 \qquad \lambda=1/\sqrt{3} \qquad \tau=\sqrt{2}/\sqrt{5+\sqrt{5}}$

Table 4.2. Sixth rank tensors for vectors of dodecahedron, icosahedron in Table 4.1, and for the combined vectors. The values in the parenthesis are those for isotropic tensors calculated by the equation (4.23).

6th rank tensor	Dodecahedron	Icosahedron	Dodecahedron + Icosahedron
$\sum_{i=1}^{m} c_{ix}c_{ix}c_{ix}c_{ix}c_{ix}c_{ix}$	2.9630 (2.8571)	1.6000 (1.7143)	4.5630 (4.5714)
$\sum_{i=1}^{m} c_{ix}c_{ix}c_{ix}c_{ix}c_{iy}c_{iy}$	0.3529 (0.5714)	0.5789 (0.3429)	0.9318 (0.9143)
$\sum_{i=1}^{m} c_{ix}c_{ix}c_{iy}c_{iy}c_{iz}c_{iz}$	0.6842 (0.5714)	0.2211 (0.3429)	0.9053 (0.9143)

The odd tensors for spatially uniformly distributed vectors are shown to vanish. For even tensors, both groups have isotropic tensors up-to fourth rank, however, they yield anisotropic tensors for the sixth rank and higher. How anisotropic are they? The sixth rank tensors for typical combinations are shown in Table 4.2. In the table, the values in the parenthesis are those for isotropic tensors calculated by the equation (4.23). The tensors of dodecahedron and icosahedron have more than ten percent discrepancies from the isotropic tensors. However, if both vectors are combined as a group, the sixth rank tensor becomes almost isotropic with about one or two percent errors. Therefore, these thirty-two vectors are adopted as a basic group of particle velocities.

When the property that the odd tensors vanish is applied to equations (4.5) through (4.11), the following equations are obtained to determine the parameters F_k:

$$\sum_{ki} F_k = 1 \tag{4.24}$$

$$\sum_{ki} F_k c_{ki\alpha} c_{ki\beta} = \frac{2}{3} e \delta_{\alpha\beta} \tag{4.25}$$

$$\sum_{ki} F_k c_{ki\alpha} c_{ki\beta} c_{ki\gamma} c_{ki\chi} = \frac{4}{9} e^2 \Delta^{(4)}_{\alpha\beta\gamma\chi} \tag{4.26}$$

$$\sum_{ki} F_k c_{ki\alpha} c_{ki\beta} c_{ki\gamma} c_{ki\chi} c_{ki\lambda} c_{ki\tau} = \frac{8}{27} e^3 \Delta^{(6)}_{\alpha\beta\gamma\chi\lambda\tau} \tag{4.27}$$

$$\sum_{ki} F_k \frac{c_k^2}{2} = e \tag{4.28}$$

$$\sum_{ki} F_k \frac{c_k^2}{2} c_{ki\alpha} c_{ki\beta} = \frac{10}{9} e^2 \delta_{\alpha\beta} \tag{4.29}$$

$$\sum_{ki} F_k \frac{c_k^2}{2} c_{ki\alpha} c_{ki\beta} c_{ki\gamma} c_{ki\chi} = \frac{28}{27} e^3 \Delta^{(4)}_{\alpha\beta\gamma\chi} \tag{4.30}$$

$$\sum_{ki} F_k \frac{c_k^2}{2} c_{ki\alpha} c_{ki\beta} c_{ki\gamma} c_{ki\chi} c_{ki\lambda} c_{ki\tau} = \frac{8}{9} e^4 \Delta^{(6)}_{\alpha\beta\gamma\chi\lambda\tau} \tag{4.31}$$

If it is further assumed that particle velocities have isotropic tensors up-to seventh rank, the eight equations above reduce to the following five equations:

From equation (4.24),

$$\sum_{ki} F_k = 1 \tag{4.32}$$

From equations (4.25), (4.28),

$$\sum_{ki} F_k c_k^2 = e/16 \tag{4.33}$$

From equations (4.26), (4.29),

$$\sum_{ki} F_k c_k^4 = \frac{5}{24} e^2 \tag{4.34}$$

From equations (4.27), (4.30),

$$\sum_{ki} F_k c_k^6 = \frac{35}{36} e^3 \tag{4.35}$$

From equation (4.31),

$$\sum_{ki} F_k c_k^8 = \frac{35}{6} e^4 \tag{4.36}$$

Five speed groups of particle velocities are necessary to satisfy the above equations. A rest particle (c_0=0.0) and four moving groups of particles whose speeds are c_1, c_2, c_3, and c_4 ($0<c_1<c_2<c_3<c_4$) are assumed. The equations (4.32) through (4.36) are easily solved to give the following. The parameters F_k are functions of c_1, c_2, c_3, c_4, and internal energy e.

$$F_1 = \frac{1}{c_1^2(c_1^2-c_2^2)(c_1^2-c_3^2)(c_1^2-c_4^2)}\left[\frac{35}{6}e^4 - \frac{35}{36}(c_2^2+c_3^2+c_4^2)e^3 + \frac{5}{24}(c_2^2c_3^2+c_3^2c_4^2+c_4^2c_2^2)e^2 - \frac{c_2^2c_3^2c_4^2}{16}e\right] \tag{4.37}$$

$$F_2 = \frac{1}{c_2^2(c_2^2-c_3^2)(c_2^2-c_4^2)(c_2^2-c_1^2)}\left[\frac{35}{6}e^4 - \frac{35}{36}(c_3^2+c_4^2+c_1^2)e^3 + \frac{5}{24}(c_3^2c_4^2+c_4^2c_1^2+c_1^2c_3^2)e^2 - \frac{c_3^2c_4^2c_1^2}{16}e\right] \tag{4.38}$$

$$F_3 = \frac{1}{c_3^2(c_3^2-c_4^2)(c_3^2-c_1^2)(c_3^2-c_2^2)}\left[\frac{35}{6}e^4 - \frac{35}{36}(c_4^2+c_1^2+c_2^2)e^3 + \frac{5}{24}(c_4^2c_1^2+c_1^2c_2^2+c_2^2c_4^2)e^2 - \frac{c_4^2c_1^2c_2^2}{16}e\right] \tag{4.39}$$

$$F_4 = \frac{1}{c_4^2(c_4^2-c_1^2)(c_4^2-c_2^2)(c_4^2-c_3^2)}\left[\frac{35}{6}e^4 - \frac{35}{36}(c_1^2+c_2^2+c_3^2)e^3 + \frac{5}{24}(c_1^2c_2^2+c_2^2c_3^2+c_3^2c_1^2)e^2 - \frac{c_1^2c_2^2c_3^2}{16}e\right] \tag{4.40}$$

$$F_0 = 1 - 32(F_1 + F_2 + F_3 + F_4) \tag{4.41}$$

As far as the model being stably simulated, the combination of the values: c_1, c_2, c_3, and c_4, does not affect the accuracy itself. It governs the range of temperature where simulation is stably conducted. Several criteria were tried and it was finally concluded that following hypothesis has the closest relationship with simulation stability: "The model is stable as far as $F_0>F_1>F_2>F_3>F_4>0$."

Therefore, the following optimum problem was solved:

Under the condition	$0 < c_1 < c_2 < c_3 < c_4$	
determine	c_1, c_2, c_3, and c_4	
which maximizes	$(e_H-e_L)/e_M$	(4.42)
for $e_L < e < e_H$	$F_0/F_1>1.1$ and $F_1/F_2>1.1$ and	
	$F_2/F_3>1.1$ and $F_3/F_4>1.1$ and $F_4>0$. holds	
keeping	$e_M=(e_H+e_L)/2=1.0$	

The result is the following. The model is expected to stably simulate the flow for the temperature range: e = 0.48~1.52.

$$(c_0, c_1, c_2, c_3, c_4) = (0.0, 1.01, 1.82, 2.67, 3.88) \tag{4.43}$$

$$e_L = 0.48,\ e_H = 1.52,\quad (e_H - e_L)/e_M = 1.04 \tag{4.44}$$

4.4. Verification of the new model

The validity of the model was confirmed by conducting two simulations. First, the speed of sound was measured. Second, the shear flow between parallel walls (Couette flow) was investigated.

4.4.1. Speed of sound

In a box, a plate divides fluids that have small difference in density (Figure 4.2). When the plate is removed, sound waves (expansion and compression) propagate. The position of the pressure jump (Figure 4.3) was measured to calculate the speed of sound. The results at various internal energy levels are shown in Figure 4.4. The simulation was stably conducted for the range: e=0.5~1.5. The measured sound speed agreed exactly with the following theoretical value:

$$c_s = \sqrt{10/9\, e} \tag{4.45}$$

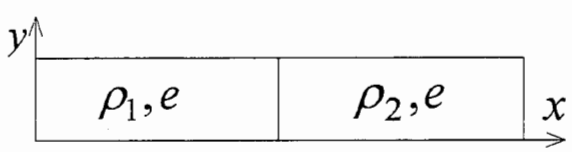

Figure 4.2. Sound wave simulation.

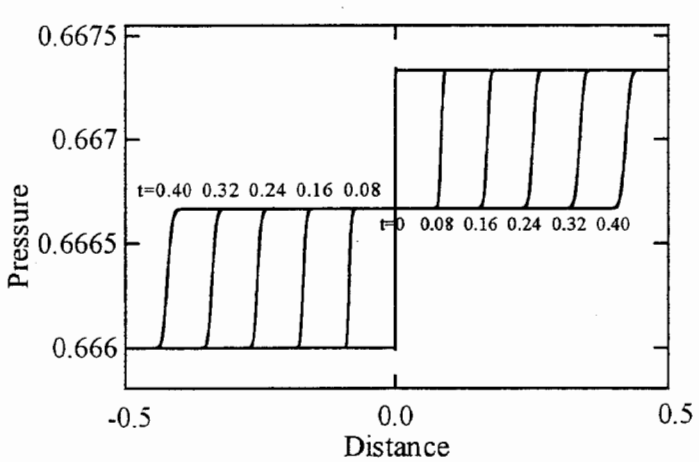

Figure 4.3. Propagation of sound waves.
The pressure jumps advance as time proceeds.

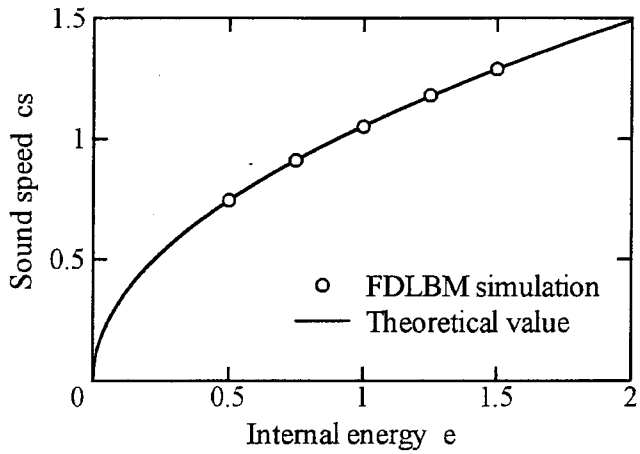

Figure 4.4. Sound speed versus internal energy.

The results are compared with the theoretical value, $c_s = \sqrt{10/9\, e}$.

4.4.2. Couette flow

The upper wall, which is H apart from the lower wall and has internal energy e_2, starts to move at speed U. The lower wall has e_1 and is at rest (Figure 4.5). The horizontal speed distribution at various instants for e_1=e_2 is shown in Figure 4.6. The simulation result agreed exactly with the theoretical value of equation (4.46).

$$\frac{u}{U} = \frac{y}{H} - \frac{2}{\pi}\sum_{n=1}^{\infty} \exp\left[-n^2\pi^2 \frac{\mu t}{\rho H^2}\right] \sin\left[n\pi(1-\frac{y}{H})\right] \tag{4.46}$$

The analytical distribution of internal energy in a steady state is:

$$e = e_1 + (e_2 - e_1)\frac{y}{H} + \frac{\mu}{2\kappa'}U^2 \frac{y}{H}(1-\frac{y}{H}) \tag{4.47}$$

Since the coefficients μ and κ' are given as (4.16) and (4.17), respectively, value $\mu/2\kappa'$ is constant (=0.3). Therefore, the internal energy subtracted by linear distribution, which corresponds to the last term in equation (4.47), does not depend on relaxation parameter ϕ or on walls' temperatures.

Figure 4.7 shows the result for various relaxation parameters. The result, which is shown to be independent of ϕ, coincides exactly with the analysis. Figure 4.8, the result for various walls' temperatures, also shows complete agreement with the analysis.

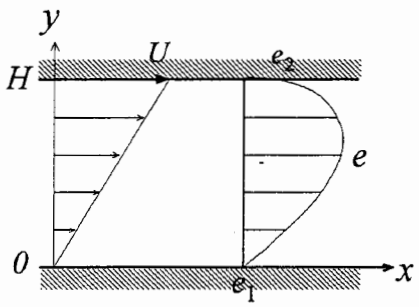

Figure 4.5. Couette flow simulation.

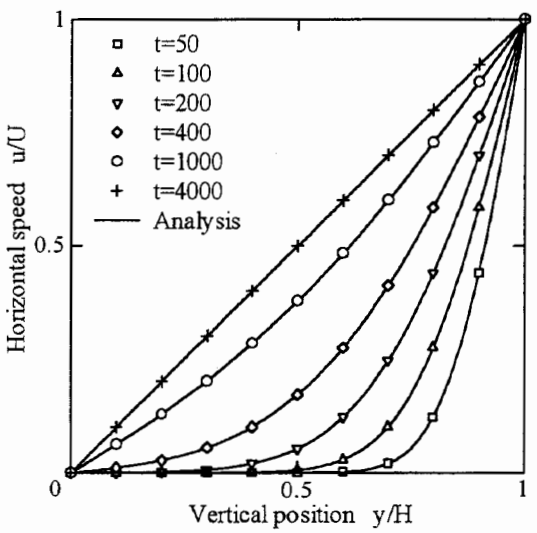

Figure 4.6. Evolution of horizontal speed distribution.

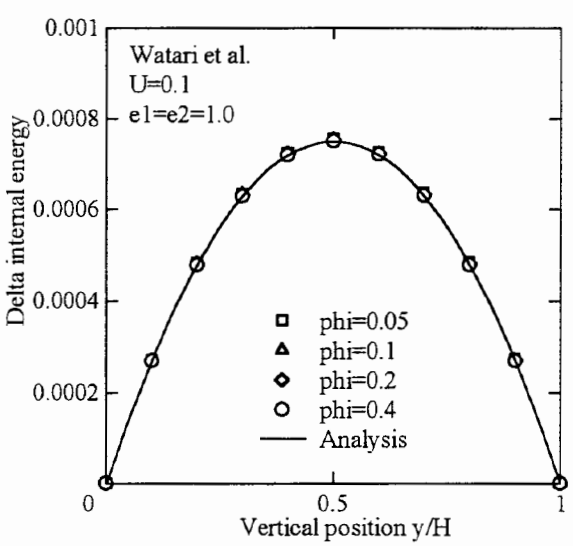

Figure 4.7. Internal energy distribution in a steady state for various relaxation parameters: ϕ=0.05, 0.1,0.2,0.4. U=0.1, e_1=e_2=1.0. The internal energy subtracted by linear distribution is shown. The results for all cases overlap each other.

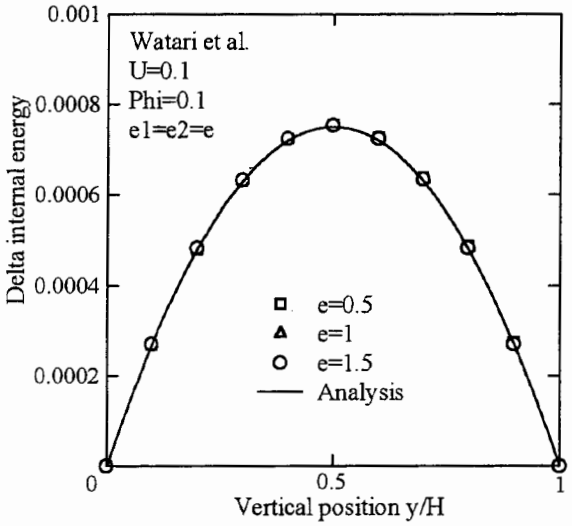

Figure 4.8. Internal energy distribution in a steady state for various wall temperatures: e_1=e_2=0.5, 1.0, 1.5. U=0.1, ϕ=0.1. The internal energy subtracted by linear distribution is shown. The results for all cases overlap each other.

4.5. Evaluation of existing thermal models

Existing three-dimensional multi-speed thermal LBM models were evaluated by applying them to a Couette simulation, using a FDLBM scheme.

As predicted in the previous study,[4] although the model by Chen et al.[2] (3D40V) gave a linear profile to the horizontal speed distribution in a steady state, internal energy showed strange distribution (internal energy in the fluid is lower than that at the walls!).

The model by Takada et al.[3] (3D39V) retains up-to third order terms of flow velocity in the local equilibrium distribution function $f_{ki}^{(0)}$ and ensures only up-to fifth rank tensor isotropy. The model adopts as particle velocities, a rest particle and 5 groups of moving particles shown in Figure 4.9. As expected from insufficient terms in the local equilibrium distribution function and insufficient isotropy, although the horizontal speed profile showed an appropriate evolution, the internal energy distribution in a steady state yielded discrepancies with the analytical prediction, as shown in Figure 4.10 and Figure 4.11.

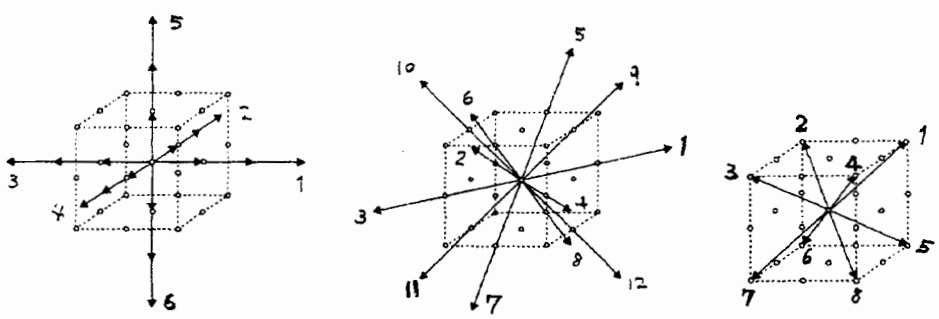

Figure 4.9. Particle velocities of the model by Takada et al. They are three speeds of six directions: c_k=1,2,3, one speed of twelve directions: c_k=$2\sqrt{2}$, and one speed of eight directions: c_k=$\sqrt{3}$.

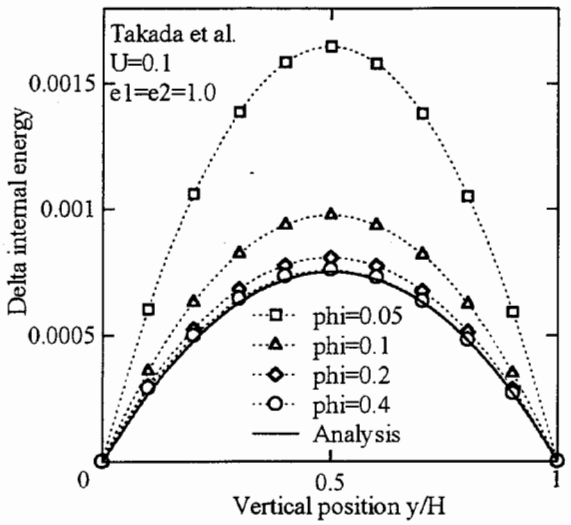

Figure 4.10. Internal energy distribution in a steady state for various relaxation parameters: ϕ=0.05, 0.1, 0.2, 0.4. U=0.1, e_1=e_2=1.0. The internal energy subtracted by linear distribution is shown. The result shows dependence on ϕ, which contradicts the analytical prediction.

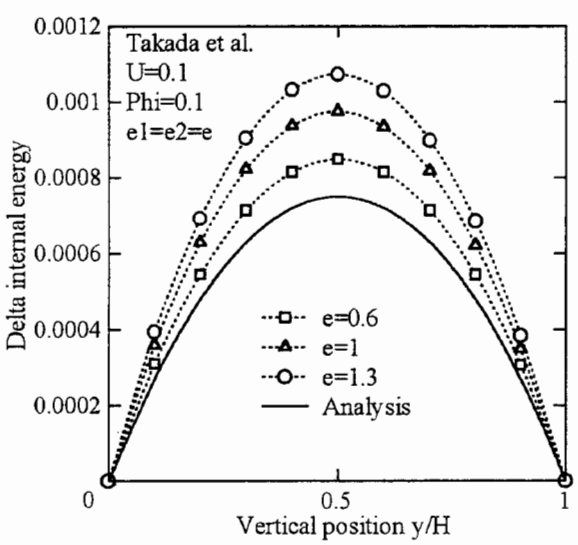

Figure 4.11. Internal energy distribution in a steady state for various wall temperatures: e_1=e_2=0.6, 1.0, 1.3. U=0.1, ϕ=0.1. The internal energy subtracted by linear distribution is shown. The result shows dependence on e, which contradicts the analytical prediction.

4.6. Conclusions

Existing three-dimensional LBM multi-speed thermal models do not provide a correct solution.

In order to recover correct fluid equations, up-to fourth orders of local flow velocity should be retained in the local equilibrium distribution function and particle velocities must have up-to seventh rank tensor isotropy. In the FDLBM, particle velocities can be selected independently from the lattice configuration. Therefore, a group of particle velocities that has high rank isotropic tensors can be adopted.

A new three-dimensional multi-speed thermal model for the FDLBM was proposed. In the model, a group of thirty-two particle velocities is selected as a basic group of moving particles. These moving particles are derived from vectors that point to the vertexes of dodecahedron and icosahedron from the center. As they have quasi-isotropic sixth rank tensor, the model made up of a rest particle and four speeds of the basic groups showed good agreement with the analytical solutions when applied to two flow simulations.

References

[1] X. Shan and H. Chen, "Lattice Boltzmann model for simulating flows with multiple phases and components", Phys. Rev. E 47: 1815-19 (1993).

[2] Y. Chen, H. Ohashi and M. Akiyama, "Thermal lattice BGK model without nonlinear deviations in macrodynamic equations", Phys. Rev. E 50,4: 2776-83 (1994).

[3] N. Takada, Y. Yamakoshi and M. Tsutahara, "Numerical Analysis of fluid motions by three-dimensional thermal lattice Boltzmann model", JSME B 64, 628: 4-11 (1998) (in Japanese).

[4] M. Watari and M. Tsutahara, "Is it possible to construct a multi-speed thermal model of the lattice Boltzmann method?" (submitted to J. Stat. Phys).

[5] N. Cao, S. Chen, S. Jin and D. Martinez, "Physical symmetry and lattice symmetry in the lattice Boltzmann method", Phys. Rev. E 55, 1: R21-24 (1997).

[6] S. Wolfram, "Cellular automaton fluids 1: Basic Theory", J. Stat. Phys. 45: 471-526 (1986).

5. Boundary conditions for thermal models of finite difference lattice Boltzmann method

5.1. Introduction

A lot of studies[1-7] have been done to make clear boundary conditions for the lattice Boltzmann method (LBM). Most of them are about boundary conditions for non-thermal models that have limited number of particle velocities. Few studies describe a clear receipt of boundary conditions for thermal models of the finite difference lattice Boltzmann method (FDLBM), that have multi-speed particle velocities. Furthermore, many of the previous work were about boundary conditions for planar wall. It seems difficult to handle conditions for corners.[1] We challenged to these themes.

In order to realize accurate boundary conditions, it is necessary not only to realize boundary conditions explicitly stated, such as velocities and temperatures, but also to assure the conditions that are not explicitly indicated, such as continuity of stress tensor. To accomplish these requirements, there seem to be two ways. One is to assume the boundary as part of fluid and to apply evolution equation there. We shall call this method "the control node method." The other, which shall be called "extrapolation method," is to define the distribution functions on the boundary by inverse mapping or extrapolation from quantities in the fluid domain.

This paper present these two methods and compare their performances, applying benchmark tests.

5.2. Thermal FDLBM model

We show here a two-dimensional thermal model of FDLBM that was used in this study. The evolution of the distribution function f_{ki} for particle velocity c_{ki} is governed by the following equation. The particle velocities are shown in Figure 5.1.

$$\frac{\partial f_{ki}}{\partial t} + c_{ki\alpha}\frac{\partial f_{ki}}{\partial r_\alpha} - g_\alpha E_{ki\alpha} = -\frac{1}{\phi}(f_{ki} - f_{ki}^{(0)}) \tag{5.1}$$

where t is time, r_α the spatial coordinate (x , y), g_α the gravity acceleration vector (0, -g), and ϕ the relaxation parameter. Macroscopic quantities: the density ρ, the velocity u_α, and the internal energy e, are defined as follows.

$$\rho = \sum_{ki} f_{ki} \tag{5.2}$$

$$\rho u_\alpha = \sum_{ki} f_{ki} c_{ki\alpha} \tag{5.3}$$

$$\rho\left(e + \frac{u^2}{2}\right) = \sum_{ki} f_{ki}\frac{c_{ki}^2}{2} \tag{5.4}$$

The local equilibrium distribution function $f_{ki}^{(0)}$ is defined as

$$f_{ki}^{(0)} = \rho F_k \varphi_{ki}^{(0)} \tag{5.5}$$

where

$$\varphi_{ki}^{(0)} = 1 + \frac{(c_{ki\alpha} u_\alpha)}{e} - \frac{u^2}{2e} + \frac{(c_{ki\alpha} u_\alpha)^2}{2e^2} - \frac{(c_{ki\alpha} u_\alpha) u^2}{2e^2} + \frac{(c_{ki\alpha} u_\alpha)^3}{6e^3} \tag{5.6}$$

$$F_0 = 1 - \frac{1}{144}(255e^3 - 525e^2 + 392e) \tag{5.7}$$

$$F_1 = \frac{1}{240}(195e^3 - 355e^2 + 180e) \tag{5.8}$$

$$F_2 = -\frac{1}{480}(75e^3 - 125e^2 + 36e) \tag{5.9}$$

$$F_3 = \frac{1}{720}(15e^3 - 15e^2 + 4e) \tag{5.10}$$

$$F_4 = -\frac{1}{12}(3e^3 - 4e^2) \tag{5.11}$$

$$F_5 = \frac{1}{192}(3e^3 - e^2) \tag{5.12}$$

The external force distribution function $E_{ki\alpha}$ is defined as

$$E_{ki\alpha} = -\frac{c_{ki\alpha}}{e} \rho F_k \varphi_{ki}^{(0)} + \rho F_k \frac{\partial \varphi_{ki}^{(0)}}{\partial c_{ki\alpha}} \tag{5.13}$$

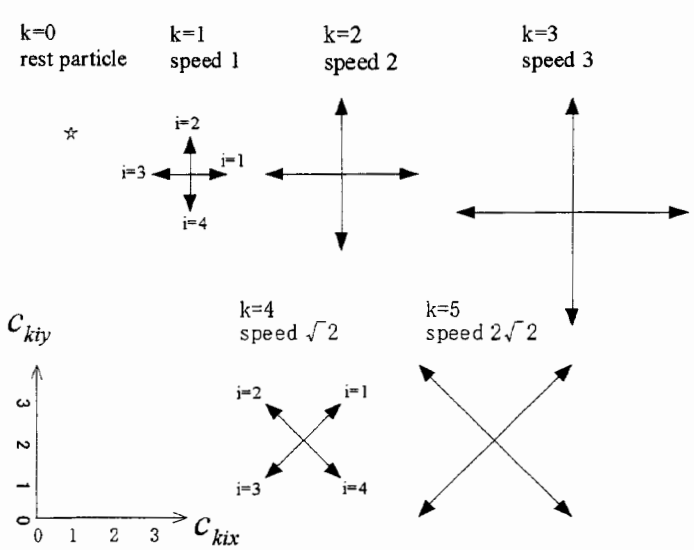

Figure 5.1. Particle velocities.

By applying the Chapman-Enskog expansion, the Navier-Stokes equations can be recovered with the error of $o\ (u^4)$

$$\frac{\partial \rho}{\partial t} + \frac{\partial}{\partial r_\alpha}(\rho u_\alpha) = 0 \tag{5.14}$$

$$\frac{\partial}{\partial t}(\rho u_\alpha) + \frac{\partial}{\partial r_\beta}(\rho u_\alpha u_\beta + P\delta_{\alpha\beta}) - \frac{\partial}{\partial r_\beta}[\mu(\frac{\partial u_\beta}{\partial r_\alpha} + \frac{\partial u_\alpha}{\partial r_\beta}) + \lambda \frac{\partial u_\gamma}{\partial r_\gamma}] + \rho g_\alpha = 0 \tag{5.15}$$

$$\frac{\partial}{\partial t}[\rho(e + \frac{u^2}{2})] + \frac{\partial}{\partial r_\alpha}[\rho u_\alpha (e + \frac{u^2}{2} + \frac{P}{\rho})] - \frac{\partial}{\partial r_\alpha}[\kappa' \frac{\partial e}{\partial r_\alpha} + \mu u_\beta (\frac{\partial u_\beta}{\partial r_\alpha} + \frac{\partial u_\alpha}{\partial r_\beta}) + \lambda u_\alpha \frac{\partial u_\gamma}{\partial r_\gamma}] + \rho g_\alpha u_\alpha = 0 \tag{5.16}$$

where the pressure P, the viscosity μ, the second viscosity λ, and the heat conductivity κ' are defined as follows.

$$\begin{aligned} P &= \rho e \\ \mu &= \rho e \phi \\ \lambda &= -\rho e \phi \\ \kappa' &= 2\rho e \phi \end{aligned} \tag{5.17 abcd}$$

5.3. Control node method

We apply the evolution equation to boundary nodes assuming that they are part of fluid. Outside the boundary, fictitious nodes, called "control nodes" are arranged. Assuming second order upwind difference scheme, two layers are necessary, as shown in Figure 5.2.

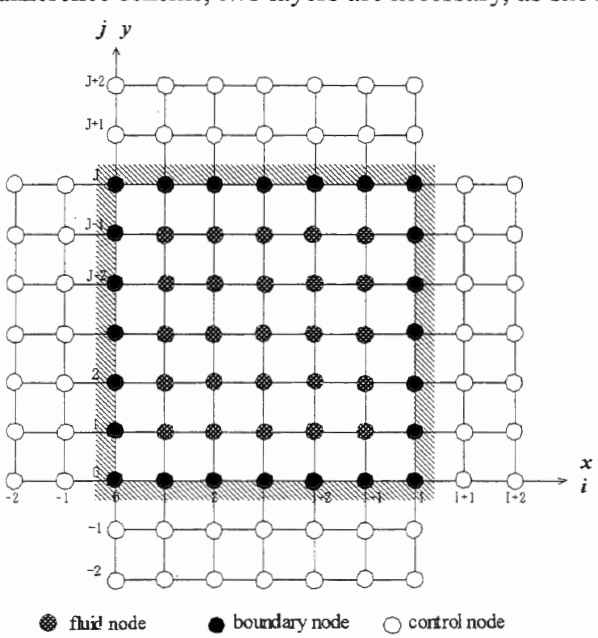

Figure 5.2. Sketch of the control node method.

Applying Euler scheme on time derivative, the following finite difference equation is derived from the evolution equation (5.1).

$$f_a^{n+1} = f_a^n - c_{ax}\frac{\partial f_a}{\partial x}\Delta t - c_{ay}\frac{\partial f_a}{\partial y}\Delta t - gE_{ay}^n\Delta t - \frac{1}{\phi}(f_a^n - f_a^{(0)n})\Delta t \quad (5.18)$$

$$\frac{\partial f_a}{\partial x} = \begin{cases} \left.\frac{\partial f_a}{\partial x}\right|^{+} = \frac{3f_a^n - 4f_{a,i-1}^n + f_{a,i-2}^n}{2\Delta x} \\ \left.\frac{\partial f_a}{\partial x}\right|^{-} = \frac{3f_a^n - 4f_{a,i+1}^n + f_{a,i+2}^n}{-2\Delta x} \end{cases} \quad (5.19)$$

$$\frac{\partial f_a}{\partial y} = \begin{cases} \left.\frac{\partial f_a}{\partial y}\right|^{+} = \frac{3f_a^n - 4f_{a,j-1}^n + f_{a,j-2}^n}{2\Delta y} \\ \left.\frac{\partial f_a}{\partial y}\right|^{-} = \frac{3f_a^n - 4f_{a,j+1}^n + f_{a,j+2}^n}{-2\Delta y} \end{cases} \quad (5.20)$$

where the suffix *ik* is written as *a* for simplicity, and the suffix *n* indicates the time step.

Spatial derivatives are defined differently depending on the direction of particle velocities. The upper parts of the equations (5.19) and (5.20) are for particles that have positive speed, and the lower parts for negative speed. Suffixes i-1, i-2, and j-1, j-2 indicate the nodes in x and y direction, respectively from the nominal node.

5.3.1. Boundary conditions on planar walls

Let us consider the boundary conditions on the left wall as an example (see Figure 5.3). We post an equilibrium-type distribution function $f_a^{(0)}(\rho_c, u_c, v_c, e_c)$ on the control node (-2, j). Assuming the distribution of the node (-1, j) is an average of the nodes (-2, j) and (0, j), the spatial derivative for positive particle velocities (rightward direction) is expressed as:

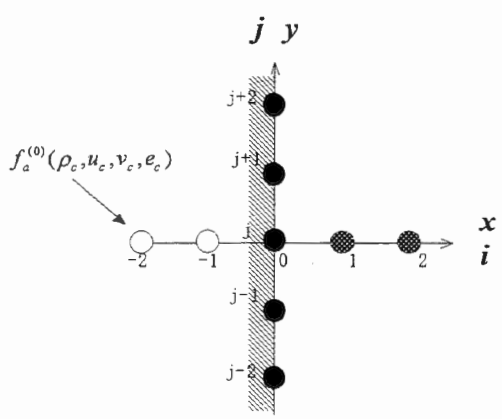

Figure 5.3. Left wall of the control node method.

$$\left.\frac{\partial f_a}{\partial x}\right|^{+} = \frac{3f_a^n - 4f_{a,-1}^n + f_{a,-2}^n}{2\Delta x} = \frac{f_a^n - f_a^{(0)}(\rho_c, u_c, v_c, e_c)}{2\Delta x} \tag{5.21}$$

Therefore, the finite difference evolution equation on the boundary node becomes

$$f_a^{n+1} = f_a^n - c_{ax}\left[\frac{f_a^n - f_a^{(0)}(\rho_c, u_c, v_c, e_c)}{2\Delta x \left.\frac{\partial f_a}{\partial x}\right|^{-}}\right]\Delta t - c_{ay}\frac{\partial f_a}{\partial y}\Delta t$$
$$- gE_{ay}^n \Delta t - \frac{1}{\phi}(f_a^n - f_a^{(0)n})\Delta t \tag{5.22}$$

In the [ ] of equation (5.22), the upper part is chosen for positive c_{ax} and the lower part for negative c_{ax}. The control distribution function $f_a^{(0)}(\rho_c, u_c, v_c, e_c)$ is used for the adjustment of boundary condition. If macroscopic quantities and/or their combinations are given as boundary conditions, these macroscopic requirements are expressed by moment summations on the distribution at the step $n+1$. Some examples are shown below.

$$\rho_w = \sum_a f_a^{n+1} \tag{5.23}$$

$$\rho_w u_w = \sum_a f_a^{n+1} c_{ax} \tag{5.24}$$

$$\rho_w v_w = \sum_a f_a^{n+1} c_{ay} \tag{5.25}$$

$$\rho_w\left(e_w + \frac{u_w^2 + v_w^2}{2}\right) = \sum_a f_a^{n+1}\frac{c_a^2}{2} \tag{5.26}$$

$$\rho_w [E.F.]_x = \sum_a f_a^{n+1}\frac{c_a^2}{2}c_{ax} \tag{5.27}$$

$$\rho_w [E.F.]_y = \sum_a f_a^{n+1}\frac{c_a^2}{2}c_{ay} \tag{5.28}$$

where $[E.F.]_\alpha$ is energy flux per unit mass in α direction. These requirements can be satisfied by adjusting ρ_c, u_c, v_c, e_c. Specific examples are given.

Wall example 1 (adiabatic with zero velocities)

The conditions of adiabatic wall with zero velocities are expressed as

$$\sum_a f_a^{n+1} c_{ax} = 0 \tag{5.29}$$

$$\sum_a f_a^{n+1} c_{ay} = 0 \tag{5.30}$$

$$\sum_a f_a^{n+1} \frac{c_a^2}{2} c_{ax} = 0 \tag{5.31}$$

Applying these conditions on the equation (5.22), we get the following equations.

$$\sum_+ c_{ax}^2 \left[f_a^n - f_a^{(0)}(\rho_c u_c v_c e_c) \right] \frac{\Delta t}{2\Delta x} = \sum_a c_{ax} H_a - \sum_- c_{ax}^2 \frac{\partial f_a}{\partial x} \Delta t \tag{5.32}$$

$$\sum_+ c_{ax} c_{ay} \left[f_a^n - f_a^{(0)}(\rho_c u_c v_c e_c) \right] \frac{\Delta t}{2\Delta x} = \sum_a c_{ay} H_a - \sum_- c_{ax} c_{ay} \frac{\partial f_a}{\partial x} \Delta t \tag{5.33}$$

$$\sum_+ \frac{c_a^2}{2} c_{ax}^2 \left[f_a^n - f_a^{(0)}(\rho_c u_c v_c e_c) \right] \frac{\Delta t}{2\Delta x} = \sum_a \frac{c_a^2}{2} c_{ax} H_a - \sum_- \frac{c_a^2}{2} c_{ax}^2 \frac{\partial f_a}{\partial x} \Delta t \tag{5.34}$$

where

$$H_a = f_a^n - c_{ay} \frac{\partial f_a}{\partial y} \Delta t - g E_{ay}^n \Delta t - \frac{1}{\phi} (f_a^n - f_a^{(0)n}) \Delta t \tag{5.35}$$

$\sum_+$ means the summation over positive c_{ax}, $\sum_-$ over negative c_{ax}, and $\sum_a$ over all c_{ax}.

We have four degrees of freedom: ρ_c, u_c, v_c, e_c, against three conditions. It is physically understandable that u_c strongly affects on the requirement $\rho_w u_w = 0$, v_c on $\rho_w v_w = 0$, and e_c on $\rho_w [E.F]_x = 0$. The ρ_c affects evenly on each requirement, however, the effect is quite small. Therefore, equations (5.32) through (5.34) are solved by adjusting u_c, v_c, e_c in the control distribution function. The density ρ_c is extrapolated from the fluid domain (Figure 5.4).

$$\rho_c = 3\rho_0 - 2\rho_1 \tag{5.36}$$

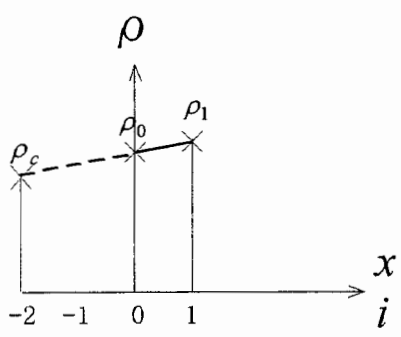

Figure 5.4. Density extrapolation in the control node method.

Equations (5.32) through (5.34) are solved by Newton Raphson method assuming following iteration equation:

$$f_a^{(0)}(\rho_c, u_c, v_c, e_c) = f_a^{(0)}(\rho_c, u_{c0}, v_{c0}, e_{c0}) + \frac{\partial f_a^{(0)}}{\partial u} \Delta u_c + \frac{\partial f_a^{(0)}}{\partial v} \Delta v_c + \frac{\partial f_a^{(0)}}{\partial e} \Delta e_c \tag{5.37}$$

where u_{c0}, v_{c0}, e_{c0} are initial estimated values and Δu_c, Δv_c, and Δe_c are their deviations. Following sensitivity functions are readily available by differentiating the equilibrium distribution function.

$$\frac{\partial f_a^{(0)}}{\partial u} = \rho_c F_k \frac{\partial \varphi_{ki}^{(0)}}{\partial u} \tag{5.38}$$

$$\frac{\partial f_a^{(0)}}{\partial v} = \rho_c F_k \frac{\partial \varphi_{ki}^{(0)}}{\partial v} \tag{5.39}$$

$$\frac{\partial f_a^{(0)}}{\partial e} = \rho_c \left(\frac{\partial F_k}{\partial e}\varphi_{ki}^{(0)} + F_k \frac{\partial \varphi_{ki}^{(0)}}{\partial e}\right) \tag{5.40}$$

The convergence in iteration is quite fast. Three times of the iteration are enough.

Wall example 2 (constant temperature (or internal energy e_w) with non-zero velocities: u_w, v_w)

These conditions are expressed as

$$\sum_a f_a^{n+1}(u_w - c_{ax}) = 0 \tag{5.41}$$

$$\sum_a f_a^{n+1}(v_w - c_{ay}) = 0 \tag{5.42}$$

$$\sum_a f_a^{n+1}\left[\left(e_w + \frac{u_w^2 + v_w^2}{2}\right) - \frac{c_a^2}{2}\right] = 0 \tag{5.43}$$

Like the wall example 1, ρ_c is estimated from the fluid domain and the equations above are solved in terms of u_c, v_c, and e_c.

5.3.2. Boundary conditions on corners

The example of a lower left corner is shown in Figure 5.5. Control distribution functions are placed on the two nodes: $f_a^{(0)}(\rho_x, u_x, v_x, e_x)$ on the node (-2,0), and $f_a^{(0)}(\rho_y, u_y, v_y, e_y)$ on the node (0,-2).

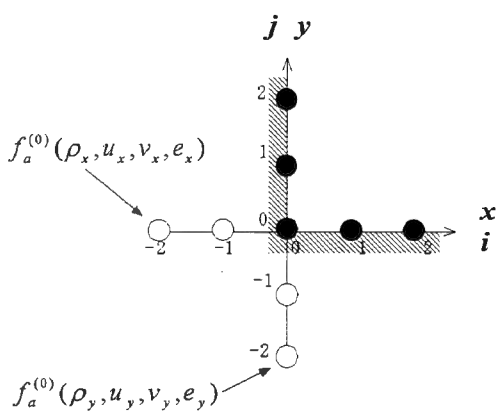

Figure 5.5. Lower left corner of control node method.

The distributions on the nodes (-1,0) and (0,-1) are averaged values of their both sides. Then, the evolution equation on the corner (0,0) becomes:

$$f_a^{n+1} = f_a^n - c_{ax}\left[\frac{f_a^n - f_a^{(0)}(\rho_x, u_x, v_x, e_x)}{\left.\frac{2\Delta x}{\frac{\partial f_a}{\partial x}}\right|^-}\right]\Delta t - c_{ay}\left[\frac{f_a^n - f_a^{(0)}(\rho_y, u_y, v_y, e_y)}{\left.\frac{2\Delta y}{\frac{\partial f_a}{\partial y}}\right|^-}\right]\Delta t - gE_{ay}^n\Delta t - \frac{1}{\phi}(f_a^n - f_a^{(0)n})\Delta t \tag{5.44}$$

The relationship between macroscopic quantity requirements and the distribution function of the step n+1 are similar to the case of wall. However, we have eight variables for boundary control: ρ_x, u_x, v_x, e_x, ρ_y, u_y, v_y, e_y. Appropriate variables have to be selected according to boundary conditions, and others are fixed at values extrapolated from the fluid domain. Let us show specific procedures according to the following examples.

Corner example 1 (adiabatic with zero velocities)

The requirement for zero velocity u_w=0 is adjusted by the control variable u_x of the node (-2,0) and the requirement for zero energy flux in x direction is by e_x. The situation in y direction is the same as in x direction. Namely, v_w=0 is by v_y , and zero energy flux in y direction is by e_y . Other variables yield minor effects. Therefore, during iteration process, the following variables are fixed at values extrapolated from the fluid domain:

$$\rho_x = 3\rho_0^0 - 2\rho_0^1 \tag{5.45}$$

$$\rho_y = 3\rho_0^0 - 2\rho_1^0 \tag{5.46}$$

$$v_x = 0 \tag{5.47}$$

$$u_y = 0 \tag{5.48}$$

Boundary condition requirements expressed by following equations are solved by adjusting the control variables: u_x , v_y , e_x , and e_y.

$$\sum_a f_a^{n+1} c_{ax} = 0 \tag{5.49}$$

$$\sum_a f_a^{n+1} c_{ay} = 0 \tag{5.50}$$

$$\sum_a f_a^{n+1} \frac{c_a^2}{2} c_{ax} = 0 \tag{5.51}$$

$$\sum_a f_a^{n+1} \frac{c_a^2}{2} c_{ay} = 0 \tag{5.52}$$

Corner example 2 (adiabatic on the lower side, constant temperature (or internal energy e_w) on the left side, and zero velocities)

Same as the previous example, ρ_x, ρ_y, v_x, and u_y are fixed at extrapolated values. Control variables u_x, v_y, e_x, and e_y are used to solve following equations.

$$\sum_a f_a^{n+1} c_{ax} = 0 \tag{5.53}$$

$$\sum_a f_a^{n+1} c_{ay} = 0 \tag{5.54}$$

$$\sum_a f_a^{n+1} (e_w - \frac{c_a^2}{2}) = 0 \tag{5.55}$$

$$\sum_a f_a^{n+1} \frac{c_a^2}{2} c_{ay} = 0 \tag{5.56}$$

5.4. Extrapolation method

This method is a modification of McNamara.[7] The sketch of this method is shown in Figure 5.6.

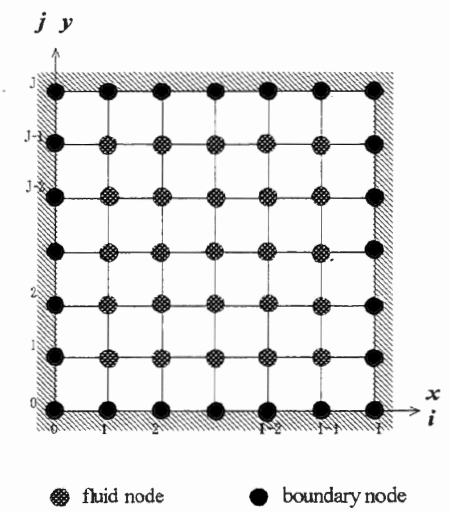

Figure 5.6. Sketch of the extrapolation method.

Distribution function is divided into two parts. One is equilibrium distribution function $f_a^{(0)}$ and the other is non-equilibrium part $f_a^{(1)}$. The macroscopic quantities: ρ, u_α, e, are represented by $f_a^{(0)}$ and quantities, such as stress tensors, are represented by $f_a^{(1)}$.

$$f_a = f_a^{(0)} + f_a^{(1)} \tag{5.57}$$

In most cases, boundary conditions are given as the macroscopic quantities: ρ, u_a, e. In order to guarantee the continuity of stress tensors, it is enough to assure the continuity of $f_a^{(1)}$ in stead of knowing individual tensors. In prior to applying the evolution equation on fluid node, the distribution functions on boundary nodes are arranged so that the equilibrium part satisfies the boundary condition explicitly stated and the non-equilibrium part is continuous.

Same as control node method, second order upwind scheme was applied on most of fluid nodes. However, first order upwind scheme was applied onto the outermost fluid nodes. Let us show specific examples.

Wall example 1 (constant temperature (or internal energy e_w) with non-zero velocities: u_w, v_w)

Density on the wall, which is not required as boundary condition, is extrapolated from the fluid domain by a quadratic fit (Figure 5.7).

$$\rho_0 = 3\rho_1 - 3\rho_2 + \rho_3 \tag{5.58}$$

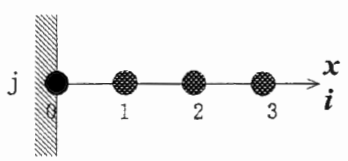

Figure5.7. Left wall of the extrapolation method.

Non-equilibrium distribution, which is defined as the difference between the distribution and the equilibrium distribution, is linearly extrapolated from the fluid domain.

$$[f_a - f_a^{(0)}]_0 = 2[f_a - f_a^{(0)}]_1 - [f_a - f_a^{(0)}]_2 \tag{5.59}$$

Consequently, the distribution function on the boundary node $(0, j)$ is given by

$$f_a = f_a^{(0)}(\rho_0, u_w, v_w, e_w) + [f_a - f_a^{(0)}]_0 \tag{5.60}$$

Wall example 2 (adiabatic wall)

If adiabatic condition is required instead of being given as temperature itself, the temperature, or internal energy is given by extrapolation from the fluid domain, assuming quadratic equation and vertex on the boundary (see Figure 5.8).

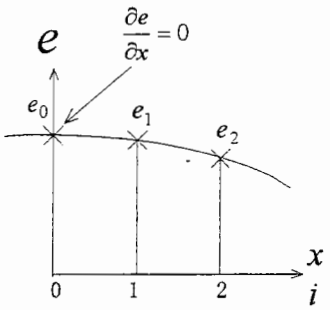

Figure 5.8. Extrapolation for adiabatic condition.

$$e_0 = \frac{1}{3}(4e_1 - e_2) \tag{5.61}$$

Distribution on corners

The evolution equation is applied only on fluid nodes, which do not use any information of corners. Therefore, the distribution functions on corners are not necessary to solve flows. However, if a complete set of the distributions is desired, the following extrapolation procedure is applied (Figure 5.9).

$$\rho_0^0 = \rho_1^0 + \rho_0^1 - \rho_1^1 \tag{5.62}$$

$$e_0^0 = e_1^0 + e_0^1 - e_1^1 \tag{5.63}$$

$$[f_a - f_a^{(0)}]_0^0 = [f_a - f_a^{(0)}]_1^0 + [f_a - f_a^{(0)}]_0^1 - [f_a - f_a^{(0)}]_1^1 \tag{5.64}$$

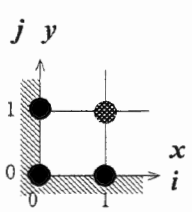

Figure 5.9. Lower left corner of extrapolation method.

5.5. Benchmark test

The performance of the two methods were evaluated in three tests.

Recovery of hydrostatic equilibrium

Thermal cavity flow

Thermal Couette flow

5.5.1. Recovery of hydrostatic equilibrium

Initially, a rectangular box of the size of $L \times L$ is filled with uniform fluid of density ρ_0 and internal energy e_0. Gravity g is added at t=0 and on. The boundaries are adiabatic with zero velocities. At an early stage, the momentum equilibrium is recovered, resulting higher temperature in lower part of the fluid and lower temperature in the upper part. Thereafter, long process for acquiring energy equilibrium, namely, process to uniform temperature, follows.
The final pressure distribution along vertical axis y should be:

$$P = \rho_0 e_0 \exp\left[-\frac{g(y - L/2)}{e_0}\right] \tag{5.65}$$

The time of about 4000 in FDLBM time-units was required to get uniform temperature. The mass ρ and the energy E, which is calculated by following formula, at the nodes of 21×21 are summed in each time step.

$$E = \rho\left[e + \frac{u^2}{2} + g(y - L/2)\right] \tag{5.66}$$

Histories of the summed values of mass and energy, divided by the values at t=0, are shown in Figure 5.10. The final pressure distribution is shown in Figure 5.11. The conservation of mass and energy is excellent for the control node method, resulting in a good agreement in pressure distribution with the analysis. The performance of the extrapolation method is satisfactory, though some leak-in was observed, resulting in a higher pressure in the equilibrium state.

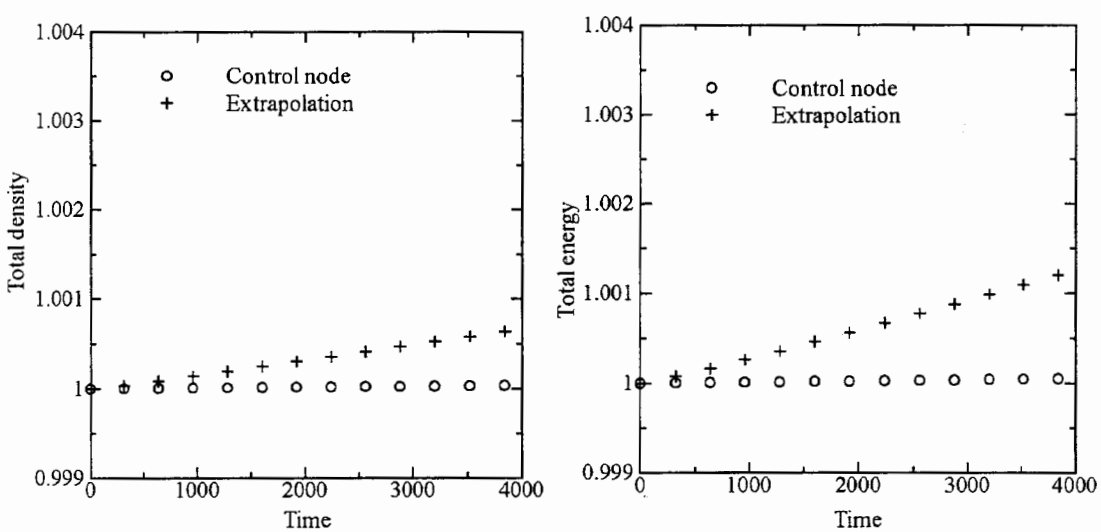

(a) Conservation of the density (b) Conservation of the energy

Figure 5.10. Conservation of the density and the energy.

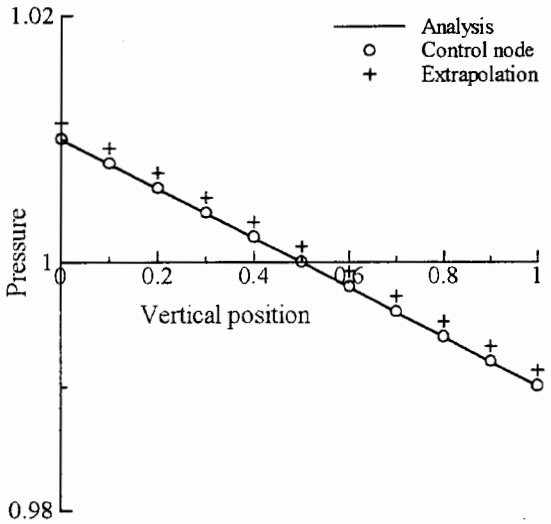

Figure 5.11. Pressure equilibrium.

5.5.2. Thermal cavity flow

The sketch of the simulation is shown in Figure 5.12. Upper and lower walls are adiabatic. Left wall has higher temperature $T_0+\Delta T/2$ (or internal energy $e_0+\Delta e$) and right wall has lower temperature $T_0-\Delta T/2$ (or internal energy $e_0-\Delta e$). Due to the buoyancy caused by the temperature difference, clockwise flow is generated.

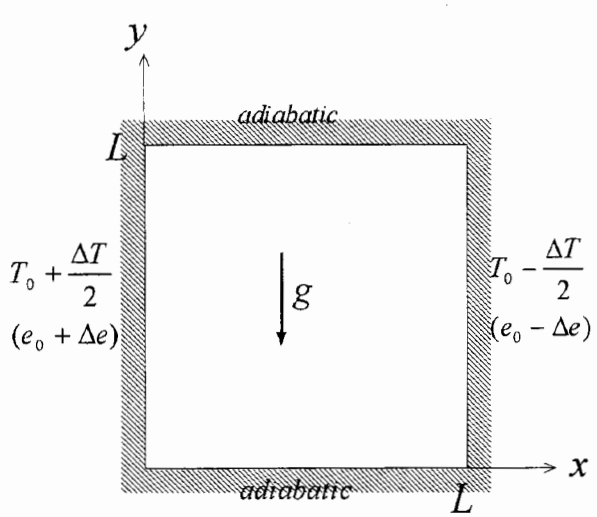

Figure 5.12. Sketch of the thermal cavity flow.

To compare the result with the solution for Boussinesq approximation, the numerical simulations were conducted for small gravity and small temperature difference. The non-dimensional equations for Boussinesq approximation are derived from the Navier-Stokes equations assuming that the speed of flow is small, the density changes only by temperature

variation, the dissipation of kinetic energy into heat can be neglected, and the physical properties are considered constant over the flow domain.[8]

$$\frac{\partial \bar{u}_\alpha}{\partial \bar{r}_\alpha} = 0 \tag{5.67}$$

$$\frac{\partial \bar{u}_\alpha}{\partial \bar{t}} + \bar{u}_\beta \frac{\partial \bar{u}_\alpha}{\partial \bar{r}_\beta} + \frac{\partial \bar{P}^*}{\partial \bar{r}_\alpha} - P_r \frac{\partial}{\partial \bar{r}_\beta}\left(\frac{\partial \bar{u}_\beta}{\partial \bar{r}_\alpha} + \frac{\partial \bar{u}_\alpha}{\partial \bar{r}_\beta}\right) - GrP_r^2 \bar{T}^* i_\alpha = 0 \tag{5.68}$$

$$\frac{\partial \bar{T}^*}{\partial \bar{t}} + \bar{u}_\alpha \frac{\partial \bar{T}^*}{\partial \bar{r}_\alpha} - \frac{\partial \bar{T}^*}{\partial \bar{r}_\alpha} = 0 \tag{5.69}$$

where T^* and P^* are variations from T_0 and hydrostatic pressure distribution, respectively. The variables with cap "–" are non-dimensional quantities normalized by characteristic values: length L, speed κ/L , and temperature difference $\Delta T(=2\,\Delta e/R)$. The i_α is a unit vector (0 , 1). Parameters that characterize the flow: Grashof number G_r and Prandtl number P_r, are defined as,

$$G_r = \frac{\beta g \Delta T L^3}{\nu^2} \tag{5.70}$$

$$P_r = \frac{\nu}{\kappa} \tag{5.71}$$

where

$$\beta = -\frac{1}{\rho_0}\left(\frac{\partial \rho}{\partial T}\right)_p = \frac{1}{T_0} = \frac{R}{e_0} : \text{thermal expansion parameter}$$

$$\nu = \frac{\mu}{\rho_0} : \text{kinetic viscosity} \tag{5.72 abc}$$

$$\kappa = \frac{R\kappa'}{\rho_0 c_p} : \text{thermal conductivity}$$

Numerical simulations for Grashof number=10^3 (Prandtl number is unity for BGK model) were conducted, varying the meshes: 21×21, 41×41, 81×81, and 161×161. The acquisition of steady state was judged when the relative variation of the maximum flow speed became less than 5×10^{-4} in 100 FDLBM time-units. About 3200 time-units was required in most cases.

The general view of velocity vectors and temperature contours for the mesh of 161×161 is shown in Figure 5.13. Horizontal velocity along mid-vertical axis and vertical velocity along mid-horizontal axis are shown in Figure 5.14. Temperature distribution at upper boundary, mid position, and lower boundary are shown in Figure 5.15. In these figures, Boussinesq solutions are also shown. Corresponding Boussinesq solution was obtained using the software of HSMAC method,[9] whose adequacy was confirmed by comparing it with the results of reference.[10] Although some differences due to the departure from Boussinesq approximation are observed in the results, agreements are generally good.

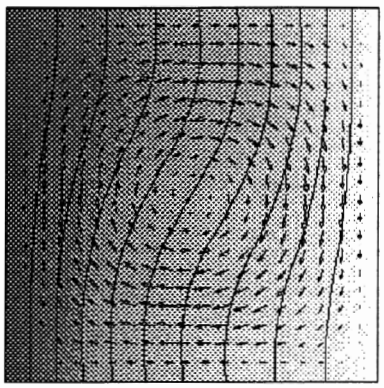

Figure 5.13. Velocity vectors and temperature contours of thermal cavity flow.

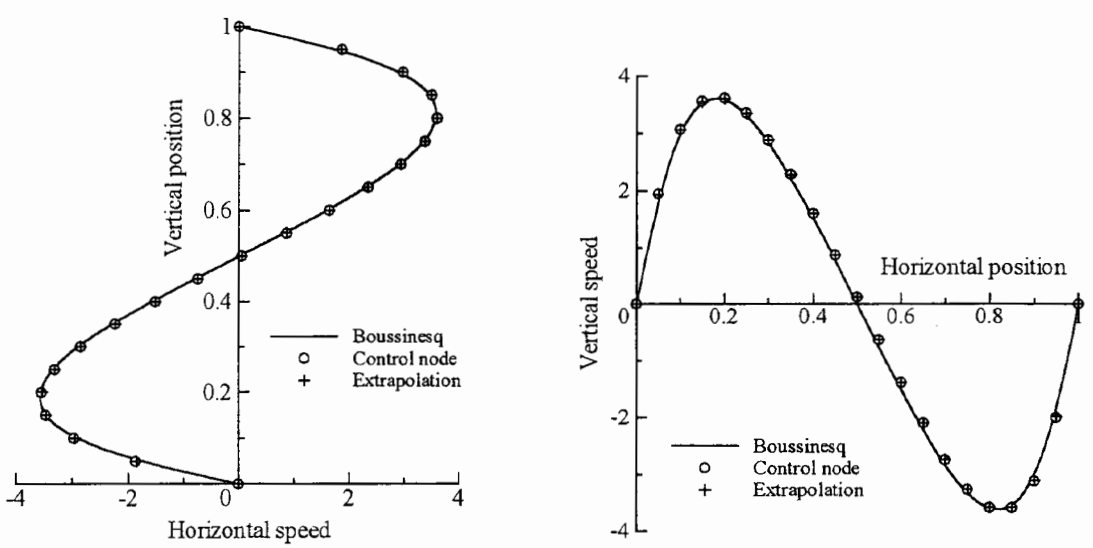

(a) Horizontal speed along mid-vertical axis (b) Vertical speed along mid-horizontal axis

Figure 5.14. Velocity distribution of thermal cavity flow.

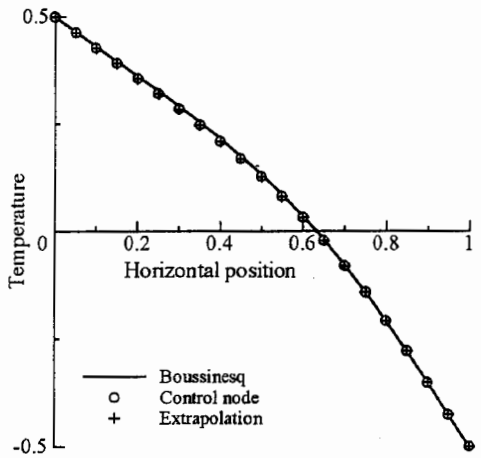

(a) Temperature distribution at upper wall

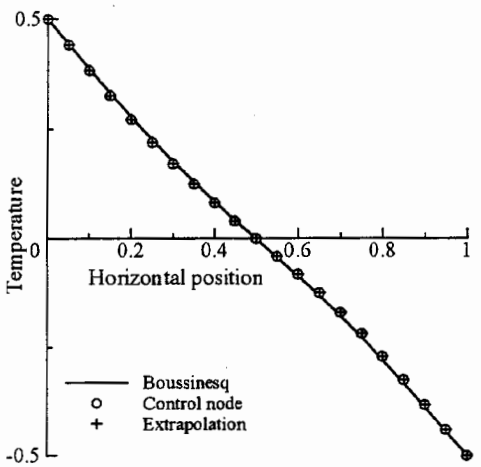

(b) Temperature distribution at mid position

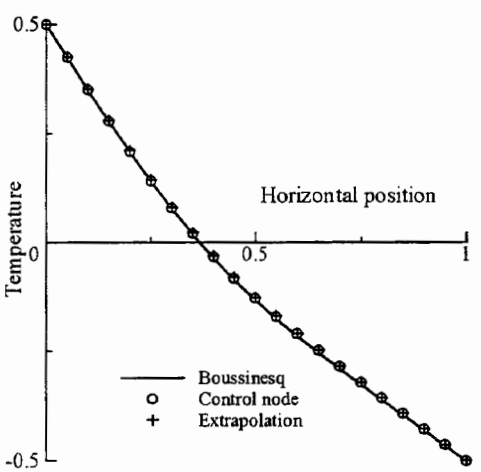

(c) Temperature distribution at lower wall

Figure 5.15. Temperature distribution of thermal cavity flow.

To confirm the convergence rate, error norms of velocity E_u and of temperature E_T are calculated by following formulas. The reference values: $\bar{u}_\infty, \bar{v}_\infty, \bar{T}^*_\infty$ are taken from the solution for the highest resolution 161×161, and the summation is taken for the common nodes of 21 $\times 21$.

$$E_u = \frac{\sqrt{\sum(\bar{u}-\bar{u}_\infty)^2 + \sum(\bar{v}-\bar{v}_\infty)^2}}{\sqrt{\sum \bar{u}_\infty{}^2 + \sum \bar{v}_\infty{}^2}} \tag{5.73}$$

$$E_T = \frac{\sqrt{\sum(\bar{T}^*-\bar{T}^*_\infty)^2}}{\sqrt{\sum \bar{T}^{*2}_\infty}} \tag{5.74}$$

The results are shown in Figure 5.16. The solution converges nearly at the rate of third order for both methods

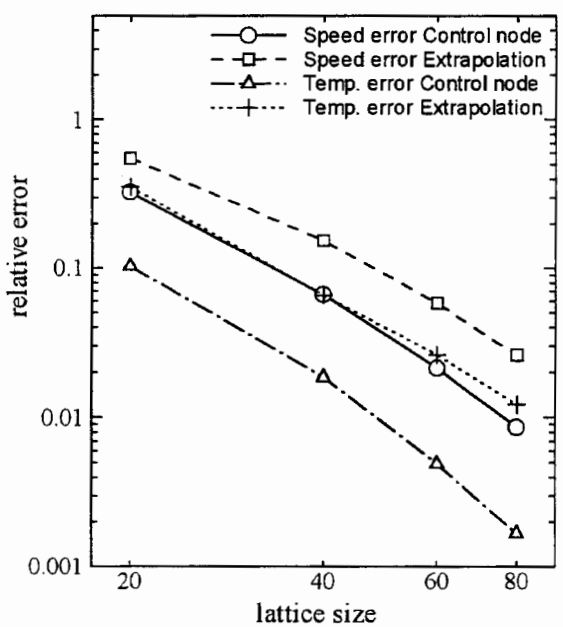

Figure 5.16. Convergence with mesh sizes.

5.5.3. Thermal Couette flow

The geometry of the flow is sketched in Figure 5.17. The upper wall, which is L apart from the lower wall, is moving at a speed of U and has an internal energy e_2. The lower wall is at rest and has e_1. The right and left boundaries are assumed periodic.

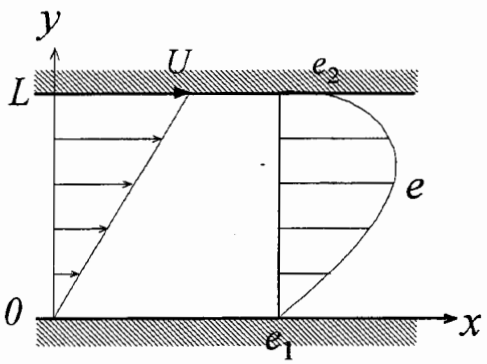

Figure 5.17. Sketch of the thermal Couette flow

Assuming $\partial/\partial t=0$, $\partial/\partial x=0$, and $v=0$, we obtain analytical solutions for internal energy e along vertical axis ($\tilde{y} = y/L$).

$$\frac{e-e_1}{e_2-e_1} = \tilde{y} + \frac{\mu U^2}{2\kappa'(e_2-e_1)}\tilde{y}(1-\tilde{y}) \quad \text{for} \quad e_2>e_1 \tag{5.75}$$

$$\frac{e-e_1}{e_0} = \frac{\mu U^2}{2\kappa' e_0}\tilde{y}(1-\tilde{y}) \quad \text{for} \quad e_2=e_1=e_0 \tag{5.76}$$

Simulation result for $e_2=e_1$ is shown in Figure 5.18 and for $e_2>e_1$ in Figure 5.19. Excellent agreement with the analytical solution for the control node method and less but still good agreement for the extrapolation method are shown.

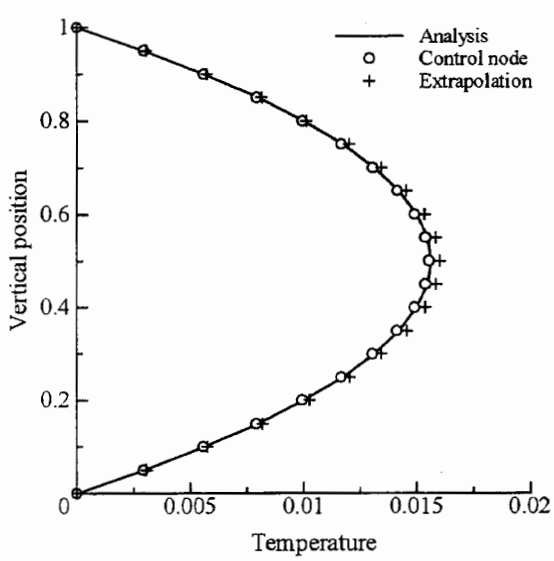

Figure 5.18. Temperature distribution for $e_2 = e_1$.

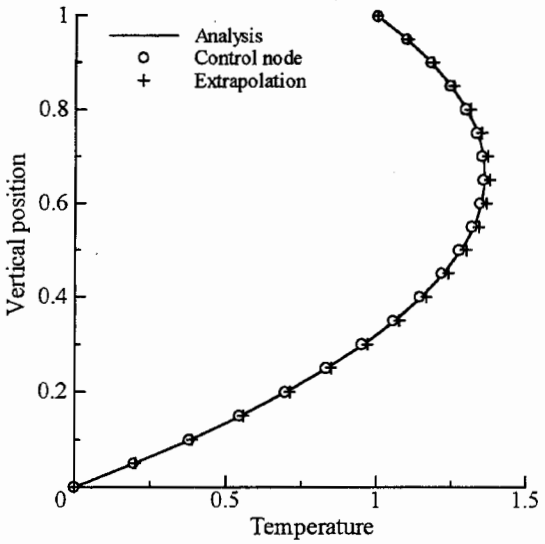

Figure 5.19. Temperature distribution for $e_2 > e_1$.

5.6. Conclusions

Two methods of boundary conditions that can be applied to thermal models of FDLBM were studied and were evaluated by three tests.

First method, called "control node method," can handle wide variety of boundary conditions and showed excellent performance on the tests. The structure is slightly complicated and it seems rather tedious to make computing software. However, if accurate simulation is desired, control node method should be used.

Second method, called "extrapolation method" is simple. Making computing software is quite easy and the performance is assured to some extent. It is a viable method if it is not required strict accuracy.

References

[1] T. Inamuro, M. Yoshino and F. Ogino, "A non-slip boundary condition for lattice Boltzmann simulations", Phys. Fluids 7: 2928 (1995).

[2] P. A. Skordos, "Initial and boundary conditions for the lattice Boltzmann method ", Phys. Rev. E 48: 4823 (1993).

[3] R. S. Maier, R. S. Bernard and D. W. Grunau, "Boundary conditions for the lattice Boltzmann method ", Phys. Fluids 8: 1788 (1996).

[4] D. R. Noble, S. Chen, J. G. Georgiadis and R. O. Buckius, "A consistent hydrodynamic boundary condition for the lattice Boltzmann method ", Phys. Fluids 7: 203 (1995).

[5] S. Chen, D. Martinez and R. Mei, "On boundary conditions in lattice Boltzmann methods", Phys. Fluids 8: 2527 (1996).

[6] Q. Zou, X.He, "On pressure and velocity boundary conditions for the lattice Boltzmann BGK model", Phys. Fluids 9: 1591 (1997).

[7] G. R. McNamara, A. L. Garcia, and B. J. Alder, "Stabilization of thermal lattice Boltzmann models ", J. Stat. Phys. 81: 395 (1995).

[8] L. D. Landau and E. M. Lifshitz "Fluid mechanics" Oxford, 1987.

[9] H. Kawamura and K. Hijikata, "Simulation of heat and flow", Maruzen, (1995) (in Japanese).

[10] G. D. V. Davis, "Natural convection of air in a square cavity: A bench mark numerical solution", J. Numer. Meth. Fluids 3: 249 (1983).

6. Thermal cavity flow of compressible fluids -Numerical simulation by a newly proposed model of finite difference lattice Boltzmann method

6.1. Introduction

Numerical simulations have been extensively performed on natural convection in a square cavity. Most of these studies are for Boussinesq fluid.[1,2] Although some studies[3,4] treat the flows as compressible fluid, they do not state clearly how much compressibility affects the flows and how far the Boussinesq approximation is considered valid.

The finite difference lattice Boltzmann method (FDLBM) is a new numerical tool for simulating viscous fluid flows. While existing models of FDLBM for compressible fluid have drawbacks of poor numerical stability and narrow band of temperature, we developed an FDLBM model for compressible fluid that is very stable and can handle wide range of temperature.

Using this model, we studied thermal cavity flow for compressible fluids. The simulations were conducted by varying viscosity, gravity, and temperature difference in a systematic manner. Our objectives are to reveal how compressibility affects natural convection and to confirm the range over which Boussinesq approximation insists its validity.

6.2. Finite difference lattice Boltzmann method

6.2.1. Formulation

Below is the two-dimensional thermal FDLBM model used in this study. The evolution of the distribution function f_{ki} for particle velocity c_{ki} is governed by the following equation, which is solved using Euler and second upwind difference scheme.

$$\frac{\partial f_{ki}}{\partial t} + c_{ki\alpha}\frac{\partial f_{ki}}{\partial r_\alpha} - g_\alpha E_{ki\alpha} = -\frac{1}{\phi}(f_{ki} - f_{ki}^{(0)}) \tag{6.1}$$

where the subscript k indicates a group of particle velocities whose speed is c_k and i indicates its direction. The subscript α indicates x or y component. The variable t is time, r_α the spatial coordinate, g_α the gravity acceleration vector (0 , -g), $f_{ki}^{(0)}$ the local equilibrium distribution function, $E_{ki\alpha}$ the external force distribution function, and ϕ the relaxation parameter.

The particles consist of a rest particle and four groups of moving particles as shown in Figure 6.1.

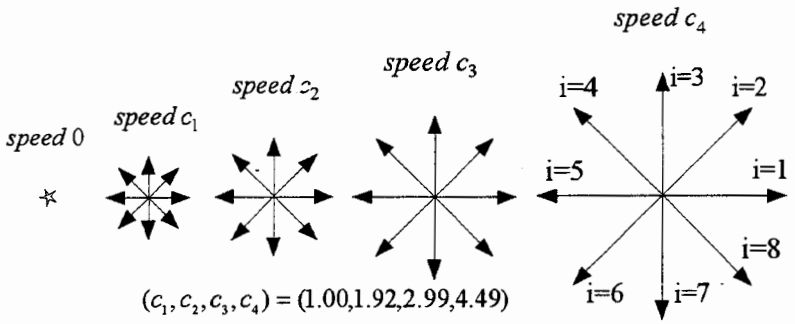

Figure 6.1. Particle velocities.

While existing models adopt the group of square directions, which has up-to second rank tensor isotropy, or adopt the group of hexagonal directions, which has up-to fourth rank tensor isotropy, our model is based on the group of octagonal directions, which has sixth rank tensor isotropy. This high isotropy contributes to the numerical stability and the applicability to wide range of temperature.

Macroscopic quantities, the density ρ, the velocity u_α, and the internal energy e, are defined as follows.

$$\rho = \sum_{ki} f_{ki} \tag{6.2}$$

$$\rho u_\alpha = \sum_{ki} f_{ki} c_{ki\alpha} \tag{6.3}$$

$$\rho(e + \frac{u^2}{2}) = \sum_{ki} f_{ki} \frac{c_k^2}{2} \tag{6.4}$$

The local equilibrium distribution function is defined as:

$$f_{ki}^{(0)} = \rho F_k \varphi_{ki}^{(0)} \tag{6,5}$$

$$\begin{aligned} \varphi_{ki}^{(0)} &= (1 - \frac{u^2}{2e} + \frac{u^4}{8e^2}) + \frac{1}{e}(1 - \frac{u^2}{2e})(c_{ki\alpha}u_\alpha) \\ &+ \frac{1}{2e^2}(1 - \frac{u^2}{2e})(c_{ki\alpha}u_\alpha)^2 + \frac{1}{6e^3}(c_{ki\alpha}u_\alpha)^3 + \frac{1}{24e^4}(c_{ki\alpha}u_\alpha)^4 \end{aligned} \tag{6.6}$$

$$\begin{aligned} F_1 &= \frac{1}{c_1^2(c_1^2 - c_2^2)(c_1^2 - c_3^2)(c_1^2 - c_4^2)}[48e^4 \\ &- 6(c_2^2 + c_3^2 + c_4^2)e^3 + (c_2^2c_3^2 + c_3^2c_4^2 + c_4^2c_2^2)e^2 - \frac{c_2^2c_3^2c_4^2}{4}e] \end{aligned} \tag{6.7}$$

$$F_2 = \frac{1}{c_2^2(c_2^2-c_3^2)(c_2^2-c_4^2)(c_2^2-c_1^2)}[48e^4 - 6(c_3^2+c_4^2+c_1^2)e^3 + (c_3^2c_4^2+c_4^2c_1^2+c_1^2c_3^2)e^2 - \frac{c_3^2c_4^2c_1^2}{4}e] \quad (6.8)$$

$$F_3 = \frac{1}{c_3^2(c_3^2-c_4^2)(c_3^2-c_1^2)(c_3^2-c_2^2)}[48e^4 - 6(c_4^2+c_1^2+c_2^2)e^3 + (c_4^2c_1^2+c_1^2c_2^2+c_2^2c_4^2)e^2 - \frac{c_4^2c_1^2c_2^2}{4}e] \quad (6.9)$$

$$F_4 = \frac{1}{c_4^2(c_4^2-c_1^2)(c_4^2-c_2^2)(c_4^2-c_3^2)}[48e^4 - 6(c_1^2+c_2^2+c_3^2)e^3 + (c_1^2c_2^2+c_2^2c_3^2+c_3^2c_1^2)e^2 - \frac{c_1^2c_2^2c_3^2}{4}e] \quad (6.10)$$

$$F_0 = 1-8(F_1+F_2+F_3+F_4) \quad (6.11)$$

The external force distribution function is defined as

$$E_{ki\alpha} = -\frac{c_{ki\alpha}}{e}\rho F_k \varphi_{ki}^{(0)} + \rho F_k \frac{\partial \varphi_{ki}^{(0)}}{\partial c_{ki\alpha}} \quad (6.12)$$

By applying the Chapman-Enskog expansion, the above formulation is shown to be equivalent to the following fluid equations.

$$\frac{\partial \rho}{\partial t} + \frac{\partial}{\partial r_\alpha}(\rho u_\alpha) = 0 \quad (6.13)$$

$$\frac{\partial}{\partial t}(\rho u_\alpha) + \frac{\partial}{\partial r_\beta}(\rho u_\alpha u_\beta) + \frac{\partial P}{\partial r_\alpha} - \frac{\partial}{\partial r_\beta}[\mu(\frac{\partial u_\beta}{\partial r_\alpha} + \frac{\partial u_\alpha}{\partial r_\beta} - \frac{\partial u_\gamma}{\partial r_\gamma}\delta_{\alpha\beta})] + \rho g_\alpha = 0 \quad (6.14)$$

$$\frac{\partial}{\partial t}[\rho(e+\frac{u^2}{2})] + \frac{\partial}{\partial r_\alpha}[\rho u_\alpha(e+\frac{u^2}{2}+\frac{P}{\rho})] - \frac{\partial}{\partial r_\alpha}[\kappa'\frac{\partial e}{\partial r_\alpha} + \mu u_\beta(\frac{\partial u_\beta}{\partial r_\alpha} + \frac{\partial u_\alpha}{\partial r_\beta} - \frac{\partial u_\gamma}{\partial r_\gamma}\delta_{\alpha\beta})] = 0 \quad (6.15)$$

where

$P = \rho e$: the pressure

$\mu = \rho e \phi$: the viscosity coefficient (6.16 abc)

$\kappa' = 2\rho e \phi$: the heat conductivity

The following equation relates the temperature T with the internal energy (R: gas constant).

$$T = e/R \quad (6.17)$$

6.2.2. Validation of the method

The model is confirmed valid by two numerical simulations. First, the speed of sound was measured. The result, shown in Figure 6.2, indicates that sound speed obtained by the simulation agrees well with the theoretical value of equation (6.18).

$$c_s = \sqrt{2e} \tag{6.18}$$

Second, shear flow between parallel walls (Couette flow) was investigated. The upper wall, which is H apart from the lower wall and has internal energy e_2, starts to move with speed U. The lower wall has e_1 and is at rest. The result for e_1=e_2 is shown in Figure 6.3.

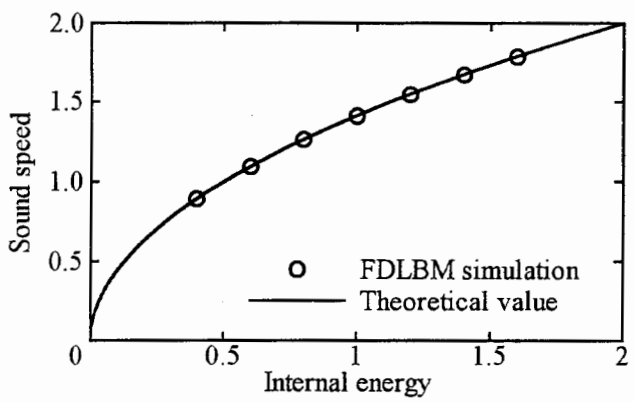

Figure 6.2. Simulation result of speed of sound.
Compared with the theoretical value (=$\sqrt{2e}$).

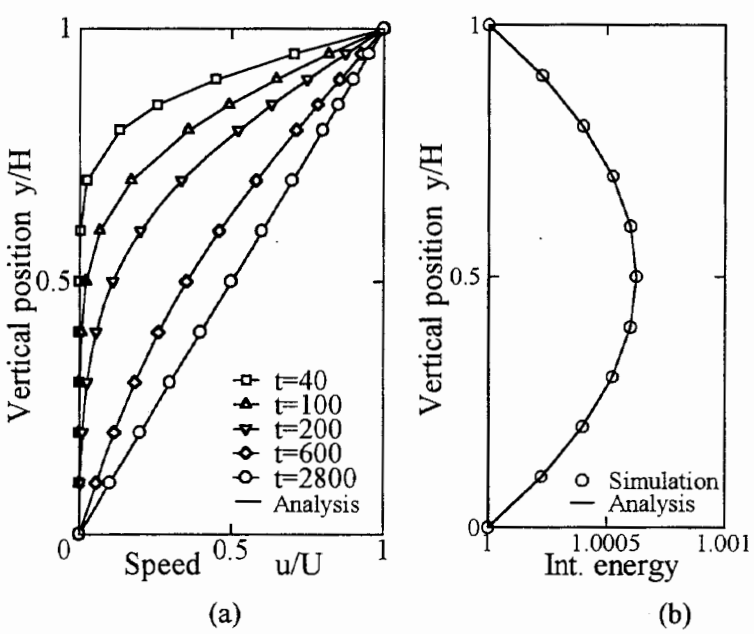

Figure 6.3. Couette flow. e_1=e_2=1.0. (a) Horizontal speed distribution at various instants. (b) Internal energy distribution at steady state.

The horizontal speed distribution along vertical axis y at various instants t, and the internal energy distribution at steady state, agree well with the theoretical values (6.19) and (6.20), respectively.

$$\frac{u}{U} = \frac{y}{H} - \frac{2}{\pi}\sum_{n=1}^{\infty} \exp\left[-n^2\pi^2 \frac{\mu t}{\rho H^2}\right] \sin\left[n\pi(1-\frac{y}{H})\right] \tag{6.19}$$

$$e - e_1 = \frac{\mu U^2}{2\kappa'} \frac{y}{H}(1-\frac{y}{H}) \tag{6.20}$$

6.3. Thermal cavity flow

The sketch of the simulation is shown in Figure 6.4. The upper and lower walls are adiabatic. The left wall has a higher temperature of $T_0 + \Delta T/2$ (or internal energy $e_0 + \Delta e$) than that of the right wall of $T_0 - \Delta T/2$ (or internal energy $e_0 - \Delta e$). Due to the buoyancy caused by the temperature difference, clockwise flow is generated.

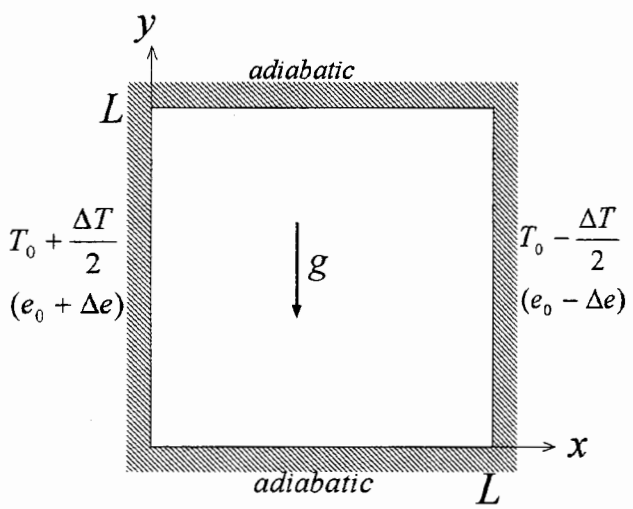

Figure 6.4. Sketch of the thermal cavity flow.

Parameters characterizing the flow are the Grashof number Gr, the Froude number Fr, the Prandtl number Pr, and the normalized temperature difference θ. The Prandtl number is unity in the single-relaxation (BGK) formulation.

$$Gr = \frac{g\beta_0 \Delta T L^3}{(\mu_0/\rho_0)^2} = \frac{g\Delta T L^3}{T_0(\mu_0/\rho_0)^2} = \frac{2g\Delta e L^3}{e_0^3 \phi^2} \tag{6.21}$$

$$Fr = \frac{\gamma R T_0}{gL} = \frac{2e_0}{gL} \tag{6.22}$$

$$\theta = \frac{\Delta T}{T_0} = \frac{2\Delta e}{e_0} \tag{6.23}$$

where suffix 0 denotes a mean value, β_0 the volume expansion parameter ($=-1/\rho(\partial\rho/\partial T)_p = 1/T_0$), and γ the specific heat ratio (=2 in the monatomic formulation).

Stream function ψ for compressible steady flows is calculated by integrating the following equations.

$$\frac{\partial \psi}{\partial x} = -\rho v \tag{6.24}$$

$$\frac{\partial \psi}{\partial y} = \rho u \tag{6.25}$$

The simulation starts from the initial condition as an equilibrium state in the vertical direction in the presence of gravity assuming the temperature field varies linearly in the horizontal direction.

Parametric study was conducted in the combinations of the Froude number, the normalized temperature difference, and the Grashof number, as shown in Figure 6.5.

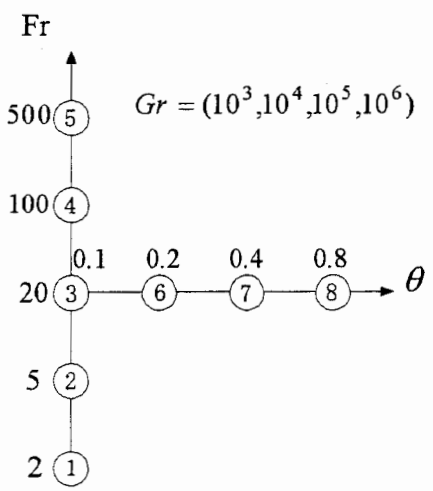

Figure 6.5. Cases of the numerical simulation.
The circled numbers are identified for combinations of Fr and θ.
At each combination, Gr varies from 10^3 to 10^6.

6.4. Results and discussions

6.4.1. Relevance of the mesh size

The effect of the mesh size on numerical accuracy was evaluated; an example is shown in Figure 6.6. Finer mesh is necessary as the Grashof number increases. We concluded the mesh in Table 6.1 to assure the accuracy of 1% both for velocity and temperature fields.

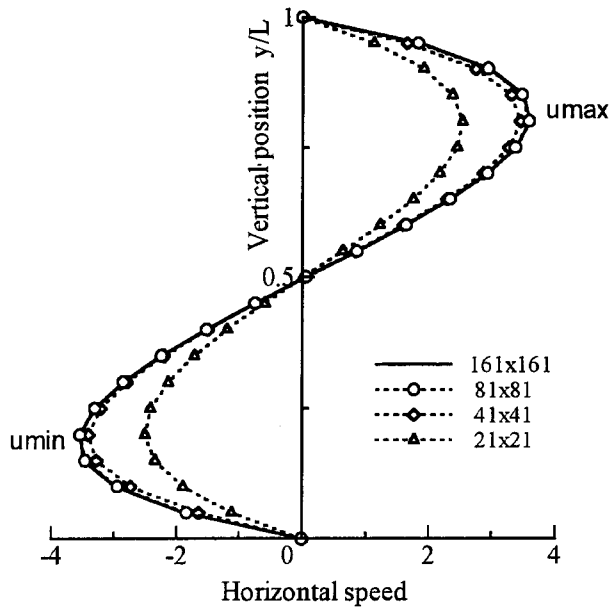

Figure 6.6. Numerical accuracy with mesh sizes. Horizontal speed along vertical centerline for the case of θ=0.1, Fr=20, Gr=10^3.

Table 6.1. Meshes of the numerical simulation

Gr	10^3	10^4	10^5	10^6
mesh	81×81	101×101	161×161	161×161

6.4.2. The Grashof number effect

The effect of the Grashof number for the case of θ=0.1 and Fr=20 is shown on the temperature contours in Figure 6.7, and on the stream function contours in Figure 6.8. As the Grashof number increases, temperature variation becomes concentrated next to the left and right walls (temperature boundary layers: TBL). In the central region between these layers, the fluid is in a stratified state as is typical in Figure 6.7(c) and (d); the upper fluid is warm and thin, while the lower fluid is cool and dense.

The stream function contour indicates that, at Gr=10^3, the circulation has a single core. However, as Gr increases the circulation becomes flattened and finally has two cores for Gr > 10^5. Let us take as an example the flow near the right wall at Gr=10^6. The down flow just outside the TBL transports the heat downward. Thus, as shown in Figure 6.9, locally inverted temperature distribution ($\partial e / \partial x \geq 0$) is exerted. A reverse phenomenon occurs on the left wall. This locally inverted temperature distribution induces secondary flows with closed streamlines there.

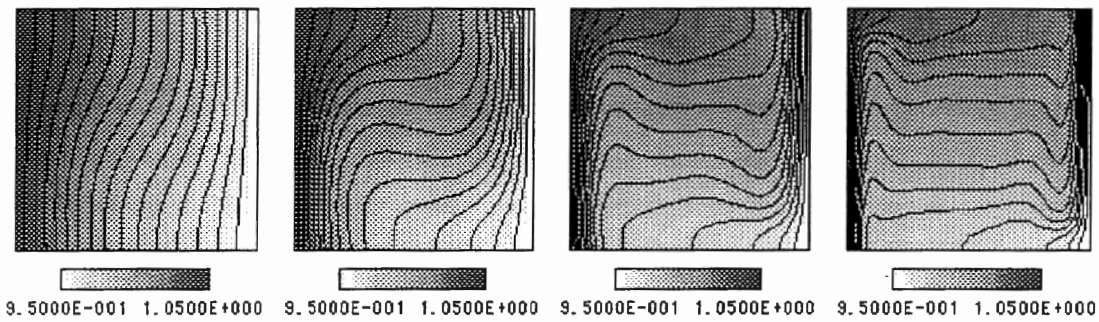

(a) Gr=10^3 (b) Gr=10^4 (c) Gr=10^5 (d) Gr=10^6

Figure 6.7. Temperature (e) contours for the case of θ=0.1, Fr=20.

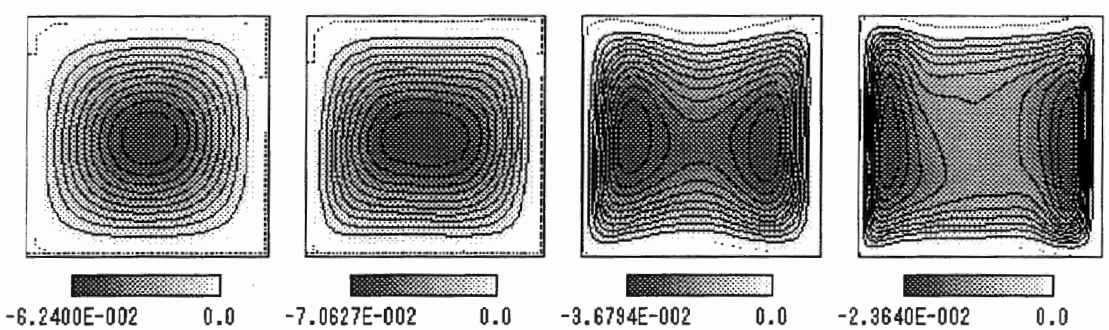

(a) Gr=10^3 (b) Gr=10^4 (c) Gr=10^5 (d) Gr=10^6

Figure 6.8. Stream function contours for the case of θ=0.1, Fr=20.

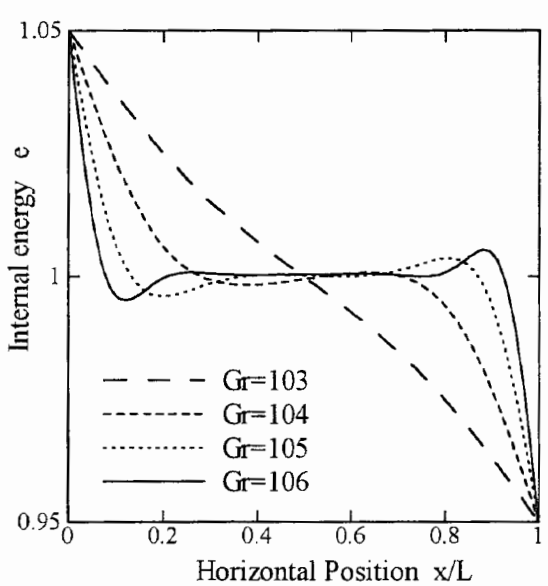

Figure 6.9. Temperature distribution along mid-depth horizontal line for the case of θ=0.1, Fr=20. Inverted temperature distribution ($\partial e/\partial x \geq 0$) near the walls are significant at Gr=10^5, 10^6.

6.4.3. Compressibility effect

The temperature contour at various Fr numbers for the combination of θ=0.1 and Gr=10^5 is shown in Figure 6.10. The temperature in the down flow near the right wall increases due to compressibility, as the fluid is descending. On the contrary, the fluid in the up flow near the left wall inflates to be cooled. Therefore, as Fr decreases (or the gravity increases), the gradient of temperature in TBL becomes steeper and the width of TBL becomes thinner.

The stream function, shown in Figure 6.11, indicates that the flow near the bottom prevails over the flow near the ceiling, as Fr decreases.

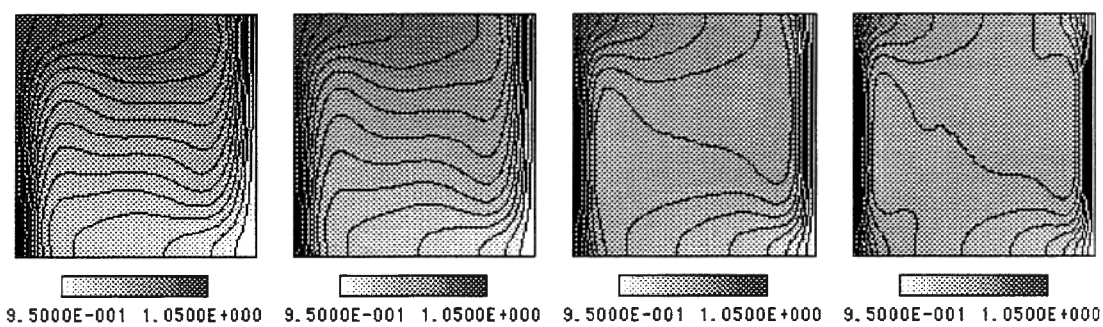

(a) Fr=100 (b) Fr=20 (c) Fr=5 (d) Fr=2

Figure 6.10. Temperature (e) contours for the case of θ=0.1, Gr=10^5.

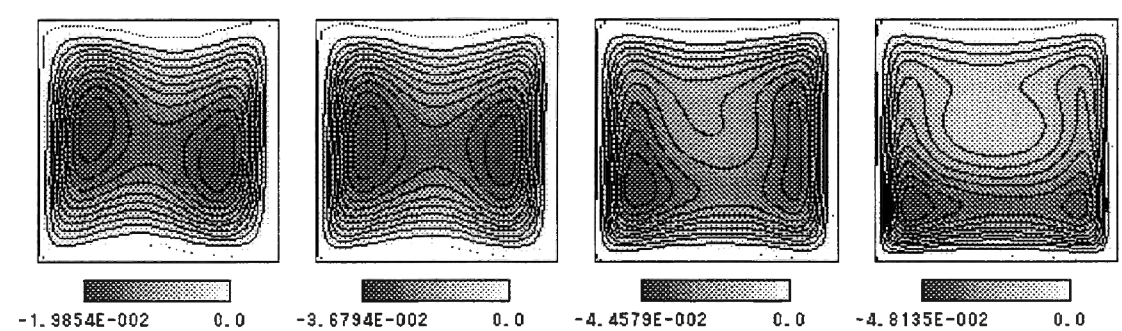

(a) Fr=100 (b) Fr=20 (c) Fr=5 (d) Fr=2

Figure 6.11. Stream function contours for the case of θ=0.1, Gr=10^5.

6.4.4. Temperature difference effect

The temperature difference is a source of convection. Therefore, as θ increases, circulation becomes stronger. At the same time, since the viscosity and heat conductivity are functions of temperature, asymmetry of the flow becomes significant. At $Gr=10^3$ the temperature varies more horizontally than vertically, therefore, horizontal asymmetry is significant as indicated in the stream functions of Figure 6.12 (a). On the other hand, at $Gr=10^6$ where temperature varies more vertically than horizontally, vertical asymmetry is significant (Figure 6.12 (b)).

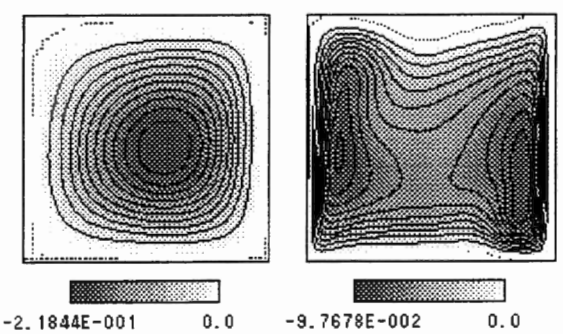

(a) $Gr=10^3$ (b) $Gr=10^6$

Figure 6.12. Stream function contours for the case of $\theta=0.8$, $Fr=20$.

6.4.5. Asymptotic behavior to Boussinesq fluid

As implied in Figure 6.5, the flow of small θ and large Fr leads to the Boussinesq flow. The simulation, varying Fr for combination of θ=0.1 and Gr=10^3, was conducted. The result was compared with the Boussinesq solution, which was obtained by the HSMAC method.[5] The peak speeds (maximum and minimum speeds) in the horizontal direction are shown in Figure 6.13. The peak speeds in the vertical direction are shown in Figure 6.14. These figures clearly indicate that the flow approaches to the Boussinesq flow as Fr increases. The Boussinesq assumption is considered valid when $Fr \geqq 100$ and $\theta \leqq 0.1$.

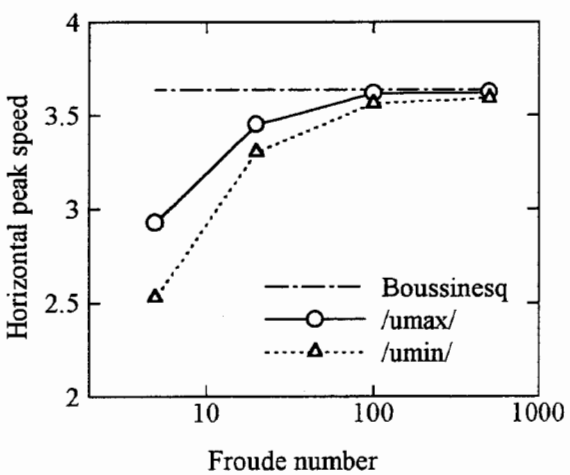

Figure 6.13. The peak speeds in the horizontal direction at different Fr numbers for θ=0.1, Gr=10^3.

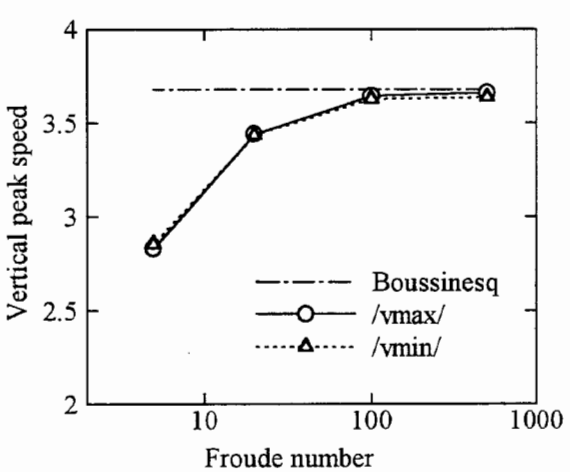

Figure 6.14. The peak speeds in the vertical direction at different Fr numbers for θ=0.1, Gr=10^3.

6.4.6. Heat transfer characteristics

Heat transfer characterized by the averaged Nusselt number was calculated at the walls by the following equation.

$$Nu = -\int_0^L \frac{\kappa'}{\kappa'_0} \frac{\partial}{\partial x}\left(\frac{T}{\Delta T}\right) dy \tag{6.26}$$

The value at the left wall (higher temperature) is slightly larger than that at the right wall. The result at the left wall is shown, as a function of *Gr* and *Fr*, in Figure 6.15 (a). In the figure, the value of the Boussinesq approximation is also shown. The figure indicates that compressibility assists the increase of heat transfer.

The result as a function of *Gr* and θ is shown in Figure 6.15 (b). The Nusselt number is less sensitive to θ, or it slightly decreases as θ increases, which is the opposite result to the simulation study by Leonardi et al.[4], who say the Nusselt number increases as θ increases.

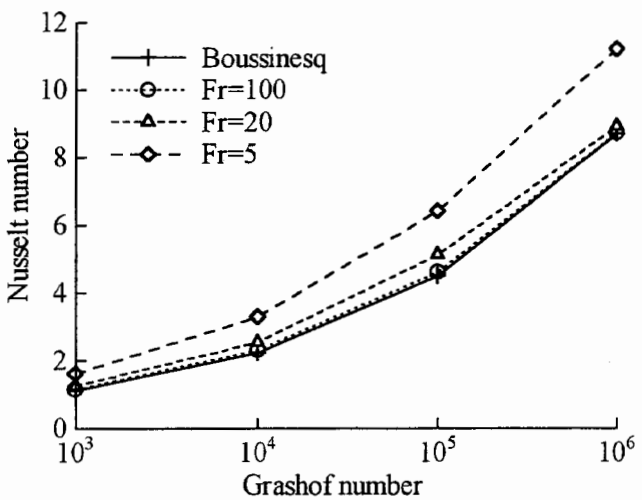

(a) Functions of *Gr* and *Fr*

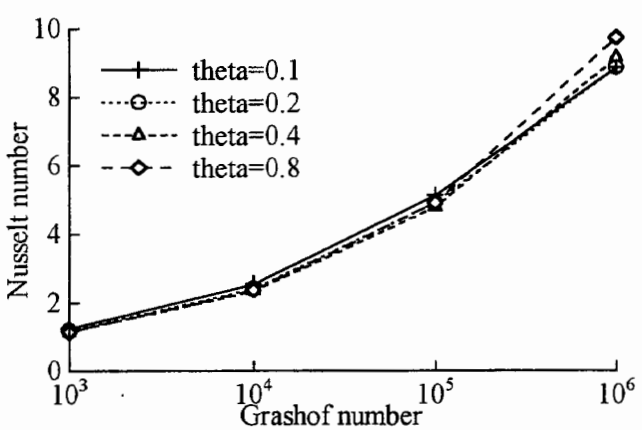

(b) Functions of *Gr* and θ

Figure 6.15. Heat conductivity characteristics.

6.5. Conclusions

The effects of viscosity, gravity, and temperature difference, on natural convection in a square cavity were investigated and the features were revealed in a systematic manner.

As the Grashof number increases, temperature boundary layers (TBLs) are formed on the walls. In the central region between the layers, the fluid is in a stratified state. The circulation has a single core for small *Gr*. As *Gr* increases the circulation becomes flattened and finally has two cores for large *Gr*. These secondary flows with closed streamlines are induced by locally inverted temperature distribution.

As the Froude number decreases (or the gravity increases) the gradient of temperature in TBL becomes steeper and the width of TBL becomes thinner due to compressibility. As *Fr* decreases the flow near the bottom prevails over the flow near the ceiling

As the temperature difference increases, circulation becomes stronger. At the same time, since the viscosity and heat conductivity are functions of temperature, the asymmetry of the flow becomes significant. For small *Gr*, horizontal asymmetry of the flow is significant. On the other hand, for large *Gr*, vertical asymmetry is significant.

It was confirmed that the flow of small θ and large *Fr* leads to the Boussinesq flow. The Boussinesq assumption is considered valid when $Fr \geqq 100$ and $\theta \leqq 0.1$.

The Nusselt number increases as *Gr* increases. The compressibility assists the increase of heat transfer. The Nusselt number is less sensitive to θ or it slightly decreases as θ increases, which is the opposite result to the simulation study by Leonardi et al.

References

[1] G. De Vahl Davis, "Natural Convection of Air in a Square Cavity: A Bench Mark Numerical Solution", Int. J. Num. Me. Fluids Vol.3: 249-264 (1983).

[2] Mallinson, G. D. and G. De Vahl Davis, "Three-dimensional Convection in a Box: A Numerical study", J. Fluid Mech. Vol.83, Part 1: 1-31(1977).

[3] Polezhaev, V. I., "Numerical Solution of the System of Two-Dimensional Unsteady Navier-Stokes Equations for a Compressible Gas in a Closed Region", Fluid Dynamics 2: 70-74 (1967).

[4] Leonardi, E. and Reizes, J. A., "Natural Convection in Compressible Fluids with Variable Properties", Num. Me. Thermal Problems: 297-306 (1979).

[5] Kawamura, H. and Hijikata, K., "Simulation of heat and flow", Maruzen, (1995) (in Japanese).

Acknowledgements

I wish to express my sincere gratitude to Professor Michihisa Tsutahara for his continuous guidance and encouragement for this study.

Minoru Watari
November 15, 2002